INFN/AExxx, LAL-xxx, SLAC-R-xxx

Super$B$ Detector Technical Design Report

Abstract

This report describes the technical design detector for Super$B$.

Contents

9 Electromagnetic Calorimeter

9.1 Overview

Calorimetry at Super$B$ is achieved with three major components: A CsI(Tl) "barrel" calorimeter covering the central region, a CsI(Tl)/LYSO(Ce) "forward" calorimeter covering the small angle region in the direction of the high energy beam, and a lead-scintillator "backward" calorimeter covering the small angle region in the direction of the low energy beam. Table 9.1 shows the solid angle coverage for each of the three parts of the Super$B$ EMC. The Super$B$ electromagnetic calorimeter (EMC) will play an essential role in the study of the flavor physics especially in the sector in which B meson decays involve neutral particles. The calorimeter provides energy and direction measurement of photons and electrons, reconstruction of neutral hadrons such as π^0's and discrimination between electrons and charged hadrons. Channels containing missing energy due to the presence of neutrinos will rely on information from the EMC to discriminate against backgrounds. The same criteria for good energy and position resolution apply for Super$B$ as for the *BABAR* calorimeter.

The Super$B$ EMC reuses the barrel part of the *BABAR* EMC detector consisting of 5760 CsI(Tl) crystals as shown in Fig. **??**. However the *BABAR* forward calorimeter will need to be partially replaced, due to the higher radiation and higher rates at SuperB compared with PEP-II. The innermost rings of the forward endcap will be replaced by new scintillating crystals designed to work well in this new environment.

After an intensive R&D program the baseline option for inner rings of the Super$B$ forward calorimeter is to use the faster and more radiation resistant LYSO crystals. As will be discussed below, this is the clear favorite in terms of performance and radiation hardness over the alternatives we have considered. The faster response time and shorter Molière radius serve together to address the higher event and background rates. LYSO is a fast scintillator largely used in medical applications with crystals of small size. The R&D is concentrated on the optimization of performance for large crystals (2cm x 2 cm x 20 cm) with good light yield uniformity and optimized Ce doping in order to have the best possible light output. Thanks to this effort, more than one producer is able to grow LYSO crystals of good quality that can be used in high energy physics applications. Table 9.2 shows the comparison between LYSO and other materials used in electromagnetic calorimeters. The largest disadvantage of LYSO is cost. The present design is a compromise. We have studied other lower cost alternatives as described below.

A lead-scintillator-sandwich backward endcap calorimeter improves the hermeticity of the detector. The main purpose of this component is to detect energy in the backward endcap region, as a veto of events with "extra" energy. This is particularly important for studying channels with neutrinos in the final state. Because of the fast time response, the backward EMC may also have a role in particle identification by providing time-of-flight for the relatively slow backward-going charged particles.

9.1.1 Background and radiation issues

One of the major concerns for the electromagnetic calorimeter is its capability to sustain the radiation dose, which is larger than in previous experiments due to the increased luminosity. The dominant contribution to radiation in Super$B$ is in fact expected to come from radiative Bhabha events that emit a large number of low energy photons at an extremely high rate.

Table 9.1: Solid angle coverage of the electromagnetic calorimeters. Values are obtained assuming the barrel calorimeter is in the same location with respect to the collision point as for *BABAR*. The CM numbers are for massless particles and nominal 4 on 7 GeV beam energies.

Calorimeter	$\cos\theta$ (lab)		$\cos\theta$ (CM)		Ω (CM)(%)
	minimum	maximum	minimum	maximum	
Backward	-0.974	-0.869	-0.985	-0.922	3.1
Barrel	-0.786	0.893	-0.870	0.824	84.7
Forward	0.896	0.965	0.829	0.941	5.6

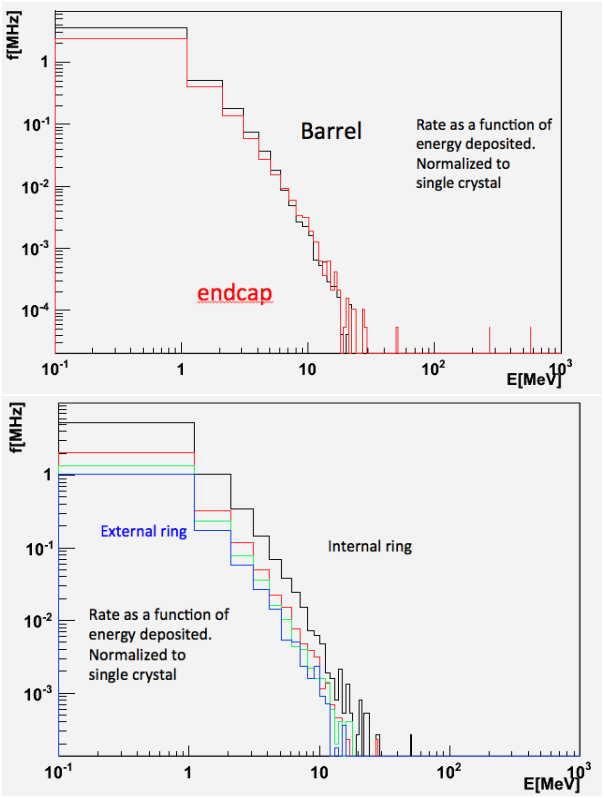

Figure 9.1: Machine Background rates per crystal as a function of deposited energy.

This photon rate can impact the performance of the detector because of two effects: the radiation can reduce the transmittance of the crystals and therefore alter as a function of time the calibration of the detector; the large number of photons can result in pile-up thus introducing a degradation in energy resolution.

To estimate the impact of these effects simulations have been set up as described in 9.1.2. The energy deposited by radiative Bhabha events in individual crystals is simulated at each beam crossing, i.e., every 2.1 ns. The resulting rates of energy deposit are shown in Fig. 9.1, both (left) averaging over the whole barrel and the whole FWD and (right) averaging over the rings of the FWD which have the same number of crystals per ring. The result shows that there is no significant difference in the irradiation between the barrel and the forward endcap. This can be understood because the dimension of the crystals is significantly different: due the different density and consequently Molière radius, the transverse dimensions of LYSO or BGO crystals are two times smaller than the CsI crystals (both doped and not) and the overall volume of a LYSO or BGO crystal is 6.7 times smaller (120cm^3 vs 800cm^3) than the CsI ones. Since the rates of signals from the machine background scales linearly with volume, the most forward crystals of the Barrel will suffer a background more than six times larger than the more central crystals of the FWD calorimeter, albeit contiguous.

On average therefore each crystal (both of Barrel or Endcap) will see 1MHz of photons between 1 and 5 MeV and 10 KHz of photons between 5-10 MeV. A plausible linear extrapolation in log-log scale would lead to 100Hz between 10-50 MeV and 1Hz between 50-100 MeV.

The ring-by-ring details are shown in Fig. 9.2, where the integrated rate of deposits larger than 5MeV are estimated as a function of an index,

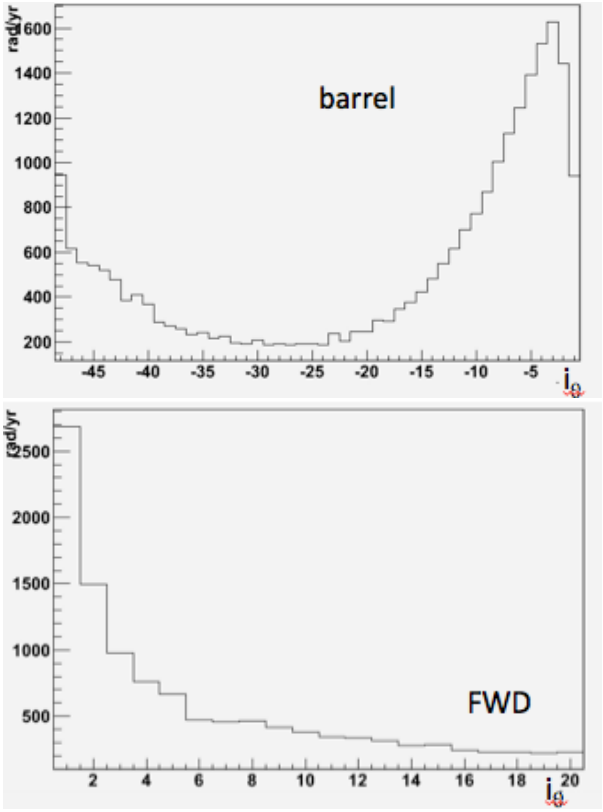

Figure 9.3: Integrated dose as a function of i_θ for the Barrel (Left) and FWD (Right) EMC.

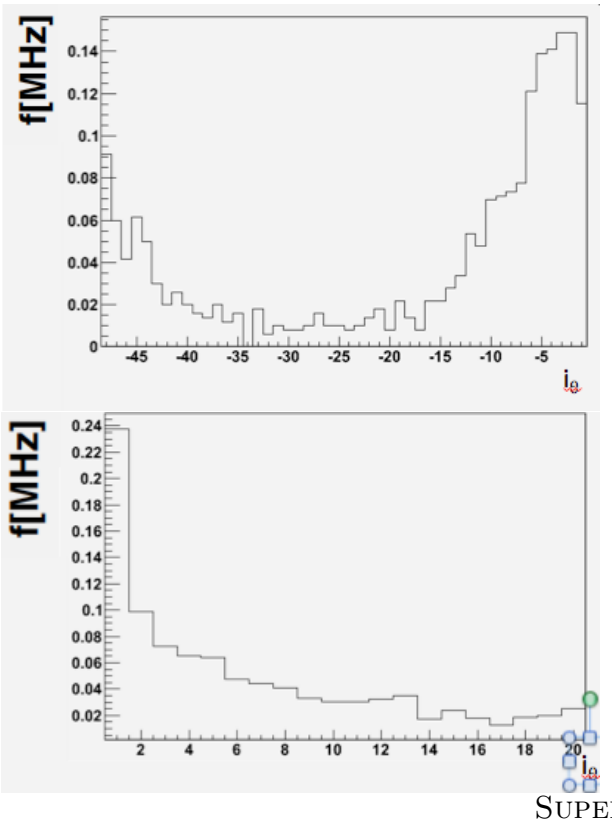

Figure 9.2: Integrated rates for $E > 5$MeV as a function of $i_\theta$for the Barrel (Left) and FWD (Right) EMC.

i_θ which is $i_\theta < -49$ for the backward calorimeter, $-49 =< i_\theta < 0$ for the barrel ($i_\theta = -1$ corresponding to the most forward ring), and $i_\theta > 0$ for the FWD EMC ($i_\theta = 1$ corresponding to the innermost ring) . It can be noted that the forward region of the barrel ($i_\theta > -10$) is more irradiated than the FWD calorimeter, a part from the innermost ring which is a factor two worse than any other ring.

From the radiation hardness point of view, the dose to which the crystals are sensitive is defined as the total energy deposited in a crystal divided by its mass. The dose expected per year (conventionally considered $10^7 s$ long) and per crystal is shown in Fig 9.3 separately for the Barrel and the FWD. Conservatively, assuming a maximum of 10 years of operations, crystals need to be radiation resistent up to at least 30krad. Also the impact on resolution of a $\sim$ 1rad/hour dose rate needs to be considered.

9.1.2 Simulation tools

9.1.2.1 Fastsim

A fast simulation (FastSim) tool based on the *BABAR* software framework has been developed to evaluate the detector performance, geometry optimization, and to study physics reach. The detector geometry is modeled by two-dimensional "shells" of basic topologies; cylinders, disks, cones, rectangles, etc. The event generators are identical to those in *BABAR*. Each particle is tracked in the detector volume; when it crosses a detector element, the interaction type and the energy loss are determined based on particle type, detector material and thickness. Secondary particles are created if necessary. Particle showers are represented by a quasi-particle instead of a (large) number of particles.

Charged track hits are fitted with a Kalman filter; EMC clusters are created based on the Moliere radius, interaction type (EM shower, hadron shower or minimum ionizing), detector segmentation, and parametrized shower shape. Geometry and model parameters can be easily set up and modified. The high level data structure of an event is the same as *BABAR*, including tracks, clusters, and particle identification objects, so one can directly apply available *BABAR* analysis tools.

Background cannot be simulated with FastSim because it is highly sensitive to the details of beam line and interaction region geometries, magnetic fields, beam trajectories, and so on. The secondary particles from beam and material interactions must be simulated precisely, which can only be done with a complete GEANT4 simulation. In order for the FastSim to include background effects, periodic "background frame" productions are carried out with GEANT4, including beam lines up to ±5 meters from the interaction point. For each bunch crossing, background particles that cross the boundary between the beam line elements and the detector volume are recorded and stored in a background frame file. In FastSim, for each signal event, background particles of a number of bunch crossings are read in from the background frame file and are appended to the list of signal particles, and then the FastSim proceeds as usual. The number of bunch crossings per signal event is determined by the crossing frequency and an overall sensitive time window. Each sub-detector has its own response timing structure to model the signal pulse.

9.1.2.2 FullSim

The calorimeter full simulation tool (FullSim) is based on GEANT4 and the Bruno tool (see Section **??**) which is used to simulate particle interactions and the energy deposits. The geometry description includes all of the Super*B* subdetectors and in the case of the Calorimeter it contains all the crystals and support structures. Bruno puts out information about the calorimeter is the deposited energy per crystal. Each single source of machine background is simulated separately for the whole SuperB detector and, if needed, they are combined in a second step of the analysis.

At the present stage of development the FullSim does not perform the digitization of signals and the reconstruction of clusters, which are instead obtained with a two step procedure through stand-alone programs. During the digitization stage, on top of the GEANT4 simulation, the electronic signal shape is generated for each crystal an with energy deposit; photostatistics, noise and time resolution effects are added using extrapolations from *BABAR*, or according to measurements when possible. For studying performance, signal particles events are overlapped with machine background events following the time structure of the bunch crossing rate in a time window centered on the signal particle arrival time; this allows the emulation of effects from the background including electronic signals pile-up. The different sources of background are mixed according to their probability and time behaviour.

Starting from the outcome of the digitization step a clustering is performed following the *BABAR* algorithm [1]; when the cluster energy is computed a random intercalibration error is applied at the 1% level (see for example [2]). To be accepted for clustering the signal peak from a crystal should be within a time window centered on the expected signal time.

9.2 Barrel Calorimeter

We propose to reuse the barrel portion of the *BABAR* EMC [2], retaining the fundamental mechanical structures and the 5760 CsI(Tl) crystals and associated pairs of photodiodes mounted on each crystal, along with some modifications required for optimal performance at Super*B*.

Below, we describe first the condition, as of the end of *BABAR* running, of the CsI(Tl) crystals which will be reused in the Super*B* detector. We then discuss the additional factors present at Super*B*, principally the high pile-up and back-

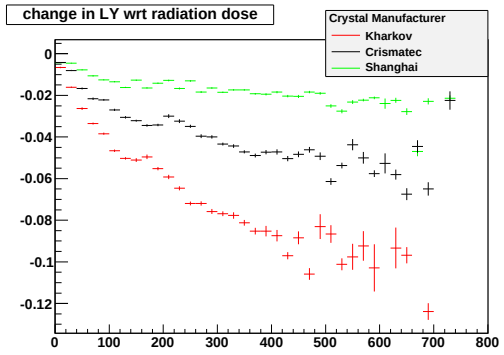

(a) Barrel backward

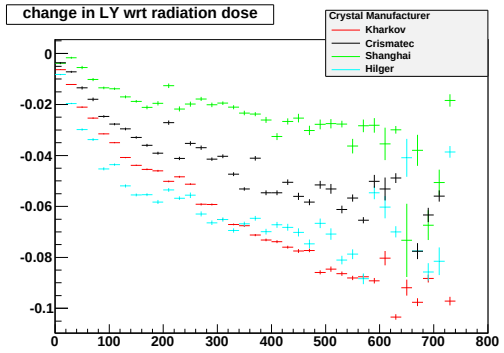

(b) Barrel forward

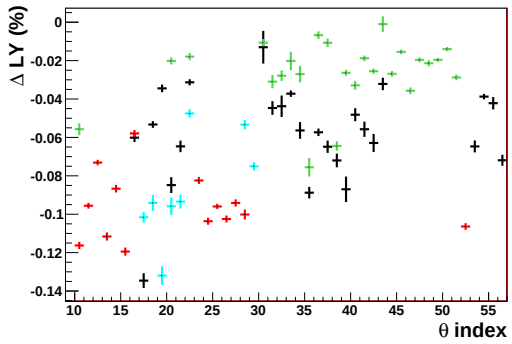

(c) Δ LY vs theta

Figure 9.4: Backward and forward barrel crystal light yield decreases versus absorbed radiation dose, with the different crystal providers indicated. The bottom plot shows the light yield decrease as a function of polar angle index for each manufacturer using the same color legend.

grounds environment, which must be addressed to optimize energy resolution. Next, we describe the mechanical design and calibration systems for the barrel, each of which will be minimally changed from their current configurations, as well as the detector readout. We then discuss the barrel's energy and position resolution, as well as the $\gamma\gamma$ mass resolution, and the effects on these due to long-term exposure to backgrounds at Babar. These trends are extrapolated to decreases in performance which might be expected over the lifetime of Super$B$.

We then describe the current barrel crystal photodiodes, which will not be replaced, and the changes proposed for the on-crystal preamplifier package and the front-end electronics. Lastly, we present the proposed plan for de-integration of the barrel EMC down to its component structures, the packaging and shipping of these, and their local storage and reintegration at a facility to be located at or near Tor Vergata.

9.2.1 Requirements Relevant to the SuperB Environment

9.2.1.1 Crystal Aging at BABAR

Over the span of *BABAR*'s running, the EMC barrel crystals have been damaged to a certain extent by high levels of radiation, which are monitored by 116 radFETs distributed throughout the subdetector. The most common form of damage [3] comes from the development of absorption bands which reduce an affected crystal's light yield. Although crystals in the EMC endcap experienced higher levels of radiation than those in the barrel, all EMC crystals from the furthest backward to those more forward integrated non-negligible doses. The resulting changes in crystal light yields were monitored and corrected for during *BABAR* operation using calibrations performed at either end of the dynamic range of the detector: a low-energy calibration using a 6.13 MeV radioactive photon source, which is discussed below in Sec. 9.2.2.3, and a high-energy calibration with Bhabha events.

The change in light yield for barrel crystals as a function of absorbed radiation dose, based on

the low-energy calibration data, is shown categorized by crystal manufacturer in Figure 9.4. Though care was initially taken to produce uniformity between crystals before they were integrated into the detector, there have been varying degrees of degradation in performance as time has progressed. Depending on the manufacturer, the total decrease in light yield can be up to $\sim 10\%$. Much of the decrease in light yield occurred during the initial years of *BABAR* running and, as the integrated dose increases, there is less light loss per unit dose received. However, as can be seen in Fig. 9.4, in the Super*B* environment, the eventual loss in light yield for the worst-performing barrel crystals, generally those provided by Kharkov and Hilger, may be substantial. The relative poor performance of the crystals provided by these manufacturers was known at the time of the barrel's construction and, to the extent possible, these manufacturers' crystals were placed as far backwards in polar angle as possible. as is shown in Fig. 9.4.

9.2.1.2 Backgrounds

In addition to crystal aging, background can degrade energy resolution due to electronic signal pile-up. The dominate source is expected to be photons and neutrons from radiative Bhabha events interacting with the detector material. This effect is negligible in *BABAR*. But in Super*B*, it could be substantial, especially in the low energy range.

The pile-up effect is a function of signal pulse shape. Since Super*B* is reusing *BABAR*'s barrel, the long decay time of CsI(Tl) crystal cannot be changed. Nonetheless, readout and electronics can be optimized to minimize the the impact of the pile-up effect. To ensure similar physics sensitivity as *BABAR*, the background pile-up should have a negligible effect in energy resolution of high energy photons (*how high?*) and contribute to no more than $x\%$ to energy resolution of photons at 100 MeV.

9.2.2 Description of BABAR Barrel Calorimeter

9.2.2.1 Mechanical design

The *BABAR* barrel EMC consists of a cylindrical shell with full azimuthal coverage, extending in polar angle from 26.8° to 141.8°. A longitudinal cross-section, including the forward endcap, is shown in Figure 9.5. The barrel EMC contains 5,760 crystals arranged in 48 separate azimuthal rings, with 120 identically dimensioned crystals in each ring. Each crystal has a tapered trapezoidal cross section, with length increasing from 29.6 cm furthest backward to 32.4 cm furthest forward in order to minimize the effects of shower leakage from increasingly higher energy particles. To minimize the probability of preshowers, the crystals are completely supported at the outer radius, with only a thin gas seal at the front. The amount of material in front of the crystal faces is $0.3 - 0.6X_0$.

Figure 9.6 is a schematic of a single crystal, showing the layered crystal wrappings, silicon photodiodes, diode carrier plate, preamplifier, and the aluminum housing enclosing the items at the crystal rear face.

The barrel crystals are inserted into modules that are supported individually from an external cylindrical support structure. At *BABAR*, the barrel support cylinder carries the load of the barrel modules plus the forward endcap to the magnet iron through four flexible supports, which decouple and dampen any acceleration induced by movements of the magnet iron during an earthquake.

The crystal modules are built from tapered, trapezoidal compartments made from carbon-fiber-epoxy composite (CFC) with 300 μm-thick walls. Each compartment loosely holds a single wrapped and instrumented crystal, assuring that the forces on the crystal surfaces never exceed its own weight. Each module is surrounded by an additional layer of 300 μm CFC to provide additional strength. The modules are bonded to an aluminum strong-back that is mounted on the external support structure. Figure 9.7 shows some details of a module and its mounting to the support cylinder. This scheme minimizes inter-crystal materials while exerting minimal force on the crystal surfaces, preventing geometric deformations and surface degradation that could compromise performance.

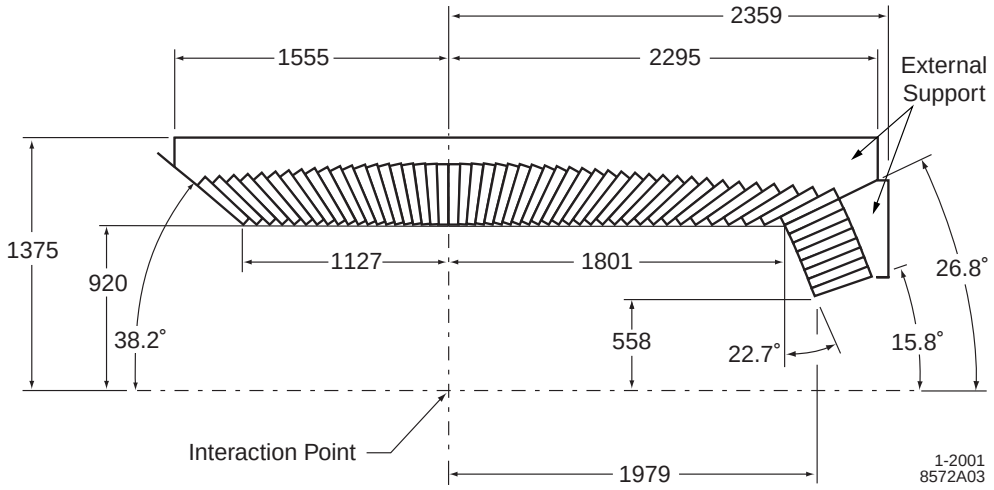

Figure 9.5: Longitudinal EMC cross-section (top half) showing the arrangement of the 48 barrel and 8 endcap crystal rings. The detector is axially symmetric around the z-axis. Dimensions are in mm.

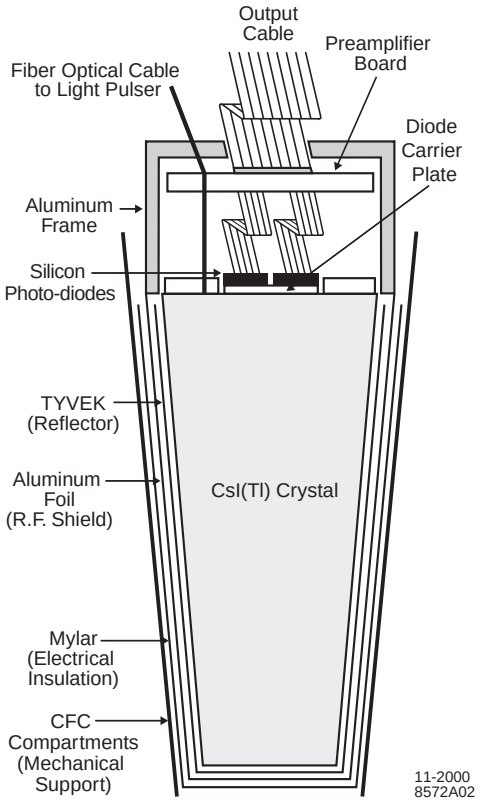

Figure 9.6: A schematic (not to scale) of a wrapped barrel crystal and the front-end readout package mounted on the rear face. Also indicated is the tapered, trapezoidal CFC compartment, which is open at the front.

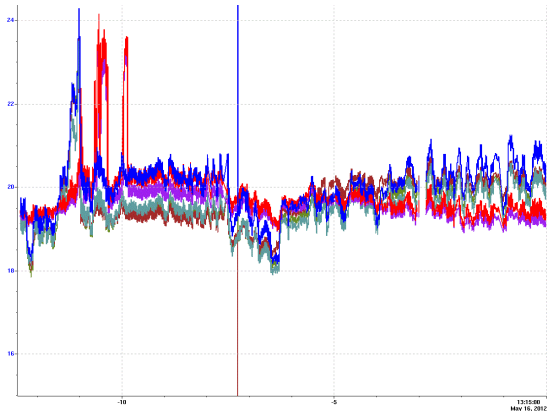

Figure 9.8: Barrel and endcap thermal history for one year. The four barrel quadrants are blue, brown, and dark and light green; the endcap halves are purple and red. The horizontal axis shows months prior to 16 May 2012. The vertical line extending the full range of the plot is an artifact due to a bad database record.

The barrel is divided into 280 separate modules, each holding 21 crystals (7×3 in $\theta \times \phi$), except for the furthest backward modules which are only 6×3. After insertion of the crystals, the aluminum readout frames, which also stiffen the module, are attached with thermally-conducting epoxy to each of the CFC compartments. The entire $\sim$ 100 kg module is then bolted and again thermally epoxied to an aluminum strong-back, which is shown in Figure 9.7. The strong-back contains alignment features as well as channels that couple to the cooling system. Each module is installed into the 2.5 cm-thick, 4 m-long aluminum support cylinder, and subsequently aligned. On each of the thick annular end-flanges, the support cylinder contains access ports for digitizing electronics crates with associated cooling channels, as well as mounting features and alignment dowels for the forward endcap. Figure 9.7 shows details of an electronics mini-crate situated within the support cylinder.

The primary heat sources internal to the calorimeter are the preamplifiers (2×50) mW/crystal and the digitizing electronics (3 kW per end-flange). In the barrel, the preamplifier heat is removed by conduction to the module strong backs which are directly cooled by Fluorinert (polychlorotrifluoroethylene). The digitizing electronics are housed in 80 mini-crates, each in contact with the end-flanges of the cylindrical support structure. These crates are indirectly cooled by chilled water pumped through channels milled into the end-flanges close to the inner and outer radii.

The entire barrel is surrounded by a double Faraday shield composed of two 1 mm-thick aluminum sheets so that the diodes and preamplifiers are further shielded from external noise. This cage also serves as the environmental barrier, allowing the slightly hygroscopic crystals to reside in a dry, temperature-controlled nitrogen atmosphere.

During *BABAR* data-taking, of particular concern is the stability of the photodiode leakage current, which rises exponentially with temperature, and crystal light yield, which is weakly temperature dependent. Currently, the most important issue is that the large number of diode-crystal epoxy joints experience as little stress as possible due to differential thermal expansion. Studies performed prior to the construction of the EMC showed that these joints should be safe when maintained at a temperature of (20 ± 5) C, and both the barrel and endcap are currently maintained in this state, with temperatures monitored in real-time and recorded in the conditions database. Fig. 9.8 shows the temperature history for one year for the four quadrants of the barrel and the two halves of the endcap.

9.2.2.2 Readout

Each CsI(Tl) barrel and endcap crystal is read out using $2 \times 1\,\mathrm{cm}^2$ silicon PIN diodes glued to a transparent 1.2 mm-thick polysterene substrate that, in turn, is glued to the center of the rear face of the crystal by an optical epoxy to maximize light transmission. The surrounding area of the crystal back face is covered by a plastic plate coated with white reflective paint, which has has two 3 mm-diameter penetrations for the fibers of the light pulser monitoring system.

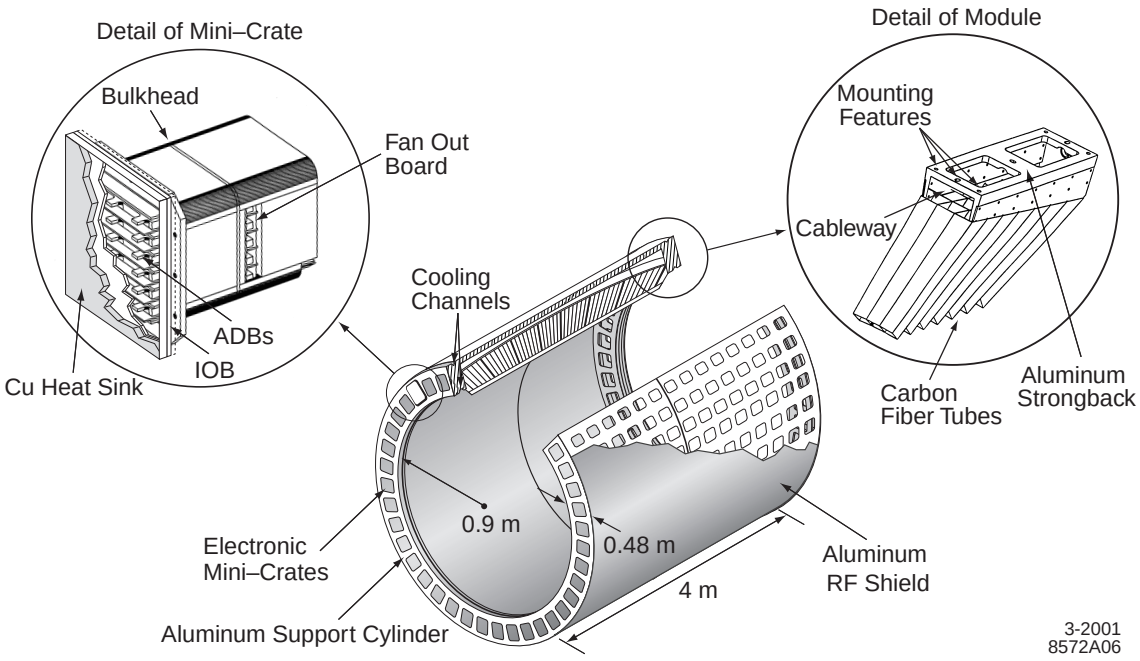

Figure 9.7: The EMC barrel support structure, with details on the modules and electronics crates (not to scale).

The signal from each of the diodes is transmitted to the preamplifier through a cable terminated in a connector that allows detachment of the preamplifier from the photodiodes. Each of the diodes is directly connected to a low-noise preamplifier, whose characteristics are discussed below in Sec. 9.2.4.2. The entire assembly at the crystal's rear facee is enclosed in an aluminum fixture as shown in Figure 9.6. This fixture is electrically coupled to the aluminum foil wrapped around the crystal and thermally coupled to the support frame in order to dissipate the heat load from the preamplifiers.

9.2.2.3 Low-energy Source Calibration

Calibration and monitoring during data-taking is important for achieving the best possible performance of the EMC. The low-energy calibration system devised for *BABAR* produces a 6.13 MeV photon line from a short-lived ^{16}O transition that can be activated as required. This system was successfully used for routine bi-weekly calibrations of the *BABAR* calorimeter, and is an ideal match to the Super$B$ requirements. We therefore propose to refurbish the *BABAR* system for use in Super$B$. The final *BABAR* calibration run was taken on 3 July 2008, and records of this run, as well as a few earlier ones, will be maintained for comparisons with the refurbished EMC.

In this system, fluorine, a component of Fluorinert^{TM} (polychlorotrifluoro-ethylene) coolant liquid, is activated with a neutron source to produce the ^{16}N isotope, which β-decays to an excited state of ^{16}O. This state in turn emits a 6.13 MeV photon as it cascades to its ground state. The source spectrum, as seen with a CsI(Tl) crystal with the PIN diode readout used in *BABAR*, is shown in Figure 9.9. There are three principal contributions to the overall peak, one at 6.13 MeV, another at 5.62 MeV, and the third at 5.11 MeV; the latter two representing e^+e^- annihilation photon escape peaks. Since all three peaks have well-defined energies, they simultaneously provide an absolute calibration, as well as a measure of the lin-

earity of the system at the low end of the energy scale.

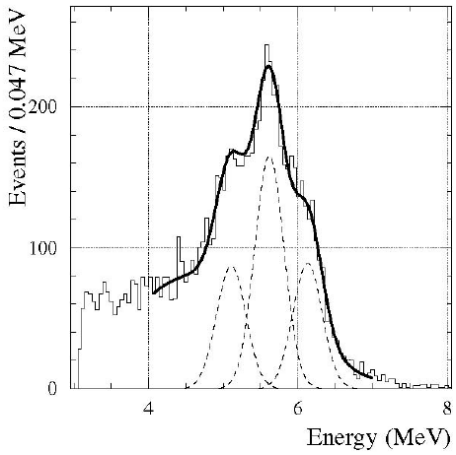

Figure 9.9: Energy spectrum in a single *BABAR* CsI(Tl) crystal irradiated with 6.13 MeV photons from an $^{16}O^*$ source, read out with a PIN diode. The solid curve is a fit to the spectrum, including Gaussian contributions at 6.13 MeV, 5.62 MeV, and 5.11 MeV, indicated by the dashed curves.

The fluorine activation is provided by a commercial deuterium-tritium (DT) generator, which produces 14.2 MeV neutrons by accelerating deuterons onto a tritium target, at typical rates of several times 10^8 neutrons/second. The DT generator is surrounded with a bath of fluorine-containing liquid, which is then circulated in a manifold to the barrel and endcap crystals. There are many suitable fluorine-containing liquids available; "Fluorinert FC77" [9], was used in *BABAR*. The half-life of the activated liquid is 7 s, hence residual radioactivity is not a substantial concern when the DT generator is not operating.

The Fluorinert is stored in a reservoir near the DT generator. When a calibration run is started, the generator and a circulating pump are turned on. Fluid is pumped from the reservoir through the DT bath to be activated, and then to the calorimeter. The system is closed, with fluid returning from the calorimeter to the reservoir. A schematic of the system is shown in Figure 9.10. In *BABAR*, the fluid is pumped at 3.5 l/s, producing a rate of approximately 40 Hz in each of 6500 crystals. This produces a calibration with a statistical uncertainty of 0.35% on peak positions in a single crystal in a 10-minute calibration run [8][10]. The crystals are approximately 12 m from the DT generator. Although Fluorinert FC-77 is no longer manufactured, an adequate supply is on-hand. Should it be necessary to substitute a commercially available coolant liquid (all of which have slightly reduced fractions of fluorine), the pumping rate would have to be adjusted accordingly.

In *BABAR*, the fluid transport manifold consisted of thin-wall (0.5 mm) aluminum tubing (3/8 inch diameter), flattened to meet space constraints. One millimeter of Al presents 1.2% of a radiation length. This material is placed in front of the *BABAR* crystals, as is an additional 2mm of Al in the structural support of the tube assemblies, which are deployed as a set of curved panels. This system can be reused for the barrel in Super$B$, or it could be rebuilt to better integrate into the barrel structure, reducing the amount of material and providing additional radial space.

The DT generator is a small accelerator; radiation safety protocols factor into the mechanical design of the system. For example, operation of the source will be done remotely, in a no-access condition. It will be shielded according to INFN radiation safety regulations. The shielding will be interlocked such that the DT generator cannot be operated if the shielding is not in place. The reservoir is capable of holding the entire volume of Fluorinert fluid. Operation of the system is anticipated to be approximately weekly. In the event of a fluid leak, the maximum exposure for the similar *BABAR* system is calculated to result in an integrated dose of less than 1 mrem. A detailed hazard analysis will be performed in collaboration with INFN radiation safety experts.

9.2.2.4 Light Pulser

The light response of the individual crystals during *BABAR* running was measured daily using a light-pulser system, which transmitted spec-

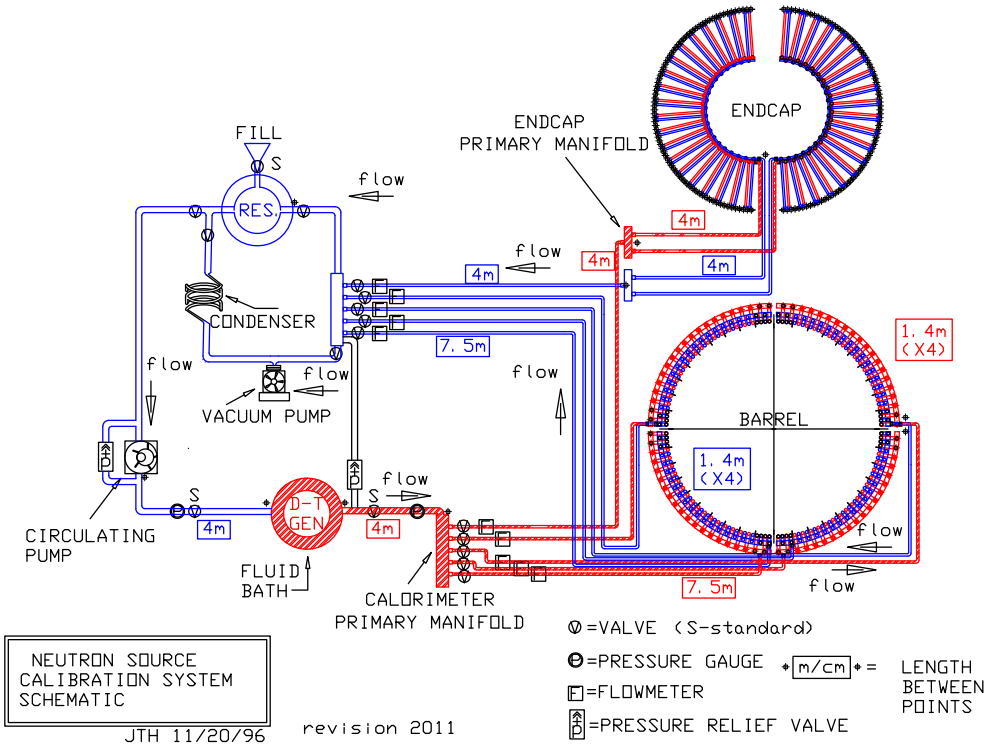

Figure 9.10: Schematic of the *BABAR* calibration system, which produces ^{19}F 6.13 MeV photons from an ^{16}O* source, as updated for Super*B*. The system is used for both the barrel and forward endcap calorimeters.

trally filtered light from a xenon flash lamp through optical fibers to the rear of each crystal, and we propose to refurbish the *BABAR* system for use in Super$B$. The light pulse is similar in spectrum, rise-time and shape to the scintillation light in the CsI(Tl) crystals. The pulses were varied in intensity by neutral-density filters, allowing a precise measurement of the linearity of light collection, conversion to charge, amplification, and digitization. The intensity was monitored pulse-to-pulse by comparison to a reference system with two radioactive sources, ^{241}Am and ^{148}Gd. Each of these was attached to a small CsI(Tl) crystal read out by both a photodiode and a photomultiplier tube, and were stable to 0.15% over a period of one week.

9.2.3 Performance of BABAR barrel

9.2.3.1 Energy and position resolution

The energy resolution of a homogeneous crystal calorimeter is generally given empirically as two terms summed in quadrature:

$$\frac{\sigma_E}{E} = \frac{a}{\sqrt[4]{E(GeV)}} \oplus b, \qquad (9.1)$$

where E and σ_E refer to the energy of a photon and its RMS error in GeV. The energy-dependent term, a, arises from fluctuations in photon statistics, electronics noise, and beam background generated noise. The constant term, b, arises from non-uniformity in light collection, leakage, and absorption in the material between and in front of the crystals, as well as uncertainties in the calibration. The angular resolution is primarily determined by the crystals' transverse dimension. Figure 9.11 shows the energy and angular resolution of the *BABAR* calorimeter derived from various data control samples, as indicated in the plot legends, and from which are derived the fundamental EMC performance characteristics:

$$\frac{\sigma_E}{E} = \frac{(2.30 \pm 0.03 \pm 0.3)\%}{(E(\mathrm{GeV}))^{0.25}} \oplus (1.35 \pm 0.08 \pm 0.2)\% \qquad (9.2)$$

$$\sigma_\theta = \sigma_\phi = \frac{(4.16 \pm 0.04)\mathrm{mrad}}{\sqrt{E(\mathrm{GeV})}} \oplus (0.0 \pm 0.0)\mathrm{mrad} \qquad (9.3)$$

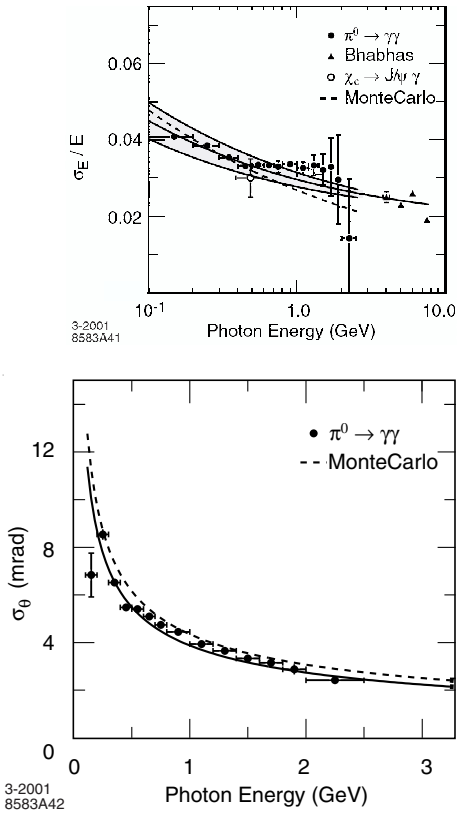

Figure 9.11: Photon energy (top) and angular (bottom) *BABAR* EMC resolutions.

Figure 9.12 shows similar plots from the December 2011 Super$B$ Fastsim using single photon MC at several energies. *[COMPARE-AND-CONTRAST BETWEEN BABAR DATA AND SUPERB MC.]*

9.2.3.2 Gamma-gamma mass resolution

Figure 9.13 shows a two-photon invariant mass distribution in the π^0 and η mass ranges for selected *BABAR* data multi-hadron events from 2001. Photons are required to have $E_\gamma > 30\,\mathrm{MeV}$, with π^0 candidate energy $E_{\pi^0} > 300\,\mathrm{MeV}$ and η candidate energy $E_\eta > 1\,\mathrm{GeV}$. The reconstructed π^0 mass is found to be $134.9\,\mathrm{MeV}/c^2$, with a width of $6.5\,\mathrm{MeV}/c^2$; the fitted η mass is $547\,\mathrm{MeV}/c^2$, with a width of $15.5\,\mathrm{MeV}/c^2$. These can be compared to a two-photon invariant mass distribution from the June 2012 Fastsim MC production *ADD FIGURE.*

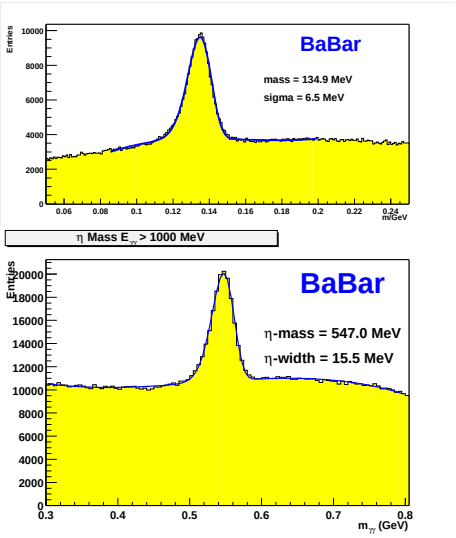

Figure 9.13: Two-photon invariant mass distribution in π^0 (top) and η (bottom) mass ranges.

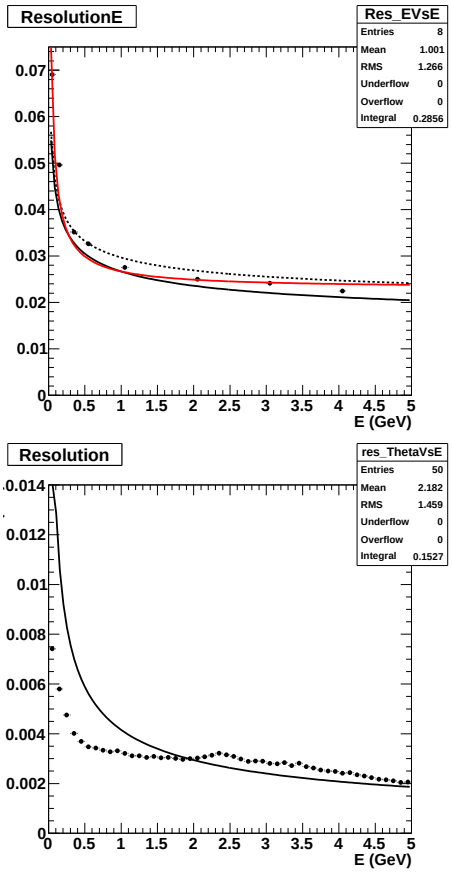

Figure 9.12: Fastsim single photon energy (top) and angular (bottom) resolution.

9.2.3.3 Radiation Damage Effects on Resolution

Beam generated backgrounds are the major cause of reduction in the light yield of the crystals over time. In order to monitor this source of background, 116 Rad FETs are placed in front of the calorimeter barrel and endcap crystals. These RadFETs are real-time integrating dosimeters based on solid-state MOS technology and are integrated into the EPICS monitoring system. As can be seen in Fig 9.14, the integrated dose is largest in the endcap, which is closer the the beam line as well as more forward in polar angle making it more susceptible to beam generated background photons from small angle radiative Bhabha events in which an $e^{\pm}$ strikes a machine element.

Radiation damage impacts CsI(Tl) through the creation of color centers in the crystals, inducing absorption, and resulting in a degradation of response uniformity and light yield. The nominal dose budget for the *BABAR* CsI(Tl) calorimeter is 10 krad over the lifetime of the detector. Pure CsI and L(Y)SO are considerably more radiation hard (see Table **??**). The dominant contribution to the dose arises from luminosity and single-beam background sources, and hence is due to MeV-level photons and (presumably) neutrons; the integrated dose scales approximately linearly with integrated luminosity.

The measured reduction of light yield due to radiation damage is shown as a function of integrated luminosity in Fig. 9.14. To date, a total dose of about 1.2krad has been received in the most heavily irradiated regions, resulting in a loss of about $\sim 15\%$ of the total light yield, but with no measurable impact on physics performance. It is notable that most of the observed light loss occurred relatively early in *BABAR* running, although radiation dose has been accumulating relatively steadily, and that crystals from different manufacturers have responded somewhat differently to irradiation. It is anticipated that the CsI(Tl) barrel will have accumulated approximately 1.5 krad in the most irradiated regions by the end of nominal *BABAR* running in 2008.

In order for the barrel calorimeter to function in the Super$B$ environment, beam background rates must be maintained at a level of approximately 1 MeV/μs or less per CsI(Tl) crystal. If this condition is achieved, then radiation dose rates are anticipated to be roughly comparable to current *BABAR* levels. A dose budget of well under 1 krad/year is expected to be achievable. At this a level, the CsI(Tl) barrel would survive for the duration of Super$B$ operations. This assumption will, however, need to be verified by detailed simulation.

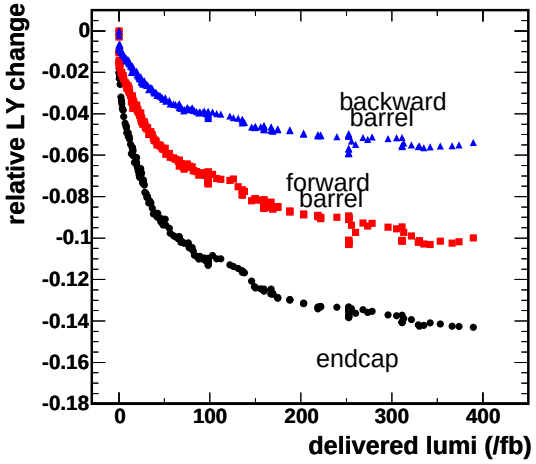

Figure 9.14: The light yield loss in the *BABAR* CsI(Tl) crystals due to radiation damage as a function of luminosity. The total dose received after 300 fb^{-1} is 1.2k rad in the endcap and 750 rad in the barrel.

9.2.3.4 Expected Changes in Performance at SuperB

The CsI(Tl) crystals used in the barrel calorimeters of both *BABAR* and Belle are the most expensive elements of the two detectors. Based on the performance that has been achieved, and the radiation damage that has been observed so far, both collaborations have concluded that the reuse of the barrel crystals is possible at a Super B Factory.

The baseline assumption is that the geometry of the crystals is unchanged from that of the current *BABAR* detector. The one change that should be made is to move the position of the interaction point from -5 cm to $+5$ cm relative to the position of the crystal gap normal to the beam axis. This adjustment retains the current non-pointing geometry, but moves the barrel to a slightly more symmetric position, in view of the reduced energy asymmetry. The effect of the change in boost from $\gamma\beta = 0.56$ to 0.28 and the shift of the IP is to increase the angular coverage of the barrel from 79.5% ($\cos\theta = -0.931$ to $+0.661$) to 84.1% ($\cos\theta = -0.883$ to $+0.798$).

If the crystal geometry is unchanged, it is in principle possible to transport the entire barrel calorimeter as one cylinder. However, the barrel was not designed for long-haul moves, and entertaining this option requires a substantial engineering evaluation. Alternatively it could be disassembled into its 280 individual modules, which would be transported separately and reassembled on arrival. This option carries lower risk and is the baseline, unless further study demonstrates that the barrel can be moved as a unit. The costs of these alternatives are discussed in the chapter on the reuse of existing *BABAR* detector elements.

A possible change to improve the coverage in the backward region would be to add one or two additional rings of crystals to the last module ring in θ, which currently only contains 6 rings of crystals. However, this would lead to major changes in the mechanical support structure and a redesign of the electronics readout, so it will not be undertaken unless there is a significant gain from the extra ring(s). Changes to the rear section of the barrel also interact strongly with the possible addition of a backward endcap calorimeter (Sec. 9.4).

9.2.4 Electronics changes

The EMC barrel reuses the original 5760 crystals from *BABAR*. The crystals are coupled to two PIN (Hamamatsu S2744-08) diodes glued to the large area of the crystal face. The possibility to change these photo-detectors with new devices was investigated, but the strong mechanical constraints and the impossibility to unglue the PIN photodiodes without the risk of damage, obliged us to maintain the original photodetectors. Each PIN diode in *BABAR* is read with a separate electronic chain composed of a charge sensitive preamplifier and a CR-RC-RC shaper, with 800 ns -250 ns -250 ns shaping time. The output of each channel is amplified in two chains respectively with a gain of 1 and 32.

9.2.4.1 Rationale for changes

In the Super$B$ configuration we want to substitute all the Front End Boards of the Barrel Calorimeter. The new Front End Boards use off-the-shelf components in order to have a shorter integration time of the order of less than one microsecond. Mechanical constraints require the same form factor of the original *BABAR* Front End Board. The necessity to reduce the integration time comes from a more intense background radiation in the Super$B$ environment. A shorter integration time uses less photons from the crystals but also avoids photons coming from off time events generated from background. To use a shorter integration time we must also reduce the shaping time from the order of one microsecond to few hundreds of nanoseconds. Tests and simulations have been performed to understand better how to change the integration and shaping time. The need to have a good time signal to use in the EMC trigger focused the design of the charge preamplifier to a transimpedence amplifier with a low feedback capacitance The choice to use a lower integration and shaping time decreases the background noise due to the background radiation but decreases also the number of photons collected from the scintillator, with a worse resolution due to less signal. Moreover a shorter shaping time increase the noise due to a larger bandwidth of the shaper.

The design of the preamplifier requires special care to obtain a lower noise from the beginning by choosing low noise components. We expect also an increase of the power consumption of the new Front End Boards due to the use of

larger bandwidth operational amplifiers and of off-the-shelf components.

9.2.4.2 Electronics design

The readout of each PIN diode is done using two separate channels. This choice is motivated from the necessity to have high redundancy and minimize the possibility to have dead channels in case of a PIN diode break. In order to minimize the noise of the Front End Boards we provide two outputs for each channel, one for the low energy range and the other for the high energy range, with a gain of 1 and 32 as in *BABAR*. The idea to use only one gain in the Front-End was dropped because using shorter integration times give smaller signals than *BABAR*. Consequently we have to improve signal to noise from the beginning, avoiding passing low level signals in long cables. The four signals for each crystal (two channels with two different gains) are combined in the digitizer board; normally the mean signal from two PIN diodes is chosen but in case of breakage of one PIN diode only one signal can be chosen. A dedicated circuit chooses the signal range to use for the digitalization. The digitalization is done using a 12 bit ADC, with a shaping time of 500 ns, a sampling rate of 7.43 MHz (RF/8) plus a range bit. If full granularity data were pushed synchronously to the trigger, about 520 optical links would be necessary. The number of synchronous trigger links can be drastically reduced by performing sums of 4 3 cells on the detector side, so that 6 such energy sums could be continuously transmitted through a single optical serial link. This permits a reduction in the number of trigger links so as to match the topology of the calorimeter electronics boxes, which are split into 40 sectors on both sides of the detector. Therefore, the total number of links would be 80 both for the trigger and the data readout toward the ROMs, including a substantial safety margin ($>$ 1:5).

9.2.5 SLAC De-installation, Transport and Local Storage

9.2.6 Electronics refurbishment

The guiding criterion in the upgrade of the Barrel electronics is to maintain the same hierarchy in the components as in *BABAR*, by using the same mechanical form factor for each board to fit the new system in the old mechanics.

The front end preamplifiers are located on the top of the crystals inside brass cages. The design of the cages is strictly connected to the crystal photodiodes assembly which is very difficult to unglue and disassemble. The brass cages are robust and can be dismounted and reused without the risk of damage.

With the intent to reuse this brass cage we choose the preamplifier form factor to fit inside using also the same form factor connector and cable.

The Barrel electronics in *BABAR* was housed inside 48 small custom-built crates (minicrates) located on the top of the 24 Barrel's for each side. Each minicrate contains a backplane that divides the connection board from the digitizer boards and an optical board on top.

We plan to use the mechanical structure of the minicrates maintaining the same form factors of the four boards (connection boards, backplane, digitizer board, and optical transmission board).

9.2.7 Re-installation at Tor Vergata

9.3 Forward Calorimeter

The Forward Calorimeter is designed to extend the coverage of the electromagnetic calorimeter to low angles, as detailed in Tab. 9.1. To be effective its performance needs therefore to be comparable with the Barrel Calorimeter. Thus, the design considers a calorimeter made of crystals and read-out by compact photodetectors capable of operating in magnetic field.

Taking as benchmark the *BABAR* detector, the relative energy resolution should be at most 4.3% at 100 MeV and 2.7% at 1 GeV. Also, in order to assure appropriate resolution on the π^0 invariant mass and to allow the $\pi^0 \to \gamma\gamma$ reconstruction up to sufficiently high energies, a segmentation at least comparable with the *BABAR* one is needed. Since the transverse crystal size

is dictated by the Molière radius of the material, only crystals with a Molière radius at most as large as the CsI(Tl) can be considered. Finally hermeticity is also important, so the requirement on mechanics is that the fraction of particles originating from the interaction point passing through the cracks between the crystals be minimal, comparable with the barrel.

As already described for the Barrel Calorimeter, the most stringent constraints come from the presence of large background due to the extremely high luminosity. As shown in Fig. 9.3, the expected dose integrated in a year ranges from $\sim$ 200 rad for the outermost rings to $\sim$ 2500 rad for the innermost ones. Consequently, the dose rate the crystals need to tolerate ranges from $\sim$ 0.1 rad/s to $\sim$ 1.0 rad/s, respectively.

As described in Sec. 9.1.1, the large rate of low energy photons can create radiation damage on the crystal themselves, thus reducing the light yield, and induce a degradation of the energy resolution due to pile-up. Therefore the chosen crystal must show a stable light yield under the expected radiation and the signal shape produced by the readout must be compatible with the expected rates.

We have investigated several combinations of crystals and electronics, as described below. The best option for performance is to use crystals made of LYSO, with readout by Avalance Photo-Diodes (APD). This configuration has been studied in detail. However, budget restrictions force us to adopt as baseline a "hybrid" scheme, making use of LYSO at the smallest radii while keeping the BaBar crystals, made of $CsI(Tl)$, in the outermost endcap layers. This permits a significant reduction in cost, while obtaining the benefits of LYSO where it is needed most, where the rate and radiation issues are most severe. As part of this cost compromise, the structural support of the *BABAR* endcap is reused instead of adopting a lower mass solution.

9.3.1 LYSO Crystals

In the last two decades, cerium doped lutetium oxyorthosilicate (Lu_2SiO_5 or LSO) [4] and cerium doped lutetium yttrium oxyorthosilicate ($Lu_{2(1-x)}Y_{2x}SiO_5$ or LYSO) [5] have been developed for the medical industry with mass production capabilities established. This section addresses the crystal properties, specifications, production and testing.

9.3.1.1 Introduction

Table 9.2 [6] lists basic properties of heavy crystals: NaI(Tl), CsI(Tl), pure CsI, bismuth gemanade ($Bi_4Ge_3O_{12}$ or BGO), lead tungstate ($PbWO_4$ or PWO) and LSO/LYSO. All have either been used in, or are actively being pursued for, high energy and nuclear physics experiments, which are also listed in the table. The experiment names in bold refer to future crystal calorimeters. NaI(Tl), CsI(Tl), BGO, LSO and LYSO crystals are also widely used in the medical industry. Mass production capabilities exist for all these crystals.

Because of their high stopping power, high light yield, fast decay time, small temperature coefficient and excellent radiation hardness, LSO and LYSO crystals have attracted a broad interest in the high energy physics (HEP) community [7, 8, 9, 10], and are chosen for the baseline material for the SuperB forward calorimeter. LSO and LYSO crystals from the following vendors have been tested during the R&D phase of the project: CTI Molecular Imaging (CTI), Crystal Photonics, Inc. (CPI), Saint-Gobain (SG), Sichuan Institute of Piezoelectric and Acousto-optic Technology (SIPAT) and Shanghai Institute of Ceramics (SIC).

9.3.1.2 Optical and Scintillation Properties

Transmittance and Emission

LYSO crystals of 20 cm (18 X_0) length are routinely produced in industry with good transmittance spectra. The left plot of Figure 9.15 shows the longitudinal (green) and transverse (red) transmittance spectra measured for a rectangular LYSO sample with a dimension of 2.5 $\times$ 2.5 $\times$ 20 cm (18 X_0). Significant red shift is observed in the absorption edge of the longitudinal transmittance as compared to the transverse transmittance, caused by internal absorption. The black line at the top is a fit to the theoret-

Table 9.2: Properties of Heavy Crystal with Mass Production Capability

Crystal	NaI(Tl)	CsI(Tl)	CsI	BGO	$PbWO_4$	LSO/LYSO(Ce)
Density (g/cm^3)	3.67	4.51	4.51	7.13	8.3	7.40
Melting Point (°CC)	651	621	621	1050	1123	2050
Radiation Length (cm)	2.59	1.86	1.86	1.12	0.89	1.14
Molière Radius (cm)	4.13	3.57	3.57	2.23	2.00	2.07
Interaction Length (cm)	42.9	39.3	39.3	22.7	20.7	20.9
Refractive Index[a]	1.85	1.79	1.95	2.15	2.20	1.82
Hygroscopicity	Yes	Slight	Slight	No	No	No
Luminescence[b] (nm)	410	560	420	480	425	420
(at Peak)			310		420	
Decay Time[b] (ns)	245	1220	30	300	30	40
			6		10	
Light Yield[b,c]	100	165	3.6	21	0.30	85
			1.1		0.077	
d(LY)/dT[b,d] (%/°CC)	-0.2	0.4	-1.4	-0.9	-2.5	-0.2
Experiment	Crystal Ball	CLEO *BaBar* BELLE BES III	kTeV	L3 BELLE	CMS ALICE PrimEx **Panda**	**Mu2e SuperB HL-LHC?**

a At the wavelength of the emission maximum.
b Top line: slow component, bottom line: fast component.
c Relative light yield of samples of 1.5 X_0 and with the PMT quantum efficiency taken out.
d At room temperature.

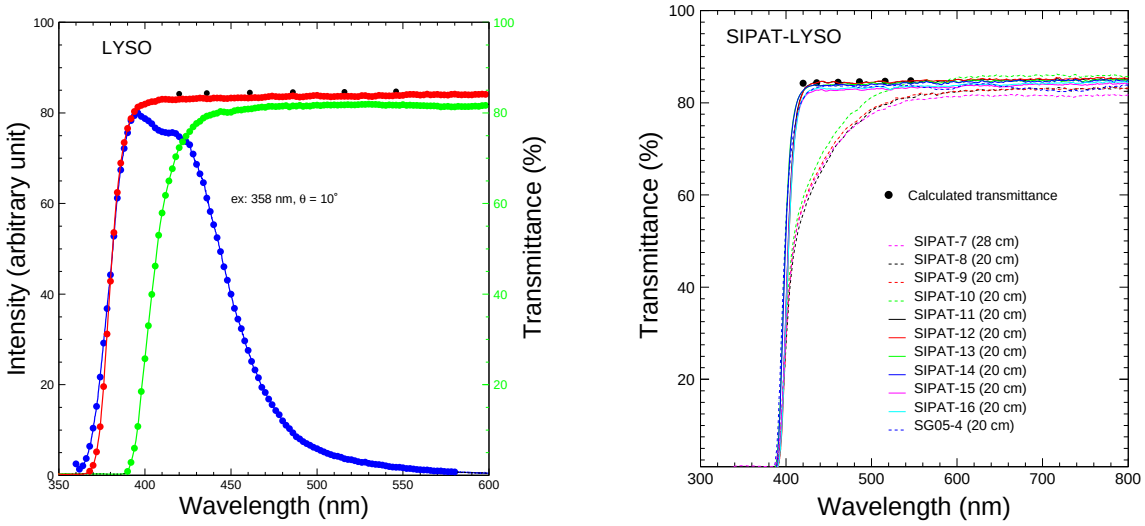

Figure 9.15: Left: The longitudinal (green) and transverse (red) transmittance spectra and the photo-luminescence (blue) spectrum are shown as a function of wavelength for a rectangular LYSO sample with a dimension of 2.5 × 2.5 × 20 cm. Right: Longitudinal transmittance spectra are shown as a function of wavelength for eleven LYSO crystals: ten from SIPAT and one from Saint-Gobain. All except SIPAT-7 are 20 cm long.

ical limit of transmittance calculated by using the refractive index assuming multiple bounces between two end surfaces and no internal absorption [11]. It overlaps with the transverse transmittance spectrum at wavelengths longer than 420 nm, indicating excellent optical quality of the crystal. Also shown in this plot is the photo-luminescence spectrum (blue) [12]. The fact that a part of the emission spectrum is at the wavelengths shorter than the absorption edge indicates that this part of the scintillation light is absorbed internally in the crystal bulk, usually referred to as self-absorption effect. There is no such self-absorption effect in other scintillation crystals commonly used for HEP calorimeters, such as BGO, CsI(Tl) and PWO [6]. While this self-absorption has little consequence to 6 mm long pixels used in medical instruments, it affects light response uniformity for 20 cm long crystals used in the SuperB calorimeter. This effect will be discussed in section 9.3.1.2.

During the R&D phase for crystal development poor longitudinal transmittance was observed in some samples [13]. The right plot of Figure 9.15 shows that four samples (SIPAT-7 to SIPAT-10) have poor longitudinal transmittance between 380 nm and 500 nm, showing an absorption band. Further investigation shows that this absorption band is located at the seed end and is caused by point defects [12], associated with a bad seed used in their growth. With rigorous quality control, LYSO crystals grown later at SIPAT (SIPAT-11 to SIPAT-16) show no absorption band at the seed end, as shown in the right plot of Figure 9.15. An increase of light output of about 30% was found after this problem was resolved. It thus is important to include in crystal specifications a requirement on the crystal's longitudinal transmittance.

The left plot of Figure 9.16 shows typical quantum efficiencies of a PMT with multi-alkali cathode (Photonis XP2254b) and an APD (Hamamatsu S8664) [14]. Also shown in the figure are the photo luminescence spectra of LSO/LYSO, BGO and CsI(Tl) crystals, where the area under the luminescence spectra is roughly proportional to the corresponding absolute light output. Table 9.3 summarizes the numerical values of the photo luminescence weighted average quantum efficiencies for vari-

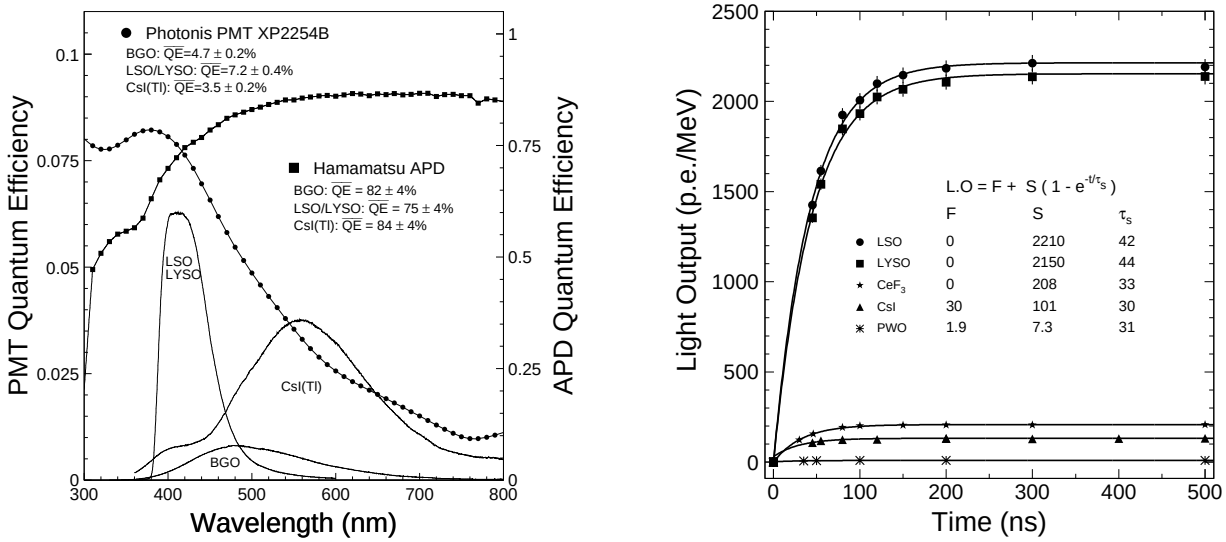

Figure 9.16: Left: The quantum efficiencies of a Hamamatsu R2059 PMT (solid dots) and a Hamamatsu S8664 APD (solid squares)are shown as a function of wavelength together with photo-luminescence spectra of the LSO/LYSO, BGO and CsI(Tl) samples, where the area under the luminescence spectra is roughly propotional to the corresponding absolute light output. Right: Light output measured by using a Photonis XP2254 PMT is shown as a function of integration time for six crystal scintillators.

ous readout devices. These numbers can be used to convert the measured photo-electron numbers to the absolute light output in photon numbers.

A significant red component was observed in the γ-ray induced luminescence spectra in the CTI LSO samples, but not in the LYSO samples from other growers [12]. This red component disappeared after a γ-ray irradiation with an accumulated dose of 5×10^3 rad. This is the only significant difference observed between the large size LSO and LYSO samples [12], indicating that LYSO is a preferred choice.

Decay time and Light Output

The right plot of Figures 9.16 shows light output in unit of photo-electron/MeV, measured using a Photonis XP2254 PMT as a function of integration time, for six crystal scintillators [6]. The light output can be fit to the following function to determine the fast and slow components and the decay kinetics:

$$LO(t) = F + S(1 - e^{-t/\tau_s}), \qquad (9.4)$$

where F is the fast component of the scintillation light with a decay time of less than 10 ns, and S represents the slow component with a decay time of τ_s longer than 10 ns. The decay time of both LSO and LYSO crystals is about 40 ns.

As shown in Table 9.2 LSO and LYSO crystals have high light output, about 85% and 50% of NaI(Tl) and CsI(Tl) respectively, and about 18, 4, and more than 200 times of pure CsI, BGO, and PWO, respectively. Figure 9.17 shows 0.511 γ-ray pulse height spectra measured by a Hamamatsu R1306 PMT (left) and two Hamamatsu S8664-55 APDs (right) for four LSO and LYSO samples of $2.5 \times 2.5 \times 20$ cm^3 from CTI, CPI, SG, and SIPAT. The equivalent noise energy for the APD readout is less than 40 keV [14]. Poor energy resolution was found in the CPI LYSO sample, but not other samples. According to the grower this was caused by intrinsic non-uniformity, which may be improved by appropriate thermal annealing. It thus is important to include in crystal specifications a requirement on the crystal's energy resolution.

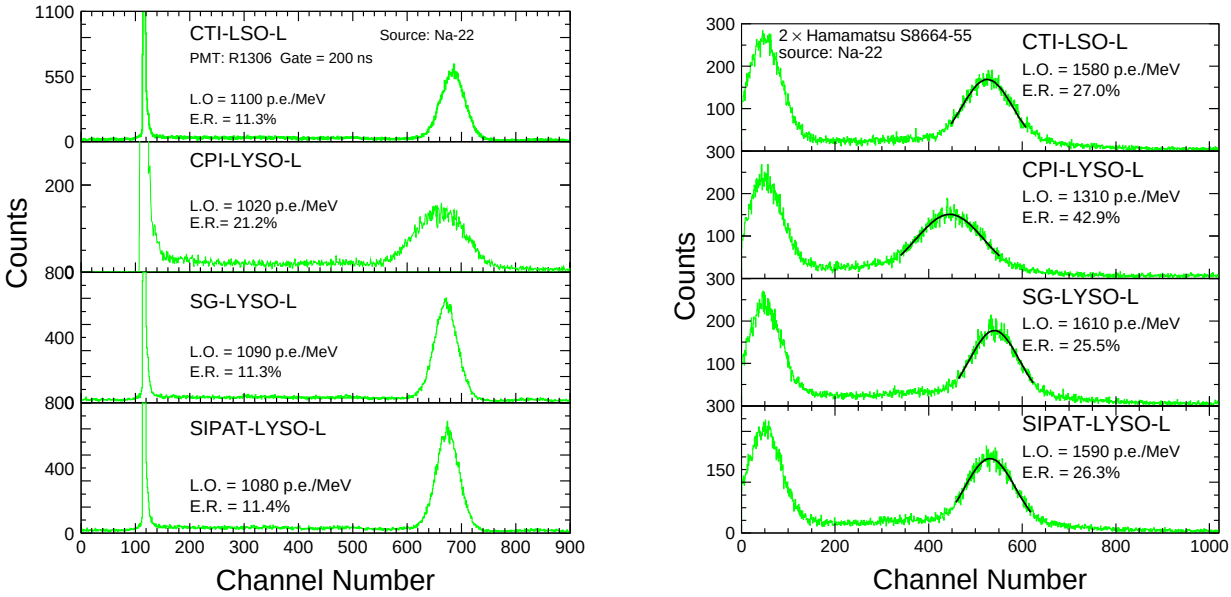

Figure 9.17: 0.511 MeV γ-ray spectra from a ^{22}Na source, measured by a Hamamatsu R1306 PMT (Left) and two Hamamatsu S8664-55 APDs (Right), with a coincidence trigger for four long LSO and LYSO samples of $2.5 \times 2.5 \times 20$ cm^3.

Because of their fast decay time and high light output, LSO and LYSO crystals have also been used in time of flight (TOF) measurements for medical applications, such as TOF PET(positron emission tomography). Better than 500 ps FWHM was achieved for the time difference between two photons. In HEP experiments a rms time resolution of better than 150 ps may be achieved for TOF measurements for single particles. Since the intrinsic rise time of scintillation light is about 30 ps for LSO and LYSO crystals [17], the measured time resolution for LSO and LYSO is affected mainly by the response speed of the readout device and the choice of time pick-off [16]. Doping calcium in LSO and LYSO is reported to reduce the decay time to about 20 ns [18], which would help to improve the time resolution.

Light Collection and Response Uniformity

It is well known that adequate light response uniformity along the crystal length is key for maintaining the precision offered by a total absorption crystal calorimeter at high energies [19]. The light response uniformity of a long crystal as shown in Figure 9.18 (Left) is parameterized as a linear function

$$\frac{LY}{LY_{\rm mid}} = 1 + \delta(x/x_{\rm mid} - 1), \qquad (9.5)$$

where ($LY_{\rm mid}$) represents the light output measured at the middle point of the crystal, δ represents the deviation from the flat response and x is the distance from the photo-detector. To achieve good energy resolution, the corresponding $|\delta|$ value for SuperB LYSO crystals of 18 X_0 length must be kept to less than 3% [20].

Effective light collection requires good light reflection. The glass fiber based supporting structure designed for the superB forward calorimeter is coated with a thin layer of aluminum as reflector. All measurements and simulations discussed in this section are carrired out with an aluminum coated glass fiber supporting structure cell, referred to as the RIBA Cell, around the crystal.

The light response uniformity of a long tapered LSO/LYSO crystal is affected by three factors. First, the tapered crystal geometry leads to an optical focusing effect, i.e., the response for scintillation light originating at the

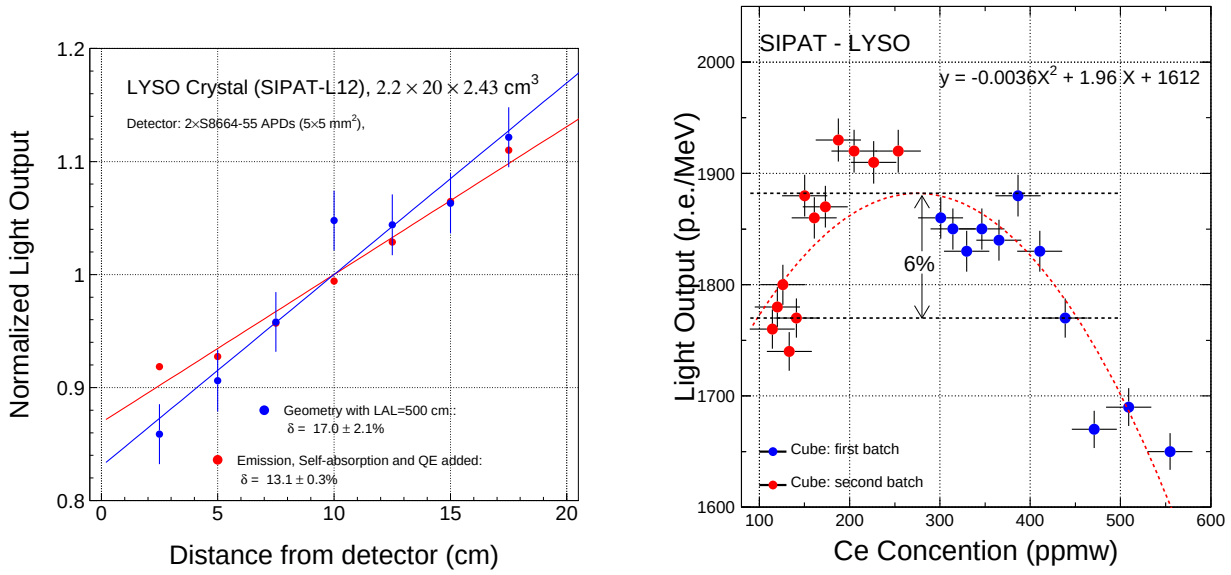

Figure 9.18: Left: Light response uniformities without (blue) and with (red) self-absorption effects, calculated by a ray-tracing program, shown for a 20 cm long crystal with tapered geometry and two Hamamatsu S8664-55 APD readout. Right: Light output measured for 17 mm LSO/LYSO crystal cubes shown as a function of the cerium concentration.

small end far away from the photo-detector would be higher compared to that at the large end, which is coupled to the photo-detector. This is caused by the light propagation inside the crystal, and is common for all optical objects with such geometry. Second, there is a self-absorption effect in LSO/LYSO crystals as discussed in section 9.3.1.2 since a part of the emission spectrum is self-absorbed in the crystal bulk as seen in the left plot of Figure 9.15. This effect is specific for LSO/LYSO crystals. Last, there is a non-uniform light yield along the longitudinal axis of the crystal. It is caused by the segregation process of the cerium activator in LSO/LYSO crystals during growth. Because of the small segregation coefficient (about 0.2) the cerium concentration increases from the seed end to the tail end of the crystal. Such an effect is common for all crystals doped with activator, e.g. CsI(Tl).

The left plot of Figure 9.18 shows the light response uniformities calculated using a ray-tracing program [19] for a SuperB LYSO crystal with tapered geometry and two Hamamatsu S8664-55 APD readout. The blue dots show the uniformity with only the optical focusing effect, and the red dots show the same with the self-absorption effect also included. Numerically, the optical focusing effect alone causes a δ value of 17%, which is reduced to 13% with self-absorption included. This indicates that the self-absorption effect provides a partial compensation for the optical focusing effect. The right plot of Figure 9.18 shows the light output measured for two batches of 17 mm LSO/LYSO crystal cubes (red and blue) as a function of the cerium concentrations determined by Glow Discharge Mass Spectroscopy (GDMS) analysis. It shows that the optimized cerium doping level is between 150 and 450 ppmw because of the interplay between the cerium activator density and the self absorption caused by the over-doping. Also shown in the plot is a second order polynomial fit. By adjusting the cerium doping the light yield difference along the crystal can be minimized. A difference at the level of 10% is more or less the maximum, which may provide a variation of the δ value up to 5%. Taking this into account the initial δ value of the SuperB LYSO crystals may vary between 8% to 18%.

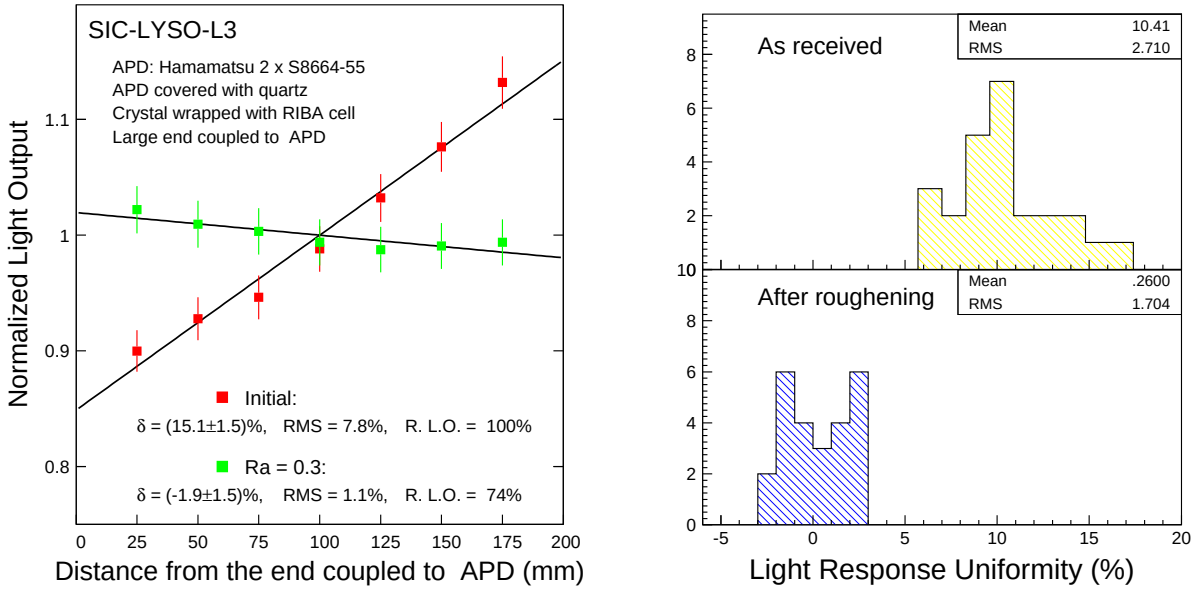

Figure 9.19: Left: Light response uniformity measured with two Hamamatsu S8664-55 APD readout for a tapered SuperB LYSO crystal SIC-L3 before (red dots) and after (green dots) uniformization by roughening the smallest side surface to Ra = 0.3. Right: The distributions of light response uniformity (δ values) are shown for 25 SuperB test beam crystals before (top) and after (bottom) uniformization by roughening the smallest side surface.

Following the experiences of previous crystal calorimeters, such as L3 BGO and CMS PWO, a $|\delta|$ value of less than 3% may be achieved by roughening one side surface of the crystal to an appropriate roughness [21]. The left plot of Figure 9.19 shows the light response uniformities measured with two Hamamatsu S8664-55 APD readout for a tapered SuperB LYSO crystal, SIC-L3. The δ value is reduced from 15% before (red) to -1.9% after (blue) roughening the smallest side surface to Ra = 0.3. The right plot of Figure 9.19 shows a comparison of the δ values before (top) and after (bottom) roughening for all 25 SuperB test beam crystals, showing a reduction of the average δ value from 10% to 0.26%. All 25 $|\delta|$ values after uniformization are within 3%. The reduction of light collection efficiency caused by this uniformization is about 17%. It is expected that one or two Ra values would be sufficient to uniformize mass produced LYSO crystals to achieve $|\delta|$ values of less than 3%.

9.3.1.3 Radiation Hardness

The radiation hardness of long LSO and LYSO samples has been investigated with γ-rays [22, 23] and neutrons [24]. It is found that the scintillation mechanism of this material is not damaged, while other damage can be completely eliminated by thermally annealing at 300°C and does not recover at room temperature, indicating no dose rate dependence [19]. Studies also show that it is also more radiation hard against charged hadrons [25] than other crystals.

Figure 9.20 shows the longitudinal transmittance (left) and normalized average light output (right) for four 20 cm LSO and LYSO samples from CTI, CPI, SG and SIPAT. The light output was measured by using a XP2254 PMT (top) and two S8664-55 APDs (bottom). All samples tested have a consistent radiation resistance, with degradations of the emission-weighted longitudinal transmittance (EWLT) and the light output of approximately 12% for a γ-ray dose of 1 MRad. This radiation hardness

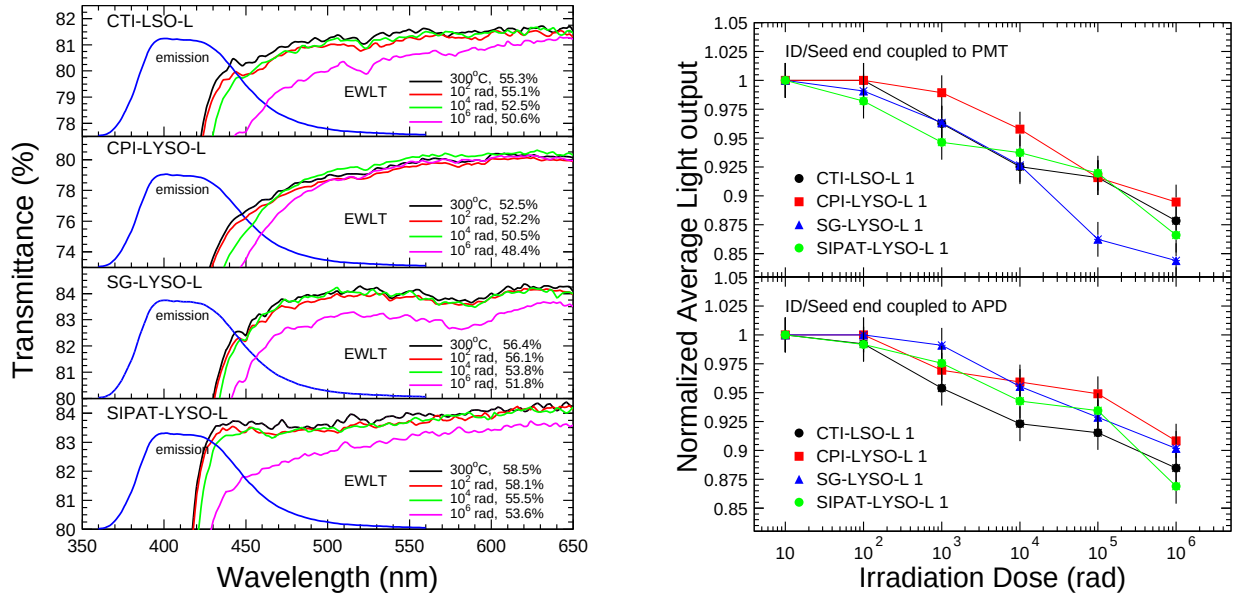

Figure 9.20: The longitudinal transmittance spectra in an expanded view (left) and the normalized light output (right) are shown as a function of the integrated dose up to 1 Mrad for four LSO and LYSO samples of $2.5 \times 2.5 \times 20$ cm^3. Also shown in the left plot is the photo-luminescence spectra (blue) in arbitrary units.

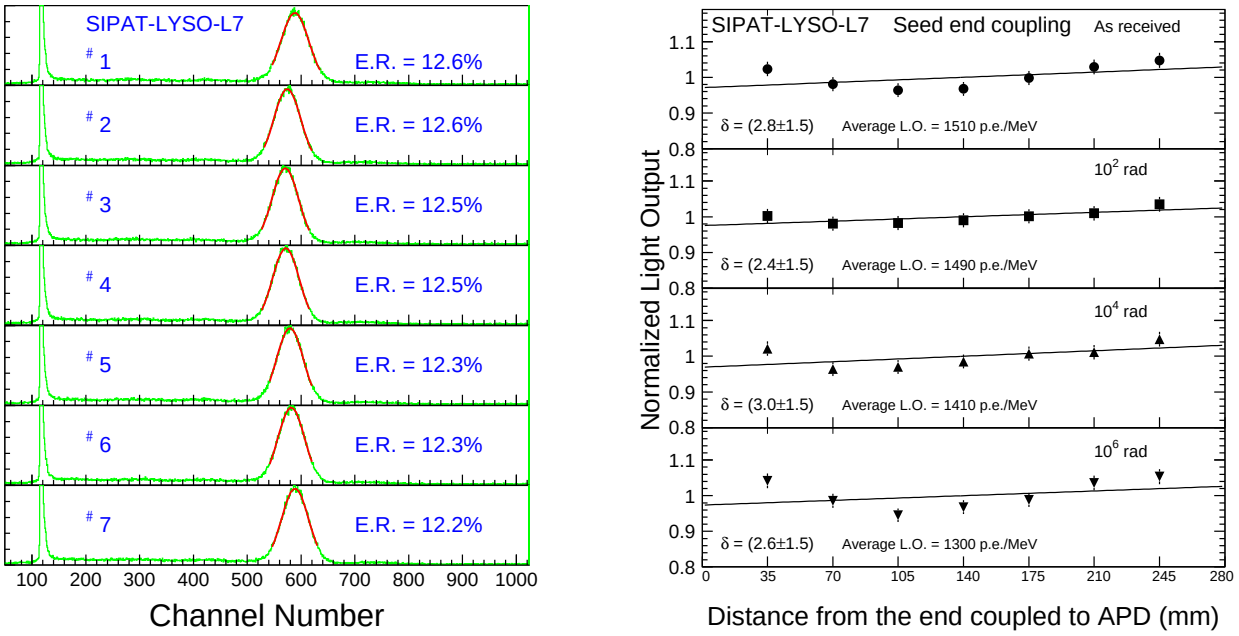

Figure 9.21: Left: The pulse height spectra of 0.511 MeV γ-ray peaks (green) and corresponding Gaussian fits (red) measured by a Hamamatsu R1306 PMT are shown at seven points evenly distributed along SIPAT-LYSO-L7. Also shown are the numerical values of the FWHM energy resolutions (E.R.). Right: Normalized light output and light response uniformity measured by two Hamamatsu S8664-1010 APDs, before and after γ-ray irradiations in several steps up to 1 Mrad are shown for SIPAT-LYSO-L7.

is much better than other scintillation crystals, such as BGO, CsI(Tl) and PWO.

Recently, a 28 cm (25 X_0) LYSO crystal (SIPAT-LYSO-L7) was grown at SIPAT. This LYSO sample has consistent emission, adequate light response uniformity and good radiation hardness against γ-rays up to 1 Mrad [13]. The left plot of Figure 9.21 shows the pulse height spectra measured by a Hamamatsu R1306 PMT at seven points evenly distributed along SIPAT-LYSO-L7. The FWHM resolutions obtained for 0.511 MeV γ-rays from the ^{22}Na source are about 12.5%. This is quite good for crystals of such length. The right plot of Figure 9.21 shows normalized light output and response uniformity measured by two Hamamatsu S8664-55 APD before and after γ-ray irradiations with an integrated dose of 10^2, 10^4 and 10^6 rad. The degradation of the light output was found to be about 13% after 1 Mrad dose. The light response uniformity of SIPAT-LYSO-L7 does not change even after 1 Mrad dose, indicating that its energy resolution may be maintained [19].

In summary, LSO and LYSO crystals are radiation hard crystal scintillators. These crystals are expected to find application in environments where severe radiation is expected.

9.3.1.4 Specifications, Production and Testing

Following our extensive R&D on LYSO crystals, the following specifications are defined for the procurement of high quality LYSO crystals from various vendors for the SuperB forward calorimeter.

- Dimension: +0.0/-0.1 mm.
- Longitudinal transmission at 420 nm: $>$ 75%.
- FWHM energy resolution: $<$ 12.5% for 0.511 MeV γ-rays measured by a Hamamatsu R1306 with DC-200 coupling at 7 points along the crystal.
- Light output will be required to be more than a defined percentage of a small crystal candle with air-gap coupling to PMT.
- Light Response uniformity ($|\delta|$): $<$ 3% measured by two Hamamatsu S8864-55 APDs.

Crystals will be produced by various vendors. The total LYSO crystal volume for the SuperB forward calorimeter is 0.24 m^3 (hybrid version with 3 CsI(Tl) rings), which is small compared to LYSO crystals grown for the medical industry. The following instruments are needed at each of the crystal vendors as well as the SuperB crystal laboratory.

- A station to measure crystal dimensions.
- A photo-spectrometer with large sample compartment to measure the longitudinal transmission along a 20 cm path.
- A PMT based pulse height spectrometer to measure light output and FWHM energy resolution with 0.511 MeV γ-rays from a ^{22}Na source.
- An APD based pulse height spectrometer to measure light response uniformity with 0.511 MeV γ-rays from a ^{22}Na source.

9.3.2 Readout and Electronics

9.3.2.1 APD Readout

The photosensors chosen for readout of the LYSO crystals of the forward endcap are an independent pair of 10×10 mm avalanche photodiodes (APDs). The APDs have several advantages over photodiodes in this application: they are a better match to the emission spectrum of LYSO, providing a quantum efficiency integrated over the spectrum of 75% (see Figure 9.22); they provide useful gain (of the order of 75) with low noise; and, as they have a thinner sensitive region, they suffer less from the nuclear counter effect.

The gain with low noise of the APDs presents two additional advantages: it can allow a reduction of the shaping and integration time constants, constants that, as shown in Sec. **??**, can be used as a handle to fight the machine background; it improves the signal-to-noise ratio for

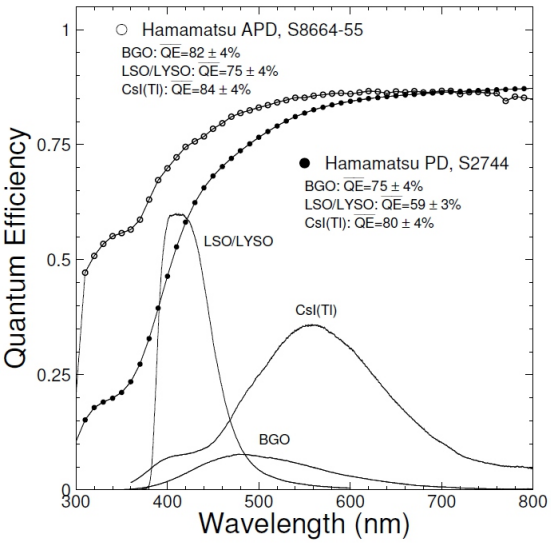

Figure 9.22: Quantum efficiency of a Hamamatsu APD and photodiode, together with the emission spectra of LYSO, BGO and CsI(Tl) crystals.

the signals used for calibration (see Sec. **??**), allowing a crystal by crystal calibration (see Sec. 9.3.3).

9.3.2.2 Electronics Block diagram

this is a test

9.3.2.3 Preamplifier

this is a second test

9.3.2.4 Shaper

9.3.2.5 Digitization

9.3.2.6 Requirements on mechanics

Cables, encumbrances, required cooling, ...

9.3.3 Calibrations

9.3.3.1 Initial LYSO calibration with source

A goal of the design is that the signal rate and the signal-to-noise ratio with a typical radioactive source such as ^{137}Cs be sufficient to allow individual calibration of each crystal with the readout device with which it will actually be paired. As was the case with the existing CsI(Tl) crystals, photodiode readout of large crystals does not allow the use of sources for calibration and setup. This is typically done with a reference photomultiplier, with the results then convoluted with the results of individually calibrated photosensors. Such a procedure does not, of course, fully account for the effects of surface oxidation of the crystal or glue joint losses. However, with APD readout, the response of the entire chain can be measured for the LYSO crystals.

The full setup of each crystal assembly requires each crystal/readout package to be individually adjusted to meet the uniformity requirements *in situ* and the characteristics of each object to be entered into a reference database. This involves appropriate roughening of, typically, one crystal surface to conform to a light collection uniformity specification as discussed in 9.3.1.1. The output of this setup/calibration procedure is then entered into a reference database, which serves as the initial set of calibration constants for the calorimeter system.

The fully assembled calorimeter is then calibrated with the circulated fluorinert system already used in *BABAR* (see Sec. 9.2.2.3) at appropriate intervals (one to four weeks in the case of *BABAR*). A substantial advantage of this approach is that there is an individual pedestal and gain constant for each crystal. A limitation is that the source is at a relatively low energy, although it is at a higher energy than that obtained from long-lived radioactive sources. Calibration with radiative Bhabhas can overcome this limitation, but it requires development of a complex matrix unfolding procedure, since high energy electrons deposit shower energy in many crystals, not in a single crystal as in the case of source calibration. Since LYSO is intrinsically radioactive, some of the endcap crystals will have intrinsic background, and a configurable trigger threshold will be required. A test with LYSO crystals using 6.13 MeV photons from an ^{16}O* state produced with neutrons from a ^{252}Cf source is planned.

9.3.3.2 Electronics calibration

9.3.3.3 Temperature monitoring and correction

The characteristics of APDs place fairly stringent requirements on the temperature control of the system, greater than those imposed by the temperature variation of light output of the crystals, as well as on the stability of the APD power supply voltage.

The Hamamatsu S-8664 APDs specified for the crystal readout have a temperature coefficient of gain of $\Delta G/\Delta T$ of 2.5%/°C, while the LYSO light output varies $-0.2\%/°C$. A specification of an APD gain stability of $\pm 0.5\%$ requires knowledge of the temperature to $\pm 0.2°C$. The CERN beam test demonstrated that a measurement of the calorimeter temperature to 0.2°C can be easily achieved. Furthermore the energy resolution degradation due to machine background might allow to tolerate even a less stringent control.

As far as the overall structure is concerned we can keep the characteristics of *BABAR*: The entire calorimeter is surrounded by a double Faraday shield composed of two 1mm-thick aluminum walls, so that the diodes and preamplifiers are shielded from external noise. This shielding also serves as an environmental enclosure, surrounding the slightly hygroscopic CsI(Tl) crystals with a dry, temperature controlled nitrogen atmosphere. The preamplifiers (2×50 mW/crystal) and the digitizing electronics (∼3 kW per end-flange) are the primary internal heat sources. The temperature was monitored by 256 thermal sensors distributed over the calorimeter. This system maintains the crystal environment at $20 \pm 0.5°C$. Dry nitrogen circulation stabilizes the relative humidity at $1 \pm 0.5\%$.

As far as gain stability is concerned, for a gain of ∼75, with a reverse bias voltage of ∼375 V, a voltage stability of better than 1 volt is required. This requirement can be met by commercially available computer-controlled high voltage supplies, such as those used for the CMS calorimeter.

9.3.4 Mechanical Structure

For cost-savings, the forward mechanicl structure from*BABAR* is reused. It is designed in order to minimize the inactive materials, as well for the barrel, and to provide hermeticity at interface with barrel itself. The design is conceptually different from that of the barrel. In fact, while the barrel remained unopened for the lifetime of *BABAR*, the endcap is capable of rapid mounting and dismounting, always keeping precision mating to barrel itself. The forward endcap is a conic section, with front and back surfaces tilted at 22.7 to the vertical, in order to match the drift chamber endplate. It is built in 2 monolithic parts able to allow an easy and quick demounting for access to inner components of detector; its total weight is approximately 4 tons (forward assembly drawing in Fig. 9.23). It is supported off the solenoid coil and precisely aligned with the calorimeter barrel; in particular it is the designed to minimize both the material and the air gap between the two parts.

9.3.4.1 Crystals

The *BABAR* forward endcap has a total of 900 CsI(Tl) crystals, made up from nine distinct radial rings (3×120, 3×100, 3×80), arranged to give approximately the same crystal dimensions everywhere; total crystals volume is 0.7 m^3. CsI(Tl) , grown in a polycrystalline form, presently populate the cells of the endcap modules. This is a soft material, not able to support load; for this reason the CFC structure support the individual crystals, avoiding load transferring to neighboring cells; CFC with 250 μm wall thickness is chosen because this presents the best compromise between strength and minimum radiation length. The design and dimensions of these crystals are described in Figure 9.24.

The CsI crystals fit loosely into their compartments; in fact they have been produced with a tolerance on crystal transverse dimensions of ∼225 μm. Each crystal is read out at the back with 2 large areas photodiodes (Hamamatsu S2744-08). The 2 diodes are glued onto a 1 mm polystyrene coupling plate which itself

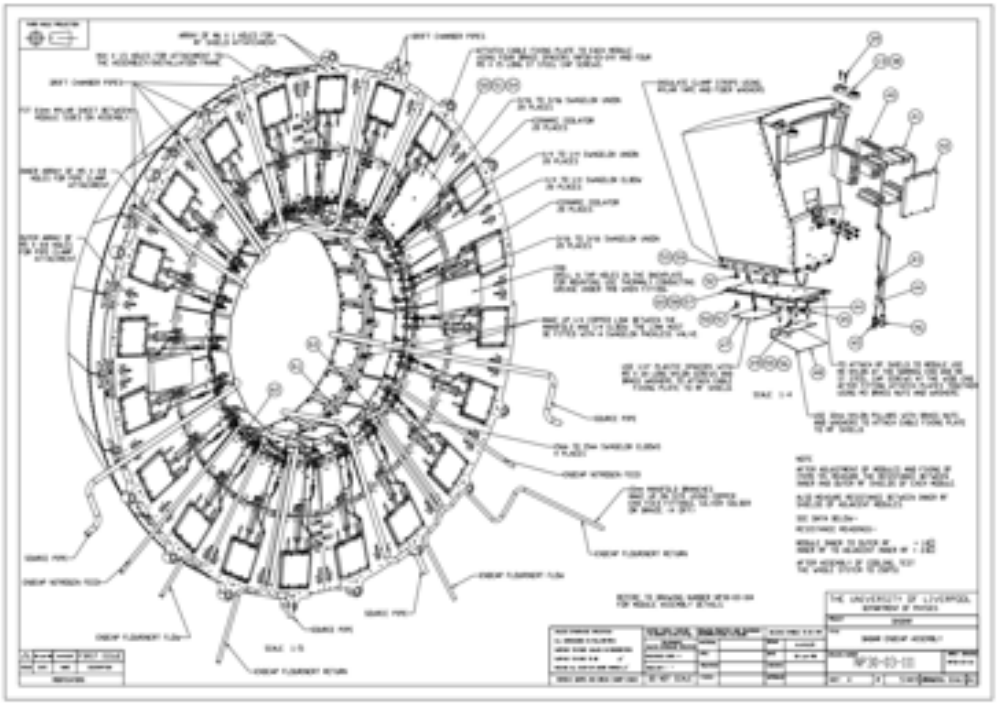

Figure 9.23: Forward assembly drawing

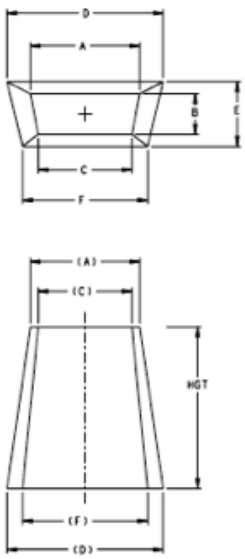

θ Row	Number Needed	Volume (cc)	A (cm)	B (cm)	C (cm)	D (cm)	E (cm)	F (cm)	Height (cm)
1	80	741.0	4.298	4.670	3.944	4.995	5.426	4.583	32.55
2	80	802.4	4.641	4.670	4.289	5.394	5.428	4.985	32.55
3	80	863.6	4.982	4.670	4.632	5.792	5.430	5.386	32.55
4	100	739.6	4.247	4.670	3.970	4.941	5.432	4.618	32.55
5	100	788.3	4.519	4.670	4.244	5.257	5.433	4.937	32.55
6	100	836.9	4.790	4.670	4.517	5.573	5.433	5.256	32.55
7	120	737.7	4.209	4.670	3.984	4.898	5.434	4.636	32.55
8	120	778.4	4.437	4.670	4.214	5.162	5.433	4.903	32.55
9	120	819.1	4.665	4.670	4.445	5.427	5.432	5.171	32.55

Figure 9.24: Definition of the sides of the crystals and their values in BaBar.

is glued onto the crystal surface. The crystals (Fig. 9.6) are wrapped with a double layer of Tyvek (150 μm each) to improve the light yield, a layer of Aluminum Foil for electrical shielding (75 μm) and a layer of Mylar (12 μm) for insulation and mechanical protection of Al foil. Furthermore there is a small aluminum box covering the photodiodes at the back of crystals, and containing the PC-board with preamplifiers.

In the hybrid scheme, we plan to replace the inner six rings of CsI(Tl) crystals with LYSO. As the Molière radius of LYSO is smaller, the replacement will be four LYSO crystals for each CsI crystal. In this way, the same structure is used, simply inserting four LYSO crystals into each CFC cell. LYSO is a very strong crystal, so no additional support is required between them. If further cost saving in the initial implementation is required, additional rings of CsI may be kept from the *BABAR* endcap. A future

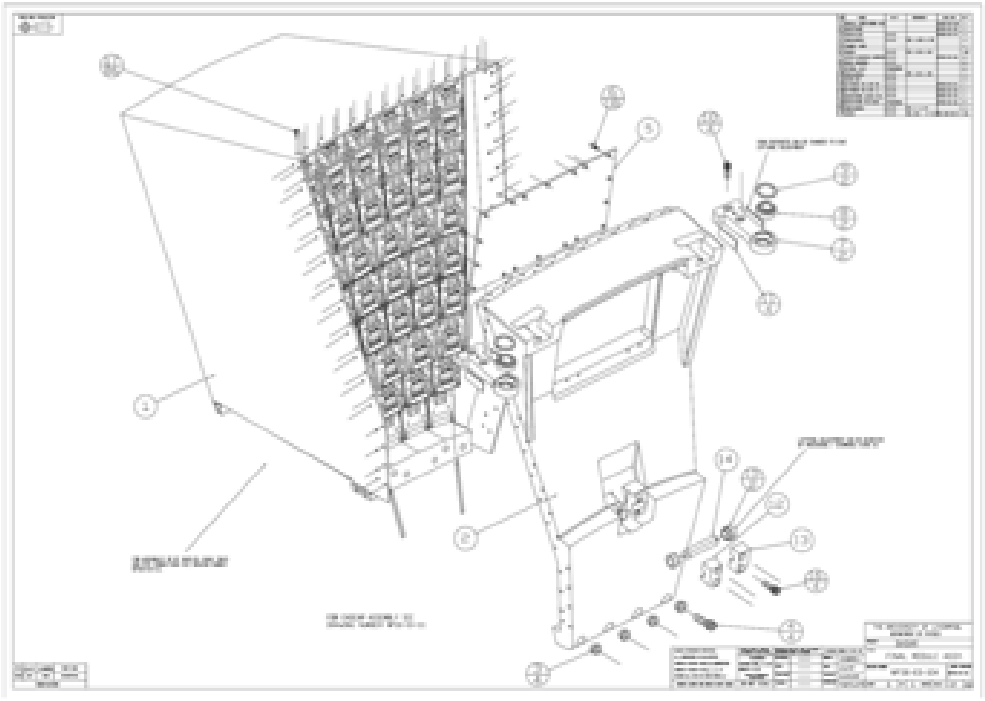

Figure 9.25: Forward module assembly drawing

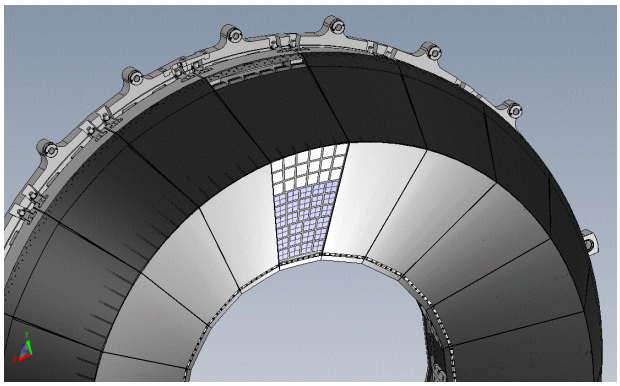

Figure 9.26: Layout of a module in the forward endcap in the hybrid plan.

upgrade of the detector could include replacing more rings of CsI with LYSO.

9.3.4.2 Modules

The geometry is basically projective, with the crystal axes pointing to an axial position 5 cm from the interaction point. In order to preserve optimum light collection and both spatial and energy resolution, similar-sized crystals have been used, arriving to a layout of nine rings of trapezoidal shaped crystals, grouped in 3 super-rings and arranged in 20-modules symmetry (Final Module drawing in Fig. 9.25).

As described above, we replace the six inner rings of CsI with LYSO. This is shown in Fig. 9.26.

9.3.4.3 Installation

A series of dedicated tools and instruments already exists, and a detailed procedureis under preparation, derived from *BABAR* for moving and installing the forward calorimeter. Existing tooling is being located at SLAC, as well as the documentation on the assembly and mounting of the 20 modules on the support backplate. Fig. 9.27 shows the exisitng Installation Bridge, able to move individually each one of the two monolithic endcap halves.

9.3.4.4 Refurbishment of the BaBar structure

As for the *BABAR* barrel, the andcap will be disassembled to the module level for transport.

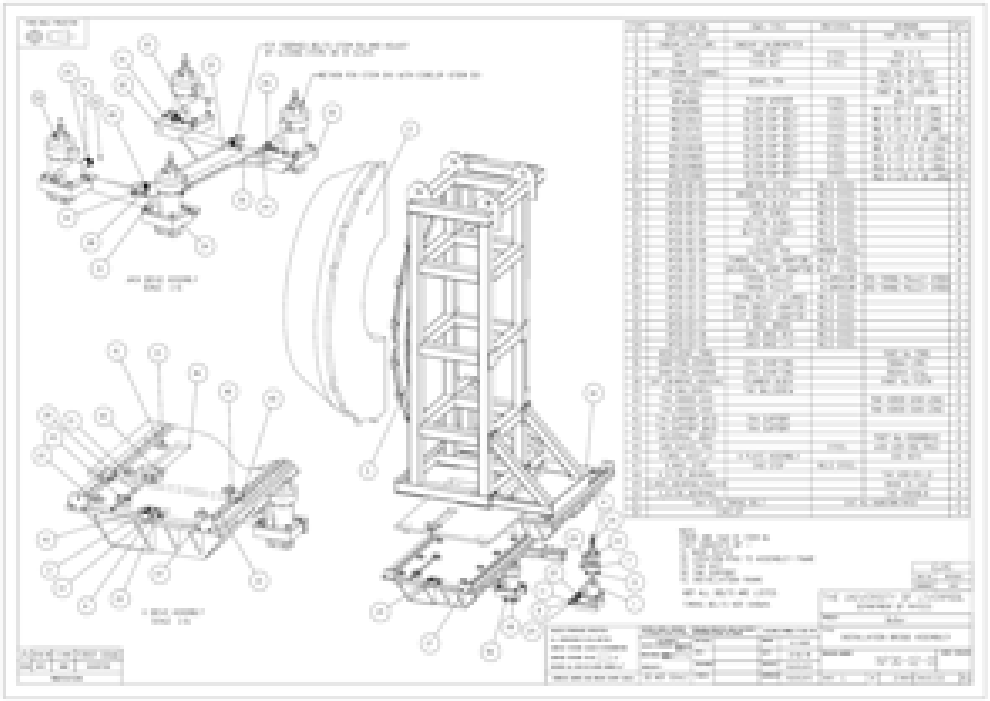

Figure 9.27: Installation Bridge drawing

The alternative of transporting each half with modules installed carries mechanical risks, but may be investigated further. Most of the tooling for handling the endcap and modules exists at SLAC, and may be used after some refurbishing.

For the CsI(Tl) rings that are kept, each crystal and preamp will be tested and measured for signal strength, both before and after shipment. Repairs will be made as necessary. The testing in Italy may be done at a remote site at the module level, both for the CsI and the LYSO crystals. Final assembly of the endcap and installation onto the detector is best done at Tor Vergata.

The electronics for the forward calorimeter will be refurbished as for the barrel (section 9.2.4 for the CsI(Tl) rings that are kept. The LYSO readout is with APDs, with new electronics as described in 9.3.2.

9.3.4.5 Spare FWD modules survey and tests

In order to study the changes required for the LYSO crystals, two spare *BABAR* endcap structural modules have been shipped to Italy. Tests and measurements on them will be necessary to define a procedure for LYSO crystals insertion, and investigate any problems implicit inside this operation (electronics for example), and to check and validate technical information presently available; in particular regarding the CFC honeycomb region.

9.3.5 Tests on Beam

9.3.5.1 Description of apparatus

Two beam tests have been performed with a prototype LYSO matrix, one at CERN in October 2010 and one at the Beam Test Facility (BTF) in Frascati in May 2011. In both cases the prototype matrix was composed by 25 LYSO crystals of pyramidal shape with dimensions 2.3cm×2.3cm×22cm inserted in a support structure assembled by the RIBA company (Faenza, Italy) described in detail in Sec. 9.3.4. To improve light output uniformity, each crystal presents a black band of 15mm at the end of its smallest face and the area of the face not covered

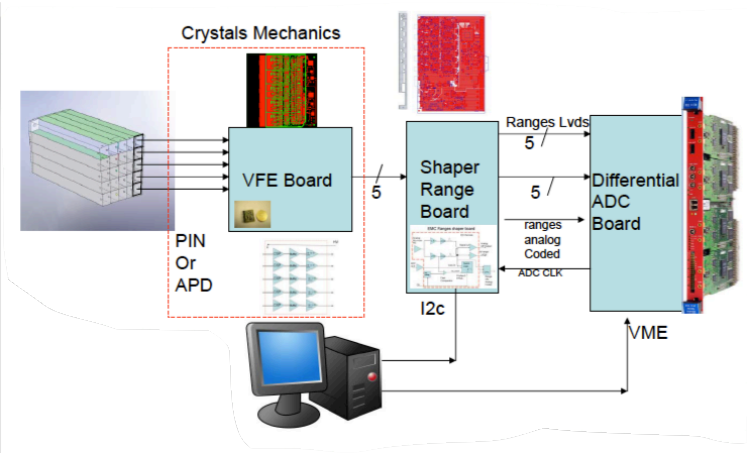

Figure 9.29: Schematic view of the electronic chain for the forward EMC.

by the APD (or PiN) is painted with a reflective white painting. The mechanics is composed of glass fiber, covered with copper foils $35\mu m$ thick. Between one cell and the other there is a nominal thickness of 200 μm, while the external side has a thickness of 135 μm. Fig.9.28 shows a picture of the Test Beam structure with inserted one row of crystals. Of the crystals,

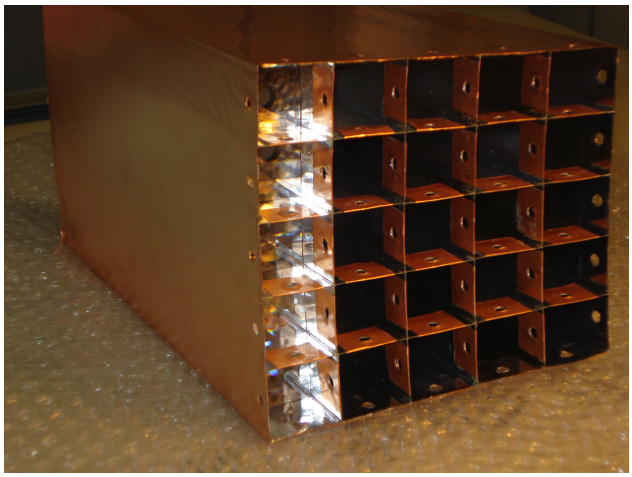

Figure 9.28: Picture of the Test Beam mechanical structure with one raw of LYSO crystals.

20 are read out with an Avalanche Photodiode (APD) in both tests while the remaining 5 are read out with PiN Diodes at CERN and with APDs at the BTF. As shown in Fig. 9.29, the readout chain is composed of: a front end board (VFE) that contains a Charge Shaper Preamplifier (CSP); Shaper Range Board which completes the attenuation, already applied in the VFE board, and then divides them according to the energy. Two different ranges are foreseen in the treatment of the signals, for energies lower than 200 MeV and for energies greater than 200 MeV, although in the tests on beam the amplifications have been adjusted to use only one range; a 12 bits Caen ADC to process the signals and digitize the analogue outputs. In order to avoid saturation effects the APD's were biassed at 308V.

9.3.5.2 Description of the beams

The Beam Test at CERN has been performed at the T10 beam line in the East Area. The beam is mainly composed of electrons, muons and pions created by the scattering of protons into aluminum and tungsten target. The composition of the beam is highly dependent on the energy and for electrons it ranges from 60% at 1 GeV to 1% at 6 GeV. The maximum energy reachable at this beam line is 7 GeV with a nominal momentum spread $\Delta p/p \simeq 1\%$. The distance between the end of the beam line and the matrix is about 15 m. The event rate is of the order of 1 Hz. Fig.9.30 shows the experimental setup used at CERN, it is composed of a Cherenkov detector

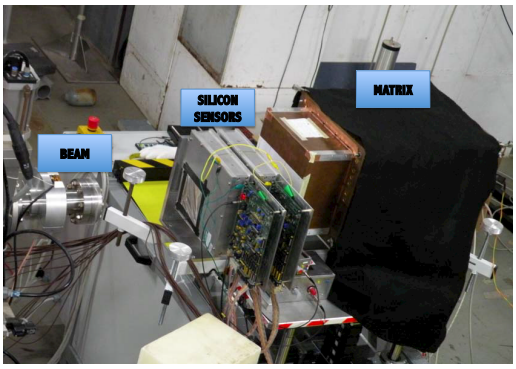

Figure 9.31: Schematic view of the test beam setup used at the BTF in Frascati.

for the electron-pion discrimination, two scintillators (finger counters) $2\times2cm^2$, the box containing the matrix and the VFE boards.

Figure 9.30: Schematic view of the test beam setup used at CERN.

The two scintillators of the fingers act as trigger while the information of the Cherenkov detector was both stored in order to select Minimum Ionising Particles (MIP) used for the calibration and used to prescale the triggers.

The Beam Test Facility in Frascati is part of the ΦFactory, DaΦne. It is composed of a linear accelerator LINAC, one spectrometer and two circular accelerators of electrons and positrons at 510 MeV. The LINAC is the same which supplies the test beam line at the BTF. The pulsed beam of the LINAC circulate electrons up to 800 MeV at a maximum current of 550 mA/pulsation and positrons at a maximum energy of 550 MeV with a current of 100 mA/pulsation. The typical duration of a pulsation is 10 ns, with a frequency of 50 Hz. A bending magnet select electrons of a given momentum, a line of about 12m contains quadrupoles for the uniformation of the beam and a system of slits allow to change the flux of arriving particles. The beam energy spread is 1% at 500 MeV. The setup for the beam test of the matrix at the BTF is shown in Fig.9.31. The setup shows the end of the electron beam line, four planes of silicon strip detector (two measurements in x and two measurements in y) and the box containing the matrix with the crystals and the VFE boards. As mentioned before, at the BTF all the crystals are equipped with APD's, and it should be mentioned that the gain of the VFE has changed with respect to CERN from 0.5 to 1, while an amplification factor has been introduced. To control the position of the beam with respect to the matrix a detector of 16 x 16 scintillating fibers of 3mm each has been used. The LINAC radiofrequency (25 Hz) was taken as trigger.

Since the beam energy spread of the CERN facility proved to be significantly larger than the specifications, based on the performances of the detector at the BTF, we will use the CERN TB data only to study the linearity at high energy, while resolution studies will be performed exclusively on the BTF data.

9.3.5.3 Description of data and calibration

For each triggered event, the output of the readout are the waveforms of the 25 channels, each constituted by 384 samples. The signal amplitude in each channel is defined as the maximum of the waveform, extracted from a gaussian fit to the sampling distribution, subtracted of a pedestal. For each crystal, the pedestal is calculated averaging the first 60 samples on a reference run. The pedestal-subtracted amplitude is considered to be the measurement of an energy deposit if it is above a threshold chosen to be three times the noise fluctuation, whose value is determined from a run taken with random triggers where no signal is present. After calibration the energy of the electron that ini-

tiated the shower, was estimated by summing all the energy deposits in all crystals ("cluster energy").

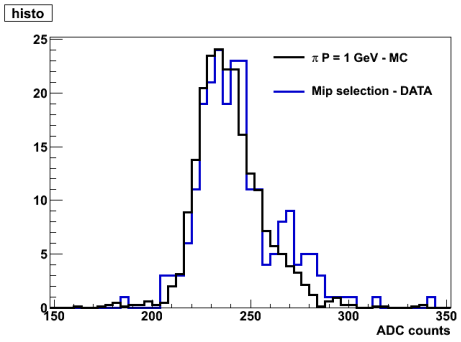

Figure 9.32: Comparison between data and MC of the energy deposited in the MIPs sample. The hypothesis that after the selection the beam is dominated by pions is made.

At the CERN test beam hadrons traversing the crystals horizontally were selected as Minimum Ionizing Particles (MIPs) by requiring no significant signal in the other crystals and a signal consistent with an hadron in the Cherenkov detector. Profiting from the fact that MIPs release a constant amount of energy regardless of their energy, the amplitude spectra of each crystal was fitted to extract the most likely value. After determining on the simulation the expected released energy in each crystal (Fig 9.33) , the corresponding calibration constants could be extracted.

At the BTF test beam, where no hadrons were available, the relative intercalibration constants were obtained on the electron sample itself. The relative cluster energy resolution was minimized by floating a constant in front of each crystal a part from the central one. The overall energy scale was then determined from the knowledge of the beam energy. This procedure was applied on a small fraction of the runs where the electrons were approximately 500 MeV (the highest energy reached in the tests) and the corresponding constants used in all other runs. This intercalibration was also cross-checked by means of cosmic-ray data obtained with an ad-hoc trigger made of two plastic scintillator pads positioned above and below the crystal matrix. The channels where there is a significant difference are those where the electron data see very little energy because they are far from the center of the matrix. In such cases, that have little impact on the resolution studies since they contribute little to the total energy measurement, the calibration constants estimated on the MIPs are used.

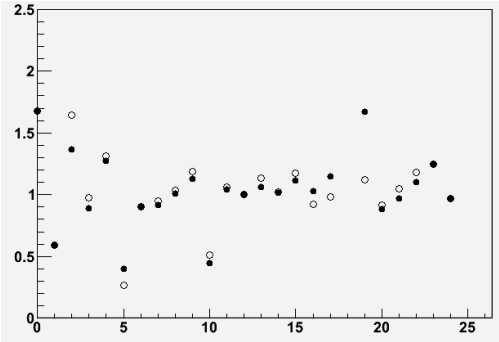

Figure 9.33: Comparison between electron and MIPs calibration at the BTF test beam as a function of the crystal number. Calibration constants are referred to crystal 12 that is therefore by definition equal to unity.

9.3.5.4 Electronics noise measurements

The first information we could extract from the data are the characteristics of the electronic noise. From the signal distribution in a random trigger run at the BTF we estimated (Fig. 9.34) that a part from two channels, the noise is on average 2ADC counts. After applying the calibration, this noise corresponds to approximately 0.4MeV. To understand if there were resonant components, the noise of each crystal i was analyzed in the Fourier space, by estimating its power spectrum from waveforms acquired with a random trigger:

$$\mathrm{PS}_i(\omega_k) =< n_i(\omega_k) n_i^*(\omega_k) > . \qquad (9.6)$$

The estimated power spectrum of a representative channel is shown in Fig. 9.34, where it can be seen that the dominant source of noise is in the range 0-8 MHz, which corresponds to the

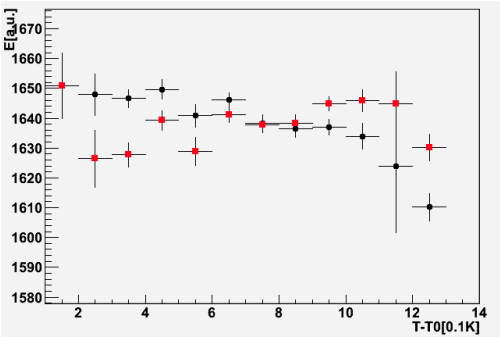

Figure 9.35: Dependence of the measured energy on the temperature before (black dots) and after (red squares) correction.

frequency bandwidth of the shaper. Sources of noise occurring after the shaper give a negligible contribution, while those occurring before are filtered according to the shaper transfer function and dominate.

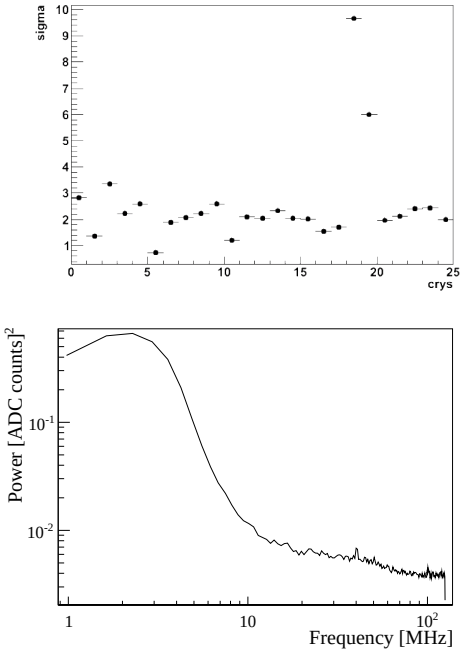

Figure 9.34: Top: Noise RMS for each channel of the BTF test beam. Bottom: power spectrum of a representative channel.

Also the presence of noise correlation among the crystals was estimated and found to be negligible.

9.3.5.5 Temperature corrections

A temperature dependence of several percent per degree is expected both in the light yield of the LYSO crystals and in the gain of the APDs. At the CERN test beam the position of the MIP peak as a function of the temperature measured by sensors places on the rear of the crystals has been used to extract the temperature correction (Fig. 9.35) : $E_{corr} = E_{raw}/(1 - p_0 * (T - T_0))$ where $p_0 = 2.8 \pm 0.2 \times 10^{-3}$ and $T_0 = 34$K. The same figure shows also the effect of the correction.

This correction proved irrelevant at the BTF test beam where the temperature was controlled to better than 0.2^oC

9.3.5.6 Results

In order to estimate the linearity of the response and the energy resolution, the distribution of the cluster energy is fitted for each beam configuration with a crystal ball function. The mean value of the gaussian component is considered as estimate of the energy, while the resolution is evaluated as starting from the FWHM of the whole distribution.

Fig. 9.3.5.6 shows the mean value as a function of the energy for the data collected during the CERN test beam. The linearity of the response is thus ensured.

At the BTF the beam was configured to be able to observe multiple peaks due to up to three simultaneous electrons impacting the crystal matrix. This allowed to have more than one resolution measurement for each beam energy configurations (see Fig. 9.3.5.6). In turn, this allowed to estimate the dependence of the beam spread with the energy by comparing measurements of the same amount of deposited energy, but obtained with different beam energies. The intrinsic resolution obtained by subtracting the measured beam spreads in quadrature from the average resolutions is also shown in Fig. 9.3.5.6.

Such intrinsic resolutions are then compared with the results of a full simulation of the experimental setup (Sec. 9.1.2). There is a good

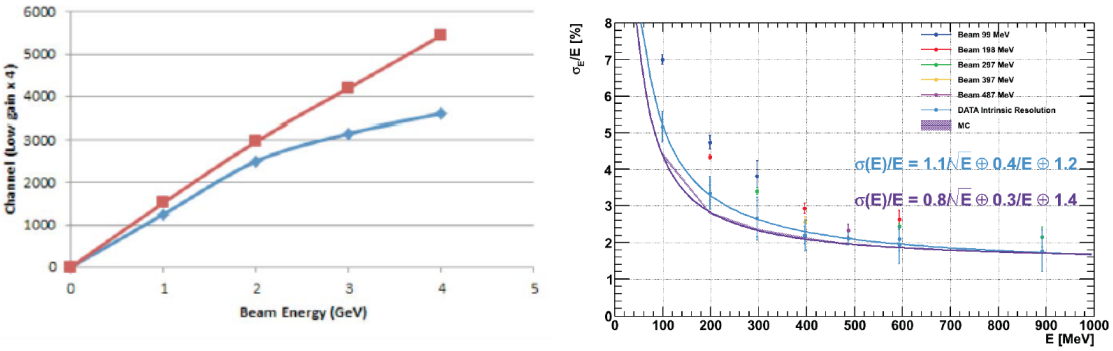

Figure 9.36: Left: **PLACEHOLDER** Measured mean value (in arbitrary units) as a function of the beam energy at the CERN test beam. Right: relative resolution as a function of the deposited energy on data and MC simulation.

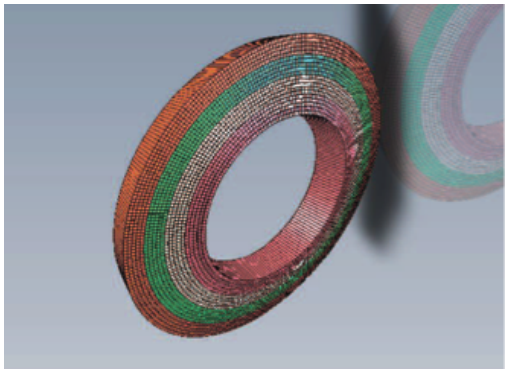

Figure 9.37: overview of the structure of the FWD EMC.

agreement, with a resolution smaller than 2% at 1 GeV.

9.3.6 Alternatives

9.3.6.1 Full LYSO calorimeter

The technically best solution for the forward calorimeter is to construct a new device using LYSO crystals throughout, with a thin mechanical support structure to minimize material. We have pursued extensive R&D into this option. It is not chosen as our baseling purely for cost considerations, and remains as an alternative should funding materialize. This section summarizes this alternative design.

The driving design principles are the same that were used for the *BABAR* Electromagnetic Calorimeter (see Sec. 9.3.4), the biggest change being induced by the higher density of the LYSO crystals: this allows for Molière radiuses that are around a factor two smaller and also the required length of the crystals is significantly smaller. This changes both the size of the cells and the position of the center of gravity, thus altering significantly the design. A detailed report of the studies that were carried out is in Ref. [26], here we only stress the relevant points.

The proposed structure is made of four rings in theta (see Fig. 9.37) each composed of 36,42,48, and 54 modules respectively. The cells are designed in order to keep the cell front dimension.

Services have not been studied in detail yet, but *BABAR* standards should be reasonably suited and also the reduced crystal size leaves further room for them.

Module design

Modules contain a 5 x 5 matrix of crystals and therefore their approximated dimensions are 110 x 110 x 230 mm^3 and the total weight of the crystals is about 25kg. The requirements on the thickness and the material of the walls constrain the module to be held in a very light container of 220g, thus making the mechanical requirements challenging.

Considering the ϕ and θ symmetries the number of crystals types that need to be produced is reduced to 20. To achieve the required energy resolution, crystal-to-crystal separation must be less than or equal to half a millimeter. The design guarantees a maximum distance between

crystal faces of 0.4 mm within a module and of 0.6 mm across two modules, either in ϕ or in θ for crystal nominal dimensions. For the crystals with the smallest tolerances these values are reduced by 0.1 mm .

As described in Fig 9.38 Alveolar modules are assembled into the Shell-Support-Structure (horse collar and wedge). Alveolar front ends are driven into position by 5 tubular CFRP setpins and the front of the module is glued to the structure front plate.

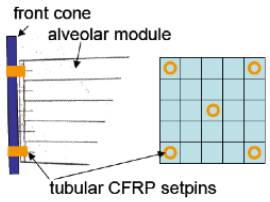

Figure 9.38: Alveola supports.

To validate the submodule design, two prototypes of the alveola module have been constructed (see a photo in Fig. 9.28). A first prototype (Proto1) was produced to validate the cell structure concept and the production economy It was then used with its 25 crystals in a beam of particles for physics validation The Proto1 validated the whole production process and a 3D dimensional inspection performed on the internal and external walls gave evidence of the achievable dimensional tolerances. Wall thickness was measured at the cell open edge over 20mm depth on both sides of punched holes and produced the following values : a) for internal walls nominal 0,200mm 0,15 to 0,22 b) for external walls nominal 0,135mm 0,13 to 0,17

The information gathered have been used to define the production protocol.

A second prototype (Proto2) was produced in September 2011 to confirm process repeatability and to evaluate the global mechanical properties of the structure.The alveolar module is identical to that used for the physics beam test in October 2010, Proto1. The test campaign had the aim to evaluate the structure overall mechanical properties. Global deformations of the alveolar array are significant, and a loading test is essential for checking the absence of interference with the shell inside (inner and outer cone) and the absence of crystal stressing (cell bending ¡ play) in a first approximation. As shown in Fig. 9.39, the cells were loaded with dummy crystals that simulate the mass and different gravity vectors have been investigated. The mechanical tests performed on the modular structure provided basic input data to a Finite Element Analysis of the complete support structure.

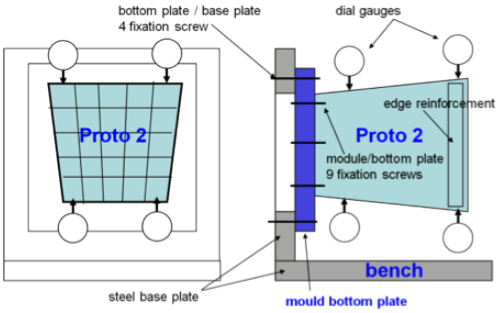

Figure 9.39: Alveolar module test setup

Alveolar module structure finite element analysis

A detailed Finite Element Analysis was performed on the alveolar structure using material properties form data-sheet. An approximated module based on surfaces, shown in Fig. 9.40, has been used as a reference to to validate the Global Finite element model of the whole EMC. On the external wall two laminae of total thickness 0.2mm were used, together with four internal walls laminae at 0^o, 90^o,0^o, 90^o. The bottom material is isotropic of 6mm aluminium material equivalent to CFRP. 5 constraint point are putting to the centrer of 5 holes on the module bottom, (2 on the upper side 2 lower side and 1 in central position, to simulate the setpins constraints to connect the module to the mechanical forward structure), for this was used the rigid elements (rigid bar) leading the center node hole to boundary hole.

The load is the weight of crystals and each one has mass of about 1 Kg. For this purpose to simulate it, a "rigid bar" with 5 nodes was

Table 9.4: Expected ply stresses and index failures.

case (^{o})/ coordinate	Ply Stress(MPa)	index failure
0/x	35	1/48
0/y	2.6	1/10
0/z	1.4	1/16
90/x	5	1/342
90/y	10	1/2.6
90/z	1.7	1/13
180/x	30	1/57
180/y	7	1/4
180/z	1.5	1/15

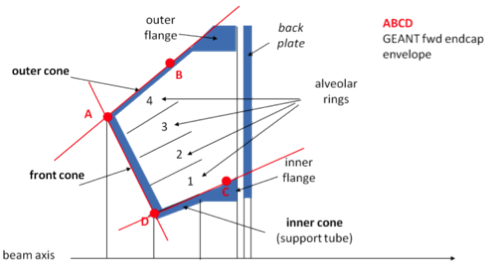

Figure 9.42: Support shell structure

used along the centre alveolar cell, and a lumped mass 1/5 of crystal weight is positioning in each of this nodes. This nodes are then connected with some nodes near alveolar walls with rigid bar and from these latter to the alveolar walls nodes with "gap and spring" elements.

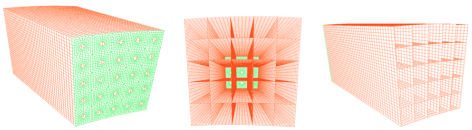

Figure 9.40: Alveolar module finite element model

The resulting stresses predicted on the structures are depicted for the 0^o case as an example in Fig. 9.41. The corresponding values for the ply stresses and for the index failure (i.e. the ratio between the predicted stress and the breakdown) are summarized in Tab. **??**.

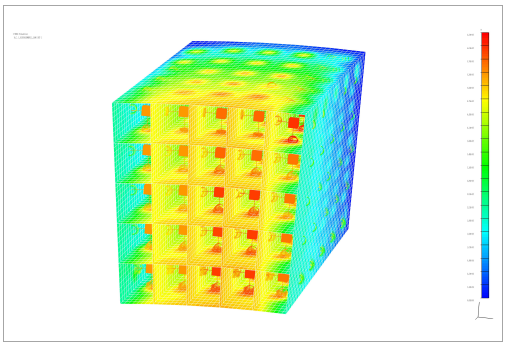

Figure 9.41: Results of the module finite element model at 0^o,

Support shell structure design

The shell, shown in Fig. 9.42, consists of the outer cone and front cone as one single solid body in CFRP. The inner cone, where material budget does not pose too stringent limits is a metallic shell. Back plate is the same as BaBar. The volume is defined by the line AB, AD, CD while A'B' and A'D' are construction lines resulting from technical choice.

The outer cone end is reinforced by a metallic ring for easy connection with the back plate. The back plate provides the EMC interface with the SuperB bearing points (position reference and transmission of loads). The alveolar array is cantilevered from the shell front cone as detailed in Fig. 9.43.

This configuration provides a logical construction and assembly sequence, in particular an easier and almost reversible access to the most delicate part of the detector, its crystals and photodiodes. There is no connection between the alveolar array and the inner and outer cone inner faces. A 1mm gap is introduced for the free elastic deformations of the alveolar array and of the shell. The front cone is connected to the inner cone by gluing secured by screws.

The outer cone is a massive CFRP (6 to 10mm) while the front cone is either a massive CFRP or a sandwich plate 20mm thick. For

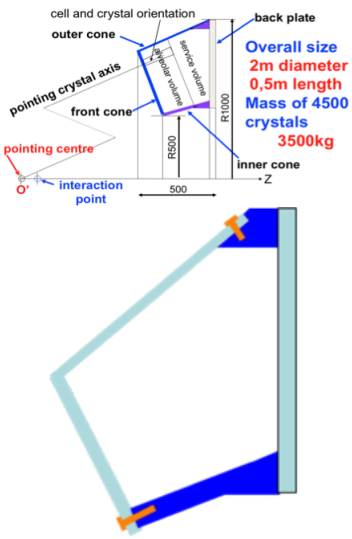

Figure 9.43: Support shell assembly

the production the mould is at the inner face of the outer-front cone in order to have high dimensional accuracy at the interface with the crystals modules, while a vacuum bag is at the opposite side; the parietal aluminum wedge is embedded in the structure The inner cone is a precise CNC machined massive Al 7075 piece with a thickness of 20mm.

9.3.6.2 Pure CsI

Description

Performance, tests

Mechanical changes

Electronics changes

9.3.6.3 BGO

Prior experiences with calorimeters made of BGO crystals in high energy physics come from L3 [28] and Belle [29]. In the first case BGO was used for both Barrel and Endcaps, while Belle used BGO to build the Extreme Forward Calorimeter with the purpose of improving hermeticity close to the beam line and monitor beam background. Such knowledge will be summarized here, integrated by tests that were performed to account for the particular operating conditions expected in the case of SuperB: short integration time, needed to reduce pile-up, and large radiation.

Resolution

The properties of the BGO crystals are summarized in Tab. 9.2: the mechanical properties are similar to LYSO, but with a light yield four times smaller. The scintillation time is intermediate between the LYSO and the CsI, reason for which a good performance in a high rate environment is possible.

The performances of the L3 calorimeter, read by pin-diodes were $\sigma_E/E = (1.6/\sqrt{(E)} \oplus 0.35)\%$ and $\sigma_\theta = ((6/\sqrt{(E)} \oplus 0.3) mrad)$, i.e. the statistical term of the resolution at 100MeV was 4%. Later studies with APDs [30] show that the system produces $\sim$ 420 p.e./MeV, i.e. the statistical term at 100 MeV would be 0.5%, i.e. well within the requirements.

Nonetheless, due to the requirements dictated by machine background (Sec. 9.1.1) we will not be able to operate the detector integrating over even as much as a decay time of the crystal. The degradation in resolution induced by the integration time was tested specifically for this application in the INFN-Roma1 electronics laboratory with a single $2 \times 2 \times 18$ cm^3 crystal. 660 keV photons from a radioactive source were detected with a crystal read at both ends by two EMI-9814B PMT. The waveforms of the signals provided by the PMTs were acquired by a Lecroy digital oscilloscope, having a bandwidth of 300 MHz and used with a sampling rate of 250 Ms/s. One of the two signals was used to trigger the oscilloscope. The other signal was processed with an Ortec-474 and acquired by scope. The Ortec-474 module has an integration time (RC) that can be choosen between 20, 50, 100, 200, and 500 ns.

For each value of RC a run was recorded and for each pulse shape both the total charge, independent of the total time, and the maximum amplitude, the quantity that will eventually be used in the experiment. The resolution on the charge was found to be 9.5% consistent with 130 p.e./MeV after detection and independent of the integration time of the ORTEC. The resolution on the amplitude depends instead on the latter, as shown in Fig. 9.44 and compared with the expectations from a simple Monte Carlo simulation where only the effect of the photo-

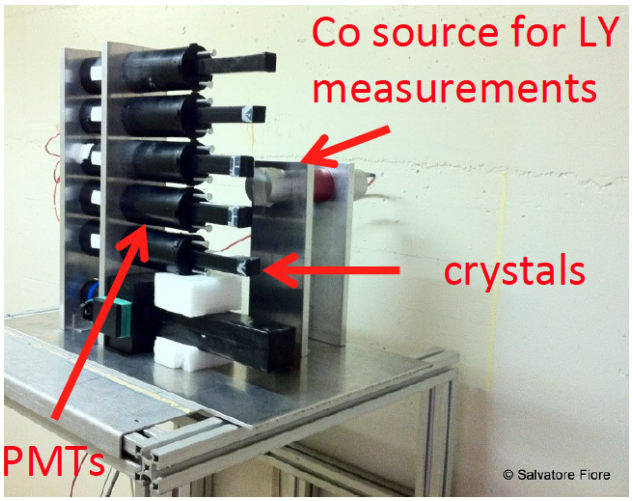

Figure 9.45: Experimental set-up for LY measurements. Crystal samples are shown while mounted on the PMTs. Crystals were coupled to the PMTs during low-dose irradiation, and data were acquired by shutting down the source for few minutes.

electron statistics is included [27]. This results shows that shortening the integration time the resolution worsens, but only moderately. For instance even integrating only for 20ns, compared with the 300ns scintillation time of the crystal, the contribution to resolution due to the photostatistics worsens only by 60%.

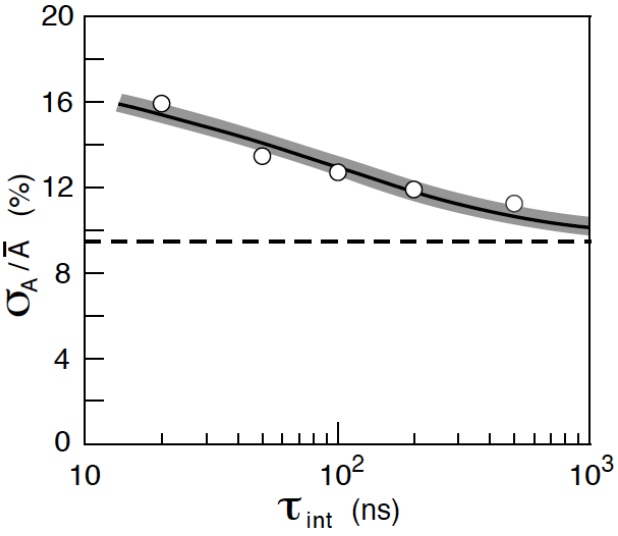

Figure 9.44: Resolution on the measurement of the total charge (dashed line) and the amplitude of the pulse shapes (dots)as a function of the integration time. The results of a Monte Carlo simulation are superimposed (shaded line).

Radiation Hardness

The BGO rad-hardness was tested up to 90Mrad [29, **?**]. After a drop of about 30% in the first 20Mrad of integrated dose the crystal light yield plateaus. It will nonetheless recover up to 90% of the original light yield in approximately 10 hours and it is not documented what will happen if after this pre-irradiation the crystal receives a small dose further. For non irradiated crystals a dose of 115krad implies a light yield loss of 30% that fully recovers with a lifetime of $\sim$ 1 hour. Furthermore, these results refer to undoped, recently produced crystals, but they depend strongly on the level of doping and the manifacturer.

To customize the radiation hardness study to our case, we exposed four samples of BGO crystals to γ-rays from a high-activity ^{60}Co radioactive source. Two crystals of 2.2x2.2x18 cm^3 have been previously used in the L3 experiment at CERN, other two crystals of 2.5x2.5x20 cm^3 were recently supplied by the Shanghai Institute of Ceramics (SIC).

Irradiations and measurements took place at the Calliope Gamma Irradiation Facility at ENEA-Casaccia center (Rome). The irradiation source is a cylindrical array of ^{60}Co source rods emitting γ-rays of 1.1 and 1.3 MeV, in an irradiation cell of 6x7x3.9 m^3 plus an attached gangway. Depending on the placement of the samples, dose rates from few rad/h up to 230 krad/h are available. The source can be moved outside or inside its shielding pool in less than two minutes.

Plastic mechanical supports for the crystals, not shielding them from the radiation, allowed us to expose the samples to different dose rates, and to couple them to EMI 9814B Photomultiplier Tubes (PMT) to perform the LY measurements using a low-activity ^{60}Co calibration

source. PMTs were read out by a CAEN VME ADC.

We started our irradiation campaign by exposing the crystals to 5-10 rad/h dose rate for few hours. We were able to measure the LY once every 20 minutes of irradiation, with only two minutes delay after the source was shut down. Using this approach we measured the progressive LY reduction at different dose rates. We measured the LY recovery after 15-30 rad and 170 rad doses, and evaluated the recovery time constant for the different samples by fitting the time evolution of the LY after irradiation with the sum of two exponential functions. The results summarized in Tab. 9.5 show that the LY loss are important and that there are several components in the recovery time. The most relevant one, due to 5-10 rad/h dose rate are about four hours.

dose (rad)	rate (rad/h)	*LY drop*	τ_1 hr	τ_2 hr
15	5	25%	2.7 ± 0.4	–
170	10	67%	4.7 ± 0.2	380 (fixed)
12×10^6	23×10^4	90%	5.0 ± 2.4	381.9 ± 3.5

Table 9.5: Effect of irradiations on a BGO crystal: relative LY loss after irradiation and recovery times as measured with a fit to the time evolution with two exponential components.

We then exposed some crystals to a massive dose rate of 230 krad/h for a total dose of 12 Mrad, and then to small doses with 1.5 rad/h rate, to measure the sensitivity to small dose rates after strong delivered doses. We measured LY reductions up to 1/10 of the pre-irradiation LY value. A long-term recovery was then analyzed and exploited to measure the recovery time constant. We fit the LY recovery data with a double-exponential function, yielding a short time constant of (5.0±2.4) h and a long time constant of (381.9±3.5) h . BGO crystals from L3 experiment showed a larger damage after each irradiation, but also a faster recover capability, while crystals from SIC hardly recovered from radiation damage.

Light transmission spectra have been acquired before and after irradiations, in order to identify the nature of the LY reduction. As previously stated, the radiation-induced LY reduction could be due either to a decrease of the light transmittance, or to a damage of the scintillation mechanism itself. By comparing the LY and transmittance measurements, we observed that the main effect of the radiation damage was a reduction of the light transmission due to color-centre formation.

9.3.6.4 Comparison among options

The decision on the technology to be used for the forward calorimeter must be based on a compromise between physics performances and building costs. The options considered are the use of LYSO, pure CsI, or BGO crystals, as described in the previous subsections of this section, and the use of lead tungstate (PWO) crystals, for which the study was based on information known in literature.Such alternatives were compared with the one chosen as baseline for this study and described in the rest of the chapter, a Csi(Tl) and LYSO hybrid.

In order to compare the **physics performances** of the possible alternatives a full GEANT4 simulation was set up. It included: the correct detector geometry; the electronic noise obtained from beam- or lab- tests when available and extrapolations from them when needed; signal shape obtained from detailed simulation of the expected electronic chain; signal extraction algorithm reproducing the actual electronics; clustering algorithm based on the BaBar one.

For each option and for several energies the response of the detector to monochromatic photons is fitted with a gaussian with exponential tails. The relative energy resolutions is computed as the FWHM of the fitted shape for several values of the photon energy. The comparison among the results for the different options is reported in Fig. 9.46 separately for the current estimate of the machine background and a con-

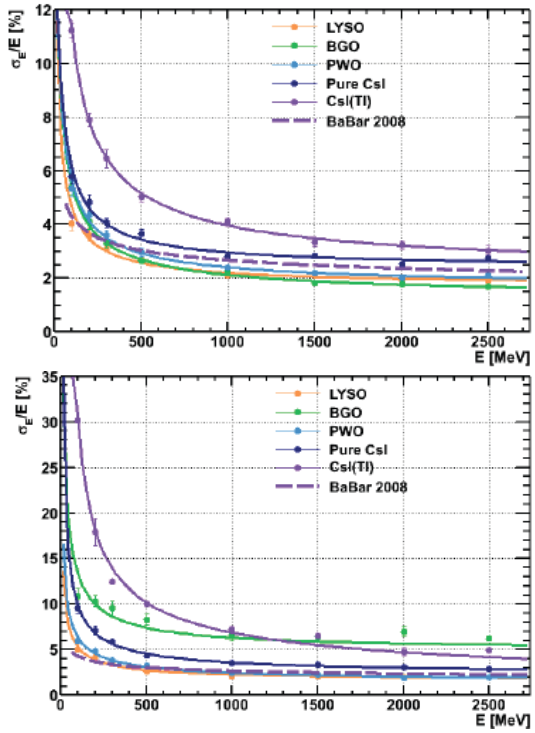

Figure 9.46: Comparison of the relative energy resolution between several options of the forward EMC. Left: nominal machine background. Right: machine background inflated by a safety factor of five. **NEED TO REDO PLOT WITH: COMPLETE HYBRID AND LATEST BACKGROUND. ALSO ADD BARREL ON TOP**

servative scenario where this background is increased by a safety factor five (5x-background).

The best option is clearly to use only LYSO crystals, while the option suffering for the most problems is the one with BGO. The latter is indeed very sensitive to the 5x-background most likely due to the non-optimal geometry of the simulation, which was not done ad-hoc. Also, the hybrid solution suffers from background, but all effects are comparable with the expected degradation in resolution of the barrel. All other options have comparable performances, intermediate between the full LYSO and the hybrid options.

To complete the picture, Tab. 9.6 shows a comparison of the **volume and total cost** of the scintillating crystals required for the forward endcap in different configurations. To compare options on the same basis, the costs need to include, besides the cost of the crystals, also the cost of the photodetectors, of the calibration system, and of the mounting structure.

Photo-detectors have reasonably similar costs for all options. Some saving can be achieved with the hybrid option by reusing existing channels. A more accurate calibration system is instead needed only for the options that degrade under irradiation with a short recovery time, namely BGO and PWO. Finally, the carbon fiber mechanical support needs to be redone only for the LYSO, BGO and PWO options, while in the other options the only costs are the shipping and the refurbishment of the present structure.

The table also lists three hybrid options, in which a number of the outer CsI(Tl) rings of the endcap are retained (since they are approximately at the same distance from the interaction region as are the forward barrel crystals) and the inner rings are replaced by LYSO crystals.

The two least expensive options are the hybrid and the CsI solutions. Among this the performance studies show that the hybrid option has a worse resolution. Nonetheless the properties of the CsI crystals are still under study and therefore the TDR budget was based on the more studied, albeit less performant, hybrid option.

9.4 Backward Calorimeter

The backward electromagnetic calorimeter for Super$B$ is a new device with the principal intent of improving hermeticity of the detector at modest cost. Excellent energy resolution is not a requirement, since there is significant material from the drift chamber in front of it. Thus, a high-quality crystal calorimeter is not planned for the backward region. The proposed device is based on a multi-layer lead-scintillator sampling calorimeter with longitudinal segmentation providing capability for π/e and K/π separation at low momenta. The design is derived from the analog hadron calorimeter for the ILC [32].

The active region of the backward calorimeter is located behind the drift chamber starting at $z = -1320\,\mathrm{mm}$ (see Figure 9.47) allowing room for the drift chamber front end electronics. The inner radius is 310 mm, the outer radius is 750 mm and its total thickness is less than 180 mm covering $12X_0$. It is constructed from a sandwich of 2.8 mm Pb plates alternating with 3 mm plastic scintillator strips (*e.g.*, BC-404 or BC-408). The scintillation light of each strip is collected by a wavelength-shifting fiber (WLS) coupled to a photodetector located at the outer radius. The scintillator strips come in three different geometries, right-handed logarithmic spirals, left-handed logarithmic spirals and radial wedges. This pattern alternates eight times. Each layer contains 48 strips producing a total of 1152 readout channels. The strip geometry is illustrated in Fig. 9.48

The WLS fibers, Y11 fibers from Kuraray, are embedded in grooves milled into the center of the scintillator strips. Each fiber is read out at the outer radius with a $1 \times 1\,\mathrm{mm}^2$ multi-pixel photon counter (SiPM/MPPC) [38]. A mirror is glued to each fiber at the inner radius to maximize light collection. The SPIROC (SiPM Integrated Read-Out Chip) integrated circuit (IC) [39] developed for the ILC is used to amplify and digitize the SiPM/MPPC sig-

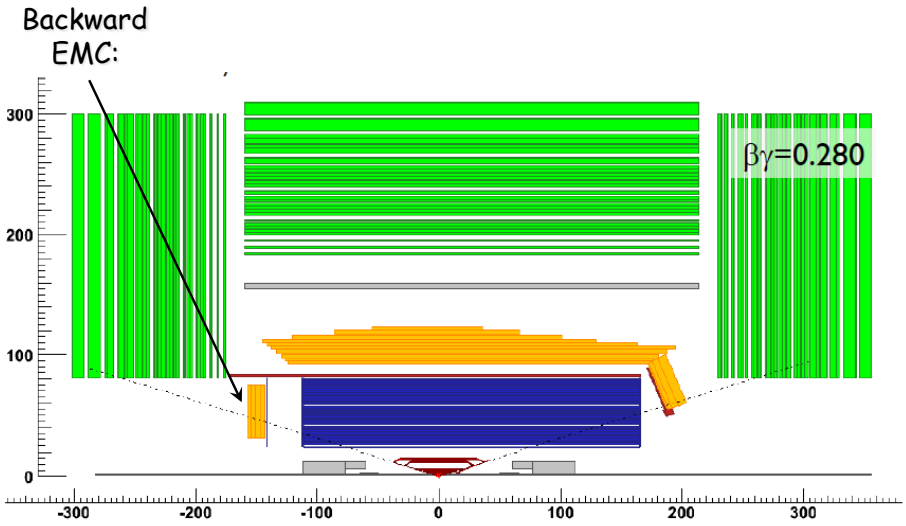

Figure 9.47: Layout of the calorimeters in the SuperB detector.

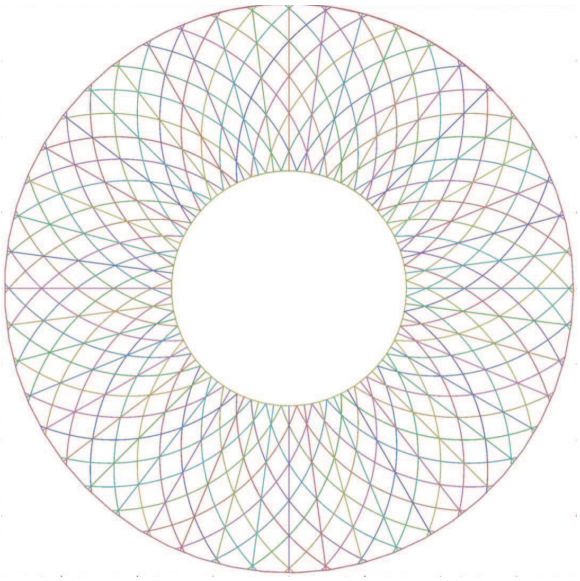

Figure 9.48: The backward EMC, showing the scintillator strip geometry for pattern recognition.

nals, providing both TDC (100 ps) and ADC (12 bit) capability. Each ASIC contains 36 channels. Since these ASICs were developed for SiPM readout, where the intrinsic gain is much higher, an additional preamplifier is coupled to the SiPM/MPPCs. This has the advantage to place the SPIROC ASICs at a convenient place in the detector without introducing additional noise.

9.4.1 Requirements

The main goal of the backward EMC is to increase the calorimeter coverage by recording any charged or neutral particle in the backward region. This information is important in particular for analyses that utilize the recoil method with hadronic and semileptonic tags to select B meson decays with neutrinos in the final state. The backward EMC helps to increase the selection efficiency and to improve background rejection. For this task, excellent energy resolution is not necessary. It is more important to keep the costs moderate. With moderate energy resolution and good angular resolution π^0 reconstruction is anticipated. Furthermore, the backward EMC has the capability to measure time-of-flight and the energy loss via ionization of charged particle well. This information is very useful for particle identification, in particular π/e and K/π separation at low momenta.

9.4.1.1 Energy and angular resolution

Since the backward EMC prototype is still in the construction phase, presently no results on

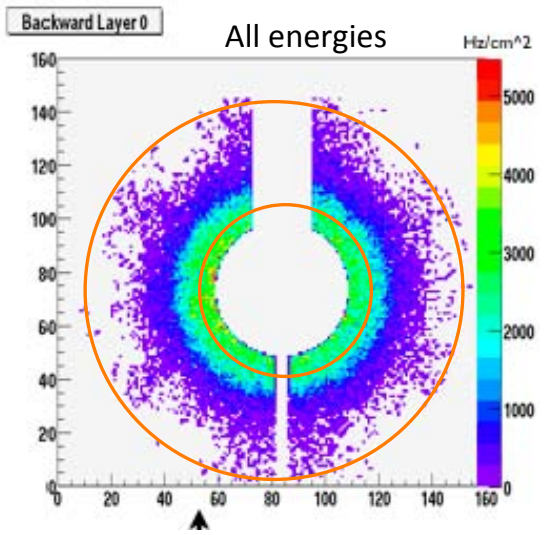

Figure 9.49: The distribution of background hits of all energies in the backward layer 0. The coverage by the backward EMC is shown by the red circles.

energy resolution and angular resolution exist. However, electromagnetic sampling calorimeter prototypes with plastic scintillator strips and tiles have been tested in test beams within the CALICE collaboration [40]. The energy resolution for the stochastic term is $15\%\sqrt{E[\,\mathrm{GeV}]}$ and for the constant term is around 1%. For the CALICE analog hadron calorimeter which has a non-optimized geometry for electromagnetic showers, the stochastic term was measured to be around $20\%/\sqrt{E[\,\mathrm{GeV}]}$. For low photon energies, an additional noise term of $\sim 130\,\mathrm{MeV}/E$ contributes. Thus, the backward endcap EMC is expected to have a similar performance with a stochastic term of $15-20\%/\sqrt{E[\,\mathrm{GeV}]}$.

The left-handed logarithmic spirals are defined by

$$x(t) = r\exp b\cdot t\cos t - r \tag{9.7}$$
$$y(t) = r\exp b\cdot t\sin t \tag{9.8}$$
$$\tag{9.9}$$

For $r = r_o/2 = 37.5$ cm and $b = 0.2$ eight left-handed spiral strips overlap with eight right-handed spiral strips defining a specific tile-shaped region. The radial strips overlap with five left-handed (right-handed) spiral strips. In the worst case, the resolution is $\sigma_r = \sigma_\phi \simeq 29\,\mathrm{mm}$ for a single tile in the outer region. This is improved to $\sigma_r = \sigma_\phi \simeq 12\,\mathrm{mm}$ in the inner region. If the shower is distributed over several adjacent tiles, its position can be determined by the center-of-gravity method improving the position resolution significantly.

9.4.1.2 Background rates

Present background simulations indicate that the worst neutron rate in layer zero of the backward IFR end cap is 3.5 $\mathrm{kHz}/\,\mathrm{cm}^{-2}\mathrm{s}^{-1}$. The radiation profile shown in Figure 9.49 indicates that the worst rates for all energies of 3 $\mathrm{kHz}/\,\mathrm{cm}^{-2}\mathrm{s}^{-1}$ occur in the inner most region. In ten years of running this amounts to $6.1\times10^9\ n/\,\mathrm{mm}^2$ in the region near the inner radius. The background rates drop significantly towards outer radius. At the location of the photodetector, the rate is reduced by more than a factor of 10. Further simulation studies are needed, since due to the high rate at the inner radius an occupation problem may be present. To deal with this issue one either subtracts a higher average background energy from each strip or divides the strips into two segments at the cost of doubling the number of photodetectors. The former solution will have an effect on the energy resolution since the background energy deposit has a wide distribution. The latter solution is preferable, but is about \$100k more expensive.

9.4.1.3 Radiation hardness

Irradiation of Si detectors causes the dark current to increase linearly with flux Φ:

$$\Delta I = \alpha\Phi V_{\mathrm{eff}} G, \tag{9.10}$$

where $\alpha = 6\times10^{-17}$ A/ cm $V_{eff}\sim 0.004\,\mathrm{mm}^3$, Φ is the flux, V_{eff} is the bias voltage and G is the gain. Since the initial resolution of MPPCs/SiPMs of $\sim$ 0.15 photoelectrons (pe) is much better than that of other Si detectors, radiation effects start at lower fluxes. For example, at a flux $\Phi = 10^{10}\ n/\,\mathrm{cm}^{-2}\mathrm{s}^{-1}$ the individ-

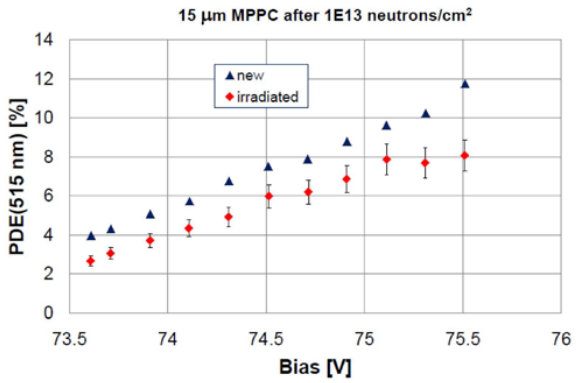

Figure 9.50: The efficiency of $15\,\mu\text{m} \times 15\,\mu\text{m}$ pixel MPPCs as a function of the bias voltage before and after irradiation with $10^{13} n/\,\text{cm}^{-2}\text{s}^{-1}$.

ual single pe signals are smeared out. The MIP peak is still visible at $\Phi \sim 10^{11}\ n/\,\text{cm}^{-2}\text{s}^{-1}$. The number of observed hot spots and the noise rate increases after irradiation of $3 \times 10^9\ n/\,\text{cm}^{-2}\text{s}^{-1}$. No significant changes are observed on the cross talk probability as well as no significant change on the saturation curves. The main effect is an increase in noise after exposure to high n dose. Hamamatsu has produced new SiPM/MPPCs with $20\,\mu\text{m} \times 20\,\mu\text{m}$ and $15\,\mu\text{m} \times 15\,\mu\text{m}$, which have lower detection efficiency than the $25\,\mu\text{m} \times 25\,\mu\text{m}$ version due to more boundaries and thus need a higher bias voltage to compensate for losses. Figure 9.50 shows the detection efficiency as a function of bias voltage for $15\,\mu\text{m} \times 15\,\mu\text{m}$ detectors before and after irradiation with $10^{13}\ n/\,\text{cm}^{-2}\text{s}^{-1}$. For the new detectors, signal/noise and the equivalent noise charge look fine after irradiation. We expect the backward endcap EMC will record $10^{11}\ n/\,\text{cm}^{-2}\text{s}^{-1}$ after 10 years operation. If the $25\,\mu\text{m} \times 25\,\mu\text{m}$ pixel SiPM/MPPC show a problem we may switch to one of the new SiPM/MPPCs with smaller pixel size.

9.4.1.4 Solid angle, transition to barrel

In the laboratory frame, the backward EMC covers a full polar angle region from 231 mrad to 473 mrad. Partial coverage extends the polar angle region from 209 mrad to 517 mrad. In the present design, there is a gap between the backward EMC and the barrel covering the region 517 mrad to 694 mrad in the laboratory frame. In the center-of mass frame, full coverage of the backward EMC is in the region 215 mrad to 442 mrad, while partial coverage exists in the region from 194 mrad to 482 mrad. If the backward EMC could move closer to the IR, the gap to the barrel calorimeter could be reduced.

9.4.2 Mechanical design

The 3 mm thick scintillator strips are cut individually from a scintillator plate. Thus, the plate size and the cutting procedure need to be carefully thought through to minimize the amount of waste. For the spiral strips the least waste and fastest production is obtained by fabricating a mould. However, this approach may be too expensive, since the total number of spiral strips is rather small. The preferred scintillator material is BC 404 from St Gobain, since it has the smallest decay time for TOF capability and its emission spectrum is reasonably matched to the Y11 absorption spectrum. The strip width is 38 mm at the inner edge increasing to 98 mm at the outer edge. The strip sides are painted with a white diffuse reflector. Front and back faces are covered with reflectors sheets (3M, Tyvec). Test bench measurements have shown that the yield along the strips varies by more than a factor of two. To restore uniformity, a pattern of black dots is printed onto the white reflector sheets.

In the center of each strip, a 1.1 mm deep groove is milled into which the 1 mm thick Y11 WLS fiber is inserted. At the outer edge of the strip, the groove is cut 0.4 mm deeper so that the active area of the SiPM/MPPC fully covers the fiber. The SiPM/MPPC is housed in a small precisely cut pocket. Especially fabricated fixtures out of Teflon or Nylon will hold a strip. The fiber groove at the outer edge is closed with a plug at the position of the photodetector. The Y11 fiber is pressed against the plug and held with a drop of glue. After removing the plug the SiPM/MPPC is inserted and is glued onto the Y11 fiber to match refractive in-

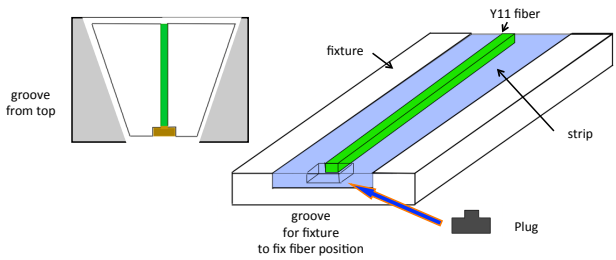

Figure 9.51: Schematic of holding the scintillator strip in a fixture for mounting the MPPC to the Y11 fiber.

dices. A mirror is placed at the other end of the fiber to detect the light that moves away from the photodetector. So tolerances in the length of the Y11 fiber are picked up at the mirror end. The strip layout is shown in 9.51.

To hold the strips in each layer in place 1.5 mm deep and 1 mm wide grooves are cut into the lead plates. The shape of groove matches that of the strip. A 3 mm thick and 1 m wide and 550 mm long plastic strip is inserted into the groove and is glued. This structure is strong enough to hold the scintillator strips in place. The calorimeter can be rotated by 90°. This is needed for operation with cosmic muons that yield a MIP calibration and allows for testing the calorimeter before installing it into the SuperB detector.

The entire calorimeter just weighs about 1300 Kg. An Al frame with a strong rear plate and a strong inner cylinder will hold the backward EMC in the SuperB detector. The front plate and outer cylinder needed for closure and shielding can be thin. Concerning cost and performance it is advantageous to build the backward EMC as a single unit. This requires the calorimeter to slide back on the beam pipe supported on the tunnel walls. It needs to be fixed at the tunnel and is rolled in. Since the inner radius is 31 cm, there is sufficient clearance for pumps and other beam elements. The design of this capability requires a detailed drawing of the beam pipe and the position and size of machine elements.

It is possible, however, to build the backward EMC in two halves with a vertical split. The impact of such a design is that ten strips per layer have to be cut into two segments. The inner segments of these strips have to be read out at the inner radius. This increases the number of channels by 240, requiring 240 additional SiPM/MPPCs, seven extra SPIROC boards and four extra calibration boards. This layout will deteriorate the performance near the vertical boundary. The effect needs to be studied in simulations. This adds extra costs at the order of $\sim 20\%$.

9.4.2.1 Calorimeter construction

Each completed strip with Y11 fiber and MPPC mounted is tested in the lab with a ^{106}Ru source. All important properties, such as bias voltage, gain, noise, and MIP position are recorded in a data base. Stacking will start from the rear to the front. The rear Al plate rotated by 90° is placed on the mounting table and the inner cylinder is bolted on to it. The back plate requires 48 radially milled grooves into which the plastic strips are inserted that will hold the scintillator strips. Next, all scintillator strips are mounted, the MPPCs are connected to preamplifiers and a Pb plate with right-handed logarithmic spiral grooves is placed on top completing layer 24. This procedure is repeated 24 times. Finally, another scintillator layer with radial strips and the front plate are stacked. The scintillator layer 0 yields information on the shower origin.

Before the outer cylinder is bolted on, temperature sensors and clear fibers need to be installed at the outer ring that transport light from a UV LED to the strips. If each fiber illuminates 13 strips via a notch spaced equidistantly every 12 mm, a total 96 fibers are sufficient. The fibers run through small holes in the back plate from the rear to the front. Attaching four fibers per LED, 24 LEDs housed outside the rear plate are needed.

9.4.2.2 Support and services

The preferred option is to build the backward EMC as one unit. In order to avoid breaking the beam pipe when access is required to the drift

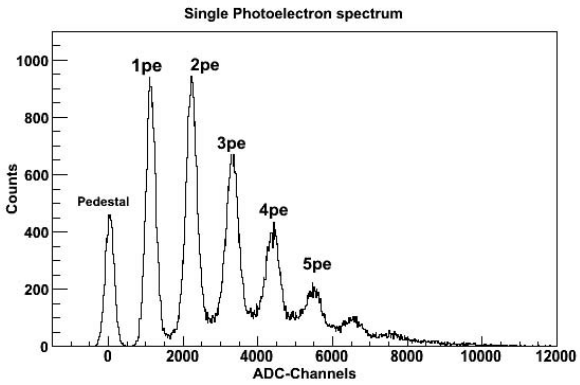

Figure 9.52: Single photoelectron spectrum measured with a Hamamatsu S10362-11-025P MPPC.

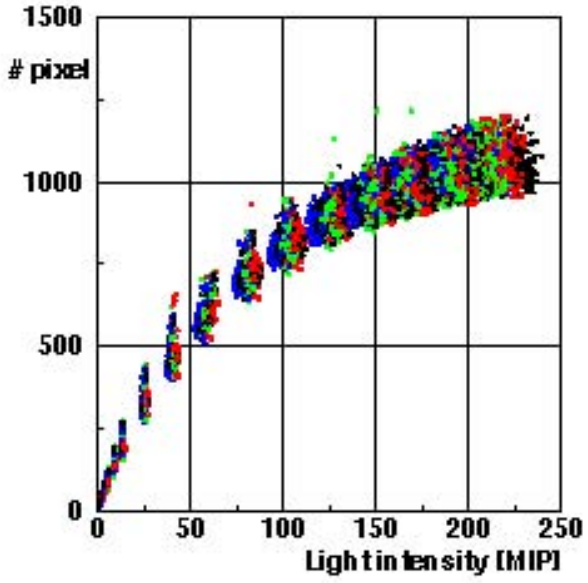

Figure 9.53: Saturation curves of 10,000 SiPMs measured in the CALICE analog hadron calorimeter.

chamber endplate, the backward EMC must be be able to slide back far enough. The explicit design requires a detailed design of the IR with all machine elements in place. In the detector position, the weight is supported by two brackets that are fixed at the rear endplate and on the inner wall of the IFR backward endcap. When rolling back the weight could be supported by the tunnel wall. To allow for a smooth sliding back, rolls are mounted on the inner support cylinder.

The 32 SPIROC ASICS and four calibration boards are mounted on the rear support plate of the EMC. Each SPIROC ASIC has one multiplexed USB output cable to the DAQ, a cable providing low voltage input for +5.5 V and -7.5 V, a cable for the MPPC bias voltage of 70 V, an electronic calibration input and an analog output. Since the 36 signal cables remain inside the detector, a total 192 cables have to be supplied from the outside to the SPIROC ASICs.

The four CMBs are also mounted on the rear support plate. Each CMB holds six LEDs and six PIN photodiodes and need to read out four thermocouples. Including the low voltage supplies for the CMB electronics, 80 cables are needed for the CMBs, yielding 272 cables in total.

9.4.3 SiPM/MPPC readout

The photodetectors are SiPM/MPPCs from Hamamatsu (type S10362-11-025P) with a sensitive area of 1 mm × 1 mm holding 1600 pixels with a size of 25 μm × 25 μm. These detectors are avalanche photodiodes operated in the Geiger mode with a bias voltage slightly above the breakdown corresponding to $50-70$ V providing a gain of a few 10^5. They are insensitive to magnetic fields. Each pixel typically has a quenching resistor of a few MΩ so they recover within 100 ns. The efficiency is of the order of $10-15\%$. Since the SiPM/MPPCs record single photoelectrons as shown in Fig. 9.52 for a Hamamatsu MPPC, they are auto-calibrating. SiPM/MPPCs are non-linear requiring non-linearity corrections for higher energies. As an example, Fig. 9.53 shows the response curves of 10,000 SiPMs measured at ITEP most of which were installed in the analog hadron calorimeter [32]. The dynamic range is determined by the number of pixels. Properties of several SiPM/MPPCs are listed in Table 9.7.

A concern with SiPM/MPPCs is radiation hardness. Degradation in performance is observed in studies performed for the Super$B$ IFR, beginning at integrated doses of order 10^8 1-MeV-equivalent neutrons/ cm^2 [41]. This needs to be studied further, and possibly mitigated with shielding. Another alternative is to look into a different photodetector. Recently, Hamamatsu has produced SiPM/MPPCs with pixel sizes of 20 μm $\times$ 20 μm and 15 μm $\times$ 15 μm (see Table 9.7). A CMS study shows that the performance of these new photodetectors deteriorates only slightly after an irradiation of $10^{13} n/\,\mathrm{cm}^{-2}\mathrm{s}^{-1}$.

9.4.4 Electronics

The signal of the SiPM/MPPC is first amplified with a charge-sensitive preamplifier then fed into the auto-triggered, bi-gain SPIROC ASIC. The SPIROC board has 36 channels. Each channel has a variable-gain charge preamplifier, variable shaper and a 12-bit Wilkinson ADC. It allows to measure the charge Q from one photoelectron (pe) to 2000 pe and the time t with a 100 ps accurate TDC. A high-level state machine is integrated to manage all these tasks automatically and control the data transfer to the DAQ. The SPIROC ASIC was designed to supply the high voltage for the SiPM/MPPC. Using a DAC, individual high voltages within ± 5 V can be supplied to each photodetector.

The SPIROC ASIC gives Gaussian signals with no tails, shows excellent linearity and low noise. 32 ASIC readout boards are needed to read out the entire endcap. The boards are mounted in two layers behind the endcap. The first layer holds 20 boards and the second layer the remaining 12 boards. Each board connects to 36 SiPM/MPPCs via a ribbon cable that were designed for ILC at a luminosity of $\mathcal{L} = 10^{34}$ cm^{-2}s^{-1}.

9.4.5 Calibration

An LED-based calibration system with fixed LED intensities is used to monitor the stability of strip-fiber-SiPM/MPPC system between MIP calibrations, to perform gain calibrations, determine intercalibration constants, and to measure the SiPM/MPPC response functions. This is necessary since the SiPM/MPPCs have a temperature and voltage dependence of the gain of

$$\frac{dG}{dT} \sim -1.7\%/\mathrm{K}, \tag{9.11}$$

$$\frac{dG}{dV} \sim 2.5\%/0.1\ \mathrm{V}. \tag{9.12}$$

The temperature and voltage dependence of measuring the charge of the scintillation signal is

$$\frac{dQ}{dT} \sim -4.5\%/\mathrm{K} \tag{9.13}$$

$$\frac{dQ}{dV} \sim 7\%/0.1\ \mathrm{V} \tag{9.14}$$

The calibration system is based on a new design for the analog hadron calorimeter. Light from a UV LED is coupled to clear fibers. The fibers are notched at equidistant positions. The shape of each notch changes such that it emits about the same intensity of light. For the backward EMC, 96 fibers with 13 notches each are sufficient to illuminate all strips. If four fibers are coupled to one LED, 24 LEDs are needed whose light is monitored by a PIN photodiode. A few thermocouples distributed throughout the outer edge of the EMC near MPPCs measure temperature. Both temperature and bias voltage are recorded regularly by a slow control system. After temperature and PIN diode correction the stability of LED system is better than 1%.

The calibration boards are 40 mm$\times$140 mm in dimension and house one LED, one PIN diode, the electronics to read out the PIN diode, and monitor temperature and MPPC voltage. The boards are sufficiently small to be mounted at the backplate near the outer radius. They can be arranged such that the fibers can be nearly straight.

9.4.6 Backward simulation

A simple backward EMC model exists in the GEANT4 simulation that models 24 layers of scintillator and lead. Each layer is modeled by

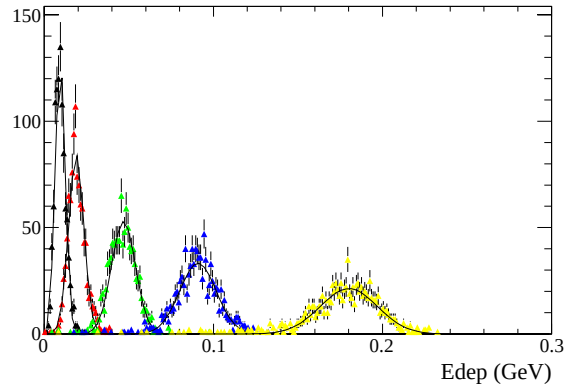

Figure 9.54: Energy depositions from mono-energetic photons (0.1 GeV, 0.2 GeV, 0.5 GeV, 1 GeV and 2 GeV) observed in the scintillators of the backward EMC.

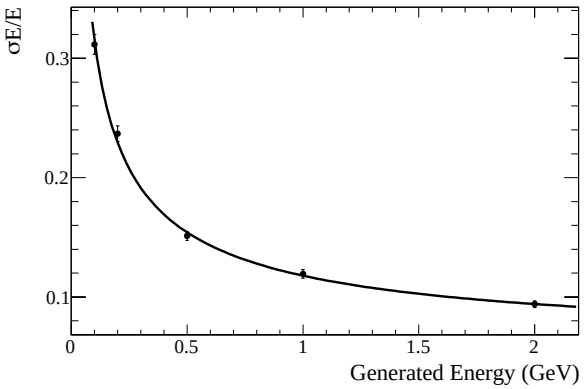

Figure 9.55: The backward EMC energy resolutions, σ_E/E, where σ_E and E are the Gaussian width and mean in Fig. 9.54, as a function of generated photon energy.

a complete disc without physical strip segmentations in r-ϕ. Support structure, fibers, electronics, and cables are presently ignored.

In the fast simulation, the model does not separate lead from scintillator. It uses instead an artificial material that approximates the overall density, radiation length, interaction length and Molière radius of the mixture of lead and plastic. The volume is divided into eight rings, each of which is divided into 60 segments. The logarithmic spirals and the lead-scintillator layers, however, are not modeled explicitly to avoid a complicated shower reconstruction and the modeling of longitudinal shower energy distribution. The energy resolution is set to $\sigma_E/E = \frac{14\%}{\sqrt{E(\text{GeV})}} \oplus 3\%$.

9.4.7 Performance in simulations

A GEANT4 simulation is performed to study the energy resolution under the simplified conditions, ignoring the rest of the detector and shooting mono-energetic photons perpendicular to the face of the disc. All energy deposited in the scintillator is collected. No clustering algorithm is performed. Figure 9.54 shows the energy deposition for five different photons energies, 0.1, GeV 0.2 GeV, 0.5 GeV, 1 GeV, and 2 GeV. For 0.1 GeV photons, approximately 9.5% of the photon energy is deposited in the scintillator on average. This percentage drops to 9.0% for 2 GeV photons.

The energy dependence of the energy resolutions on generated energy is shown in Fig. 9.55. The distribution can be fitted with the function $\sigma_E/E = \frac{10\%}{E(\text{GeV})^{0.485}} \oplus 6\%$.

9.4.8 Impact on physics results

Fast simulation studies have been conducted to investigate the performance gain achieved by the addition of the backward calorimeter. The channels chosen to evaluate the impact of this detector are $B \to \tau\nu$ and $B \to K^{(*)}\nu\bar{\nu}$, since both are benchmark channels for the Super$B$ physics program and the detector hermeticity improves signal reconstruction efficiencies and background rejection.

The study of the leptonic decay $B \to \tau\nu$ is of particular interest as a test of the Standard Model (SM) and a probe for New Physics [33]. The presence of a charged Higgs boson (in *e.g.*, a Two Higgs Doublet Model) as a decay mediator could significantly modify the branching ratio with respect to the SM value, depending on the Higgs mass and couplings. A detailed analysis of this channel is therefore quite important

in searches for physics beyond the SM. A complementary search for new physics can be performed using $B \to K^{(*)}\nu\bar{\nu}$ decays [34], [35]. Being mediated by a flavor-changing neutral current, these processes are prohibited at tree level in the SM and the higher order diagrams may receive contribution from a non-standard mechanism. Moreover, new sources of missing energy may replace the neutrinos in the final state.

The reconstruction of both decay modes is challenging, since the final state contains more than one neutrino and thus is only partially reconstructible. Signal events are selected using a recoil method analysis, in which the signal B-meson ($B_{\rm sig}$) is identified as the system recoiling against the other tag B meson ($B_{\rm reco}$). The tag B meson is either reconstructed fully via its hadronic decays or partially reconstructed from its semileptonic final states [36]. The rest of the event is assigned to the $B \to \tau\nu$ candidate, if it is compatible with one of the following decay modes of the tau lepton: $\mu\nu_\mu\nu_\tau$, $e\nu_e\nu_\tau$, $\pi\nu_\tau$, $\pi\pi^0\nu_\tau$, $\pi\pi^0\pi^0\nu_\tau$, $\pi\pi\pi\nu_\tau$, $\pi\pi\pi\pi^0\nu_\tau$. These final states cover about 95% of all τ decays, and have one charged particle (1-prong) or three charged particles (3-prong), with the possible addition of one or two π^0s. Since final states containing one or more π^0 cover about 40% of the tau decay modes, an increase in the EMC coverage improves substantially the efficiency of tau identification.

Candidates for the $B \to K^{(*)}\nu\bar{\nu}$ sample have to be compatible with one of the following final states: $K^{*+} \to K_S(\pi^+\pi^-)\pi^+$, $K^+\pi^0$, $K^{*0} \to K^+\pi^-$, K^+, $K_S \to \pi^+\pi^-$ (semileptonic analysis only). In the analyses with a $K^{(*)}$ in the final state, further selection criteria are applied using kinematic quantities related to the goodness of the $B_{\rm reco}$ and $K^{(*)}$ reconstruction and event shape variables that test the energy balancing in the event and the presence of missing energy due to the neutrinos in the final state. The present level of the analyses is very similar to that in Refs. [36] and [37].

Backgrounds are further rejected using, $E_{\rm extra}$, the total neutral energy in the calorimeter of particles not associated with either B-meson. Signal events peak at low values of $E_{\rm extra}$, while background events which contain additional sources of neutral showers tend to have higher values of $E_{\rm extra}$. The discriminating power of this observable obviously increases with the calorimeter coverage.

The performance of the backward EMC is assessed by comparing the signal-to-background ratio, S/B, and the statistical precision, $S/\sqrt{S+B}$, of the expected signal with and without the backward EMC used as a veto device for extra-neutral energy. For this task, the extra neutral energy reconstruction is split into two disjoint calorimeter regions: $E^{\rm extra}_{\rm brrfwd}$ covering the barrel and the forward region and $E^{\rm extra}_{\rm bwd}$ covering the backward region only. Furthermore, the effects of machine backgrounds (Sec. **??**) superimposed on physics events are taken into account.

The results for both rare decay channels are summarized in Table 9.8. For $B \to \tau\nu$ reconstructed in hadronic tags, the improvements in $S/\sqrt{S+B}$ are shown as a range sampling over the individual τ final states. For $B \to \tau\nu$ reconstructed in semileptonic tags, the improvement in $S/\sqrt{S+B}$ is presented as an average over all τ final states. Combining $S/\sqrt{S+B}$ of both tags, the net gain is of the order of 10%. For $B \to K^*\nu\bar{\nu}$, the net gain for hadronic and semileptonic tags combined ranges between 8% and 16% depending on the final state. For $B \to K\nu\bar{\nu}$ the net gain is about 6%.

These improvements in turn yield improvements in the precision of measured physical observables. For example, Figure 9.56 shows the expected precision of the measured $B \to K^+\nu\bar{\nu}$ and $B \to K^*\nu\bar{\nu}$ branching fractions as a function of integrated luminosity. The yellow band represents the SM prediction [33]. The red dots with red error bars are obtained from an extrapolation of *BABAR* measurements, taking into account the improvements due to the lower boost, corresponding to a higher detector hermeticity. Dots with black error bars are obtained from the same procedure but in addition include the backward EMC. For $\mathcal{B}(B \to K^+\nu\bar{\nu})$ and $\mathcal{B}(B \to K^*\nu\bar{\nu})$ the 3σ significance for evidence without the backward EMC is reached at 5 ab^{-1}

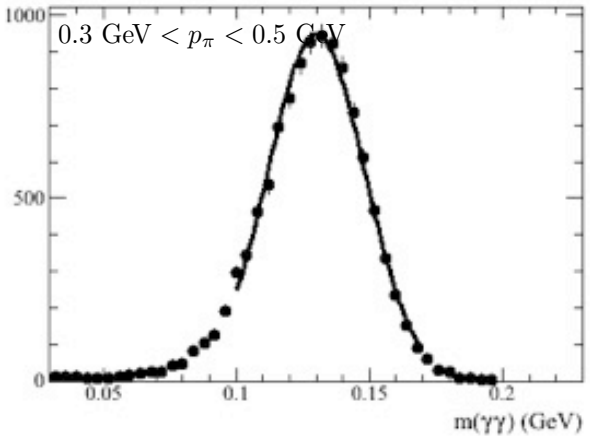

Figure 9.58: Invariant-mass resolution of $\pi^0 \to \gamma\gamma$, where one photon is detected in the backward EMC.

and 51 ab^{-1}, respectively. When adding the backward EMC, the 3 σ significance is already reached at 4.5 ab^{-1} and 42 ab^{-1}, respectively.

In addition to the measurement of neutral clusters, the backward EMC can be used to improve the π^0 reconstruction efficiency. If one photon is reconstructed in the backward EMC, the $\gamma\gamma$ invariant-mass resolution improves from $\sim$ 24 MeV for 200 MeV/c π^0s to $\sim$ 13 MeV for 1 GeV/c π^0s (see, e.g., Fig. 9.58).

It is worth mentioning that the inclusion of the backward EMC not only improves the background rejection, but also the B-tagging efficiency. The impact on the B reconstruction efficiency is determined by using the decays $B^- \to D^0\pi^-, D^0 \to K^-\pi^+\pi^0$. Events are separated into two groups: the first uses only photons from the barrel and forward endcap, while the second includes photons from the backward EMC with polar angle between $-0.96 < \cos\theta < -0.89$ as well. The π^0 mass window is defined as 120–145 MeV (100–180 MeV) for the first (second) group. For B candidates, D^0 s are selected by $1.830 < m_{K\pi\pi^0} < 1.880$ GeV and $-80 < \Delta E < 50$ GeV. The $m_{\rm ES}$ distribution is fitted to determine the B reconstruction efficiency. Including the backward EMC, the signal efficiency increases by nearly 4% in this particular channel (see Fig. 9.59).

9.4.9 Use for particle identification

Charged particles moving in the backward direction typically have lower momentum. Thus, ionization loss and time-of-flight measurements may provide useful information for particle identification, *e.g.* for e/π and K/π separation.

A preliminary time-of-flight study is performed with fast simulation. Single kaons or pions are generated that move towards the backward EMC. The true arrival time calculated at the first layer is smeared with a Gaussian resolution to simulate the measured time distribution. Velocity distributions are obtained for kaons and pions at a given momentum from the measured time and reconstructed track path length. Both mean and RMS values are extracted from these distributions to determine K/π separation in standard deviation units (σ) as a function of momentum for different time resolutions, in which uncertainties in the momentum measurement and path length reconstruction are included. Fig. 9.60 shows K/π separation in units of standard deviations as a function of momentum for time resolutions of 100 ps, 50 ps, 20 ps, 10 ps and perfect timing. For example for 100 ps time resolution, aK/π separation of more than three σ can be achieved for momenta up to 1 GeV/c and approximately 1.5σ up to 1.5 GeV/c.

Since each layer measures the time distribution, 24 measurements will be averaged. In addition to timing, the ionization is measured in each layer. For MIP-like particles, the average energy loss per layer is $dE_{Pb} = 4.3$ MeV and $dE_{\rm scintillator} = 0.6$ MeV. A 0.5 GeV/c π is at the ionization minimum, a 0.5 GeV/c K is below the minimum and a 0.5 GeV/c e is at the relativistic plateau. For MIP particles, the ionization loss in the 24 layers is $\Delta E = 117$ MeV. Since the energy loss below the minimum increases with decreasing momenta as $1/\beta^2$, dE/dx measurements in the endcap can be combined with the dE/dx information from the SVT and DCH. Figure 9.61 shows the ionization curves for e, μ, π, K and p as a function of momentum. A $> 3\sigma$ K/π separation is achievable for momenta up to $0.6 - 0.7$ GeV.

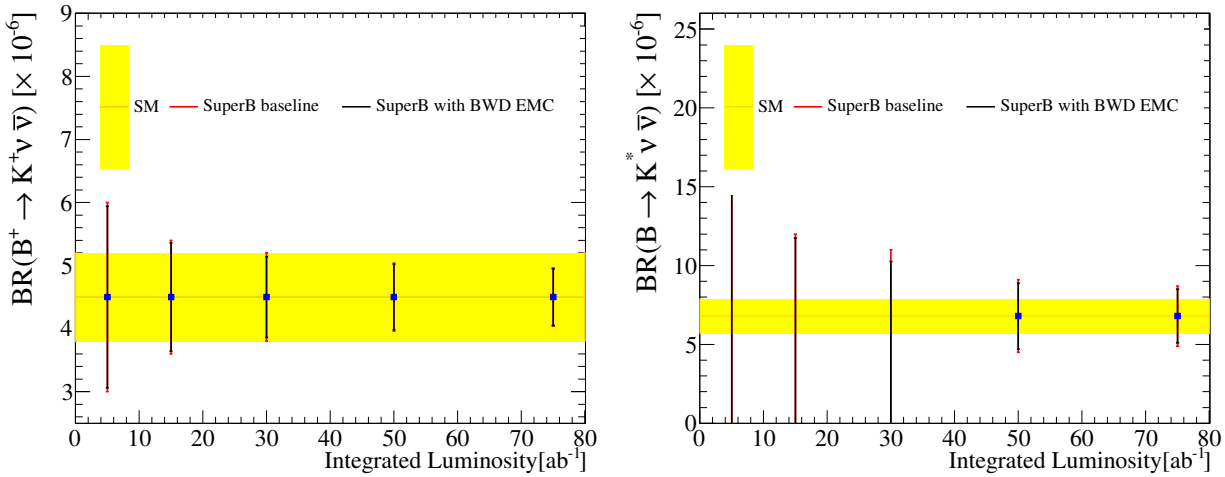

Figure 9.56: Expected precision on branching fraction measurements of (left) $\mathcal{B}(B \to K^+\nu\bar{\nu})$ and (right) $\mathcal{B}(B \to K^*\nu\bar{\nu})$ as a function of integrated luminosity. The yellow band represent the SM prediction, the black (red) error bars represent the upper limits or the branching fraction measurements with (without) the backward EMC.

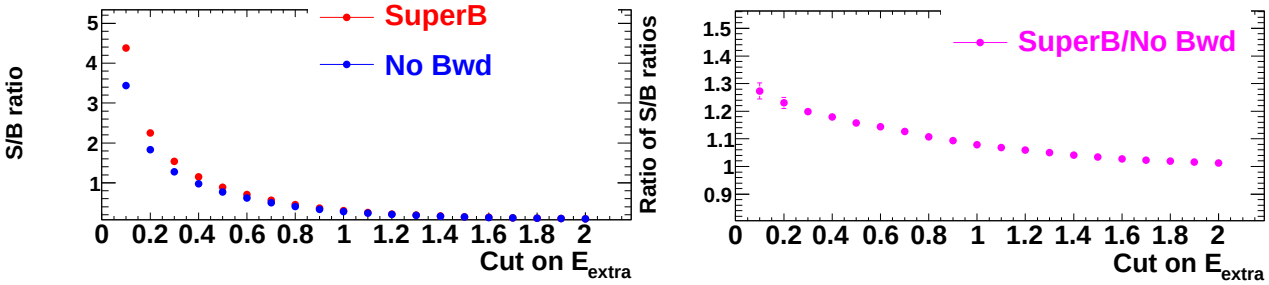

Figure 9.57: Left: Signal-to-background ratio with and without a backward EMC, as a function of the $E_{\rm extra}$ selection. Right: Ratio of the S/B ratio with a backward EMC to the S/B ratio without a backward calorimeter, as a function of the $E_{\rm extra}$ selection.

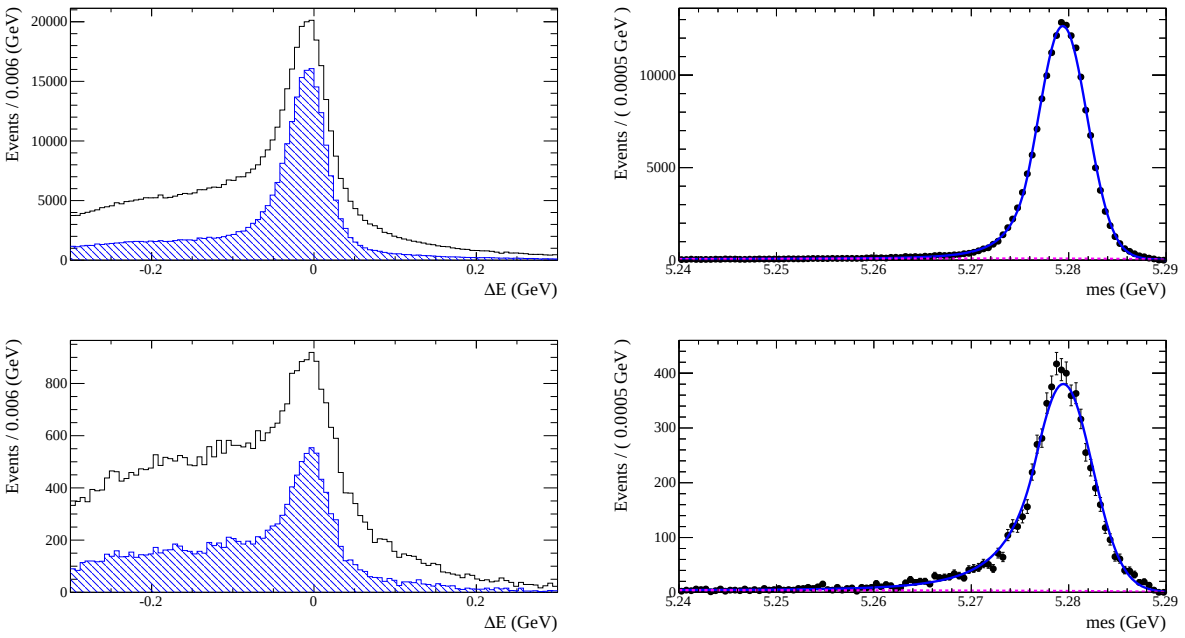

Figure 9.59: (left) ΔE and (right) $m_{\rm ES}$ distributions for the decay $B^- \to D^0\pi^-$ with $D^0 \to K^-\pi^+\pi^0$ reconstruction for (top) both γ's in barrel and forward endcap and (bottom) one γ in the backward EMC. The two histograms in each ΔE distribution are before and after a requirement on the D^0 mass.

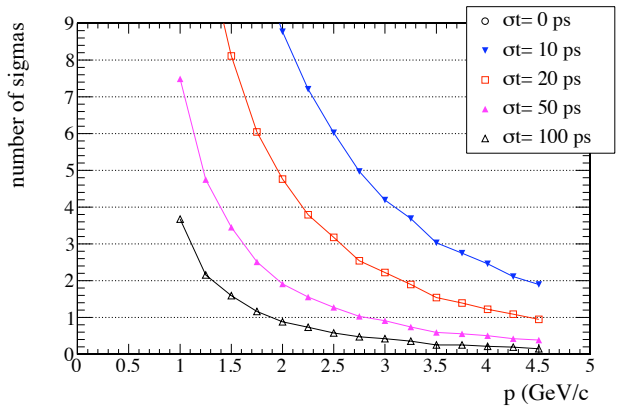

Figure 9.60: K/π separation versus measured momentum for different timing resolutions in the backward EMC. The finite separation for perfect timing is caused by uncertainties in the momentum measurement.

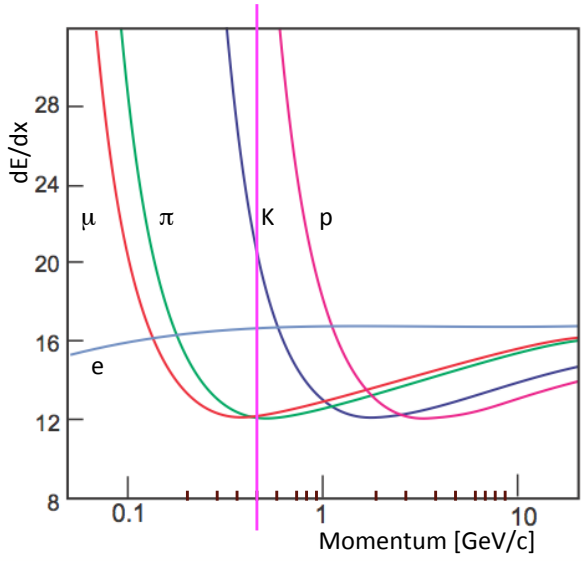

Figure 9.61: Calculated energy loss curves versus momentum for e, μ, π, K and p in one layer of the backward EMC.

9.4.10 Discussion of task force conclusions

In the process of deciding how to proceed with the backward EMC, a task force was convened to evaluate its various benefits and impacts. A number of conclusions came out of this:

- The device adds to the physics program in important channels through the increased hermeticity.
- The design is technically plausible and cost-effective, however: operation of the readout in the radiation environment should be studied further; a prototype should be demonstrated in a beam test.
- The possibility of using the backward EMC for PID through time-of-flight is attractive and should be pursued with further R&D.
- The capability to install this device should be preserved, as opposed to, for example, extending the drift chamber.

9.5 Trigger

This is a reminder that we need a synopsis of the EMC trigger somewhere in the EMC chapter, although the detailed description will be in the ETD chapter. It is to be determined whether this should be in a separate section or merged with the three sub-calorimeter sections.

9.5.1 Calorimeter readout trigger

9.5.1.1 Normal mode

9.5.1.2 Calibration mode

9.5.2 Calorimeter trigger primitives

9.6 Detector protection

Personnel ES&H will be elsewhere.

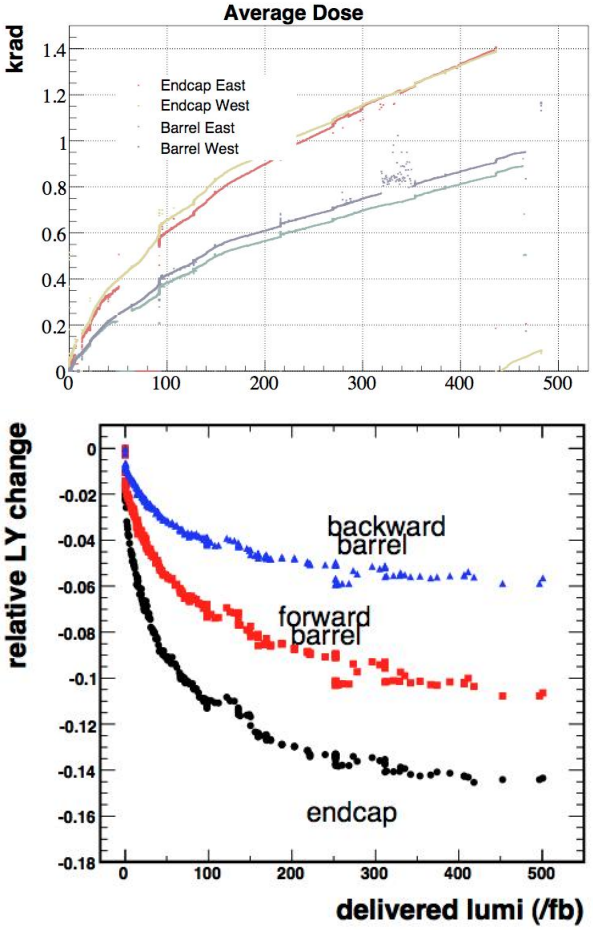

Figure 9.62: Left: Radiation dose as measured by RadFETs in the *BABAR* barrel and endcap. Right: Decrease in light output with radiation dose for the *BABAR* CsI(Tl) barrel and endcap.
These figures are placeholders; we need higher quality copies.

9.6.1 Thermal shock

9.6.2 Mechanical shock, including earthquakes

9.6.3 Fluid spills

9.6.4 Electrical surges, outages

9.6.5 Radiation damage

Radiation exposure from Bhabha, Touschek and beam-gas scattering is monitored by a set of 56 realtime integrating dosimeters (Rad-FETs) placed in front of the barrel and 60 RadFETs in front of the endcap. The accumulated dose, measured by these RadFETs over the life of the *BABAR* detector, along with the observed loss in scintillation light output is shown in Figure[**?**], separately for the endcap, the forward, and the backward barrel of the calorimeter. The dose over the life of Super*B* is expected to be two orders of magnitude greater.

9.7 Cost & Schedule

This will appear elsewhere.

9.7.1 WBS structure

9.7.2 Gantt chart

9.7.3 Basis of estimates

9.7.4 Cost and schedule risks

Table 9.3: Photo Luminescence Weighted Quantum Efficiencies (%)

Photo Luminescence	LSO/LYSO	BGO	CsI(Tl)
Hamamatsu R1306 PMT	12.9±0.6	8.0±0.4	5.0±0.3
Hamamatsu R2059 PMT	13.6±0.7	8.0±0.4	5.0±0.3
Photonis XP2254b	7.2±0.4	4.7±0.2	3.5±0.2
Hamamatsu S2744 PD	59±4	75±4	80±4
Hamamatsu S8664 APD	75±4	82±4	84±4

Table 9.6: Comparison of crystal volume and calorimeter costs for several forward endcap configuration options.

Option	Number of new crystals	New crystal volume (cm^3)	Crystal cost/cm^3 (k$)	Crystal cost (M$)	Photo-detectors (M$)	Calibration system (M$)	Total structure (M$)	cost (M$)
LYSO full (baseline)	4500	402	25.00	10.04	0.57	-	2.27	12.88
LYSO old structure	3600	402	25.00	10.04	0.57	-	0.25	10.86
Hybrid								
3 CsI(Tl) + 6 LYSO	2160	245	25.00	6.19	0.49	-	0.25	6.93
4 CsI(Tl) + 5 LYSO	1760	198	25.00	4.95	0.40	-	0.25	5.60
5 CsI(Tl) + 4 LYSO	1360	154	25.00	3.84	0.31	-	0.25	4.40
Pure CsI	900	692	5.09	3.52	0.56	-	0.25	4.33
BGO	4500	392	9.00	3.53	0.57	1.2-3.0	2.27	7.57-9.37
$PbWO_4$	4500	306	5.00	1.53	0.57	1.2-3.0	2.27	5.57-7.37

Table 9.7: Properties of Hamamatsu MPPCs

MPPC type	# cells $1/\,\mathrm{mm}^2$	C [pF]	R_{cell} kΩ]	C_{cell} [fF]	$\tau = R_c \times C_c$ [ns]	$V_{\mathrm{break\ down}}$ [V] at T=23 C	V_{op} [V] at T=23 C	Gain [10^5]
15 μm	4489	30	1690	6.75	11.4	72.75	76.4	2.0
20 μm	2500	31	305	12.4	3.8	73.05	75	2.0
25 μm	1600	32	301	20	6.0	72.95	74.75	2.75
50 μm	400	36	141	90	12.7	69.6	70.75	7.5

Table 9.8: Relative gain in $S/\sqrt{S+B}$ by including the backward EMC in the event selection for $B \to K^{(*)}\nu\bar{\nu}$ and $B \to \tau\nu$ decay channels reconstructed in the recoil of B semileptonic and hadronic tags. The first uncertainty is statistical and the second is systematic.

channel	Semileptonic	Hadronic
$B \to \tau\nu$	$(6.1 \pm 0.1 - 0.7)\%$	$\simeq 3 - 5\%$
$B \to K^+\nu\bar{\nu}$	$(5.8 \pm 1.0 - 0.6)\%$	-
$B \to K_S\nu\bar{\nu}$	$(6.0 \pm 0.4 - 0.6)\%$	-
$B \to K^{*+}(K^+\pi^0)\nu\bar{\nu}$	$(7.0 \pm 0.2 - 0.7)\%$	$(5.9 \pm 2.5 - 0.5)\%$
$B \to K^{*+}(K_S\pi^+)\nu\bar{\nu}$		$(6.2 \pm 2.1 - 0.5)\%$
$B \to K^{*0}\nu\bar{\nu}$	$(9.1 \pm 0.4 - 0.7)\%$	$(7.3 \pm 1.8 - 0.5)\%$

Bibliography

[1] P. D. Strother, "Design and application of the reconstruction software for the BaBar calorimeter," SLAC-R-828.

[2] J. M. Bauer [BaBar EMC Group Collaboration], "The BaBar electromagnetic calorimeter: Status and performance improvements," IEEE Nucl. Sci. Symp. Conf. Rec. **2** (2006) 1038.

[3] R. Y. Zhu, Nucl. Instrum. Meth. A **413**, 297 (1998).

[4] C. Melcher and J. Schweitzer, "Cerium-doped lutetium oxyorthosilicate: a fast, efficient new scintillator," *IEEE Trans. Nucl. Sci.* **39** (1992) 502–505.

[5] D.W. Cooke, K.J. McClellan, B.L. Bennett, J.M. Roper, M.T. Whittaker and R.E. Muenchausen, "Crystal Growth and Optical Characterization of Cerium-doped $Lu_{1.8}Y_{0.2}SiO_5$," *J. Appl. Phys.* **88** (2000) 7360–7362, and T. Kimble, M Chou and B.H.T. Chai, "Scintillation Properties of LYSO Crystals," in *Proc. IEEE Nuclear Science Symposium Conference* (2002).

[6] R.H. Mao, L.Y. Zhang and R.-Y. Zhu, "Optical and Scintillation Properties of Inorganic Scintillators in High Energy Physics," *IEEE Trans. Nucl. Sci.* **NS-55** (2008) 2425–2431.

[7] W. Wisniewski, "Consideration for Calorimetry at a Super B Factory", in *Proceedings of Tenth International Conference on Calorimetry in Particle Physics*, Ed. R.-Y. Zhu, World Scientific (2002), and C. Cecchi. "A LYSO Calorimeter for a SuperB Factory ," in *Proceedings of Fourteenth International Conference on Calorimetry in Particle Physics*, Journal of Physics Series (2010).

[8] F. Happacher, "CCALT: Crystal Calorimeter at KLOE2," in *Proceedings of Fourteenth International Conference on Calorimetry in Particle Physics*, Journal of Physics Series (2010).

[9] The Mu2e Experiment, see http://mu2e.fnal.gov/.

[10] R.-Y. Zhu, Talk given at the CMS Forward Calorimetry Task Force Meeting at CERN, June 17, 2010. See http://indico.cern.ch/getFile.py/access?sessionId=0&re
materialId=0&confId=97272

[11] D.A. Ma and R.-Y. Zhu, "Light Attenuation Length of Barium Fluoride Crystals," *Nucl. Instr. and Meth.* **A333** 422-424 (1993).

[12] R.H. Mao, L.Y. Zhang and R.Y. Zhu., "Emission Spectra of LSO and LYSO crystals Excited by UV Light, X-ray and γ-ray," *IEEE Trans. Nucl. Sci.* **55** (2008) 1759–1766.

[13] Rihua Mao, Liyuan Zhang and Ren-yuan Zhu, "Quality of a 28 cm long LYSO Crystal and Progress on Optical and Scintillation Properties," Paper N38-2 in *2010 IEEE NUCLEAR SCIENCE SYMPOSIUM CONFERENCE RECORD.*

[14] J.M. Chen, L.Y. Zhang and R.-Y. Zhu, "Large Size LSO and LYSO Crystal Scintillators for Future High Energy Physics Experiments," *IEEE Trans. Nucl. Sci.* **NS-54** (2007) 718–724 and *Nucl. Instr. and Meth.* **A572** (2007) 218–224.

[15] J.M. Chen, L.Y. Zhang and R.-Y. Zhu, "Large Size LYSO Crystals for Future High Energy Physics Experiments," *IEEE Trans. Nucl. Sci.* **NS-52** (2005) 3133–3140.

[16] R.-Y. Zhu, Invited talk given at the Time Resolution Workshop at University of Chicago, April 28, 2011. See http://www.hep.caltech.edu/∼zhu/talks/ryz_110428_time_resolution.pdf

[17] S.E. Derenzo, M.J. Weber, W. W. Moses, and C. DuJardin, "Measurements of the Intrinsic Rise Times of Common Inorganic Scintillators," *IEEE Trans. Nucl. Sci.* **47** (2000) 860–864.

[18] T. Szczesniak, M. Moszynski, A. Synfeld-Kazuch, L. Swiderski, M.A.S. Koschan and C.L. Melcher, "Time resolution and decay time of LSO Crystals Co-Doped with Calcium," *IEEE Trans. Nucl. Sci.* **57** (2010) 1329–1334.

[19] Ren-yuan Zhu, "Radiation Damage in Scintillating Crystals," *Nucl. Instr. and Meth.* **A413** (1998) 297–311.

[20] *The CMS Electromagnetic Calorimeter Project*, CERN/LHCC 97-33 (1997).

[21] Rihua Mao, Liyuan Zhang and Ren-yuan Zhu, "Optimization of Light Response Uniformity for SuperB Tapered LYSO Crystals with APD Readout," Paper N29-6 in *2011 IEEE NUCLEAR SCIENCE SYMPOSIUM CONFERENCE RECORD*.

[22] J.M. Chen, R.H. Mao, L.Y. Zhang and R.Y. Zhu, "Gamma-ray induced radiation damage in large size LSO and LYSO crystal samples," *IEEE Trans. Nucl. Sci.,* **54** (2007) 1319–1326.

[23] Rihua Mao, Liyuan Zhang and Ren-yuan Zhu, "Gamma-ray induced radiation damage in PWO and LSO/LYSO crystals," *2009 IEEE NUCLEAR SCIENCE SYMPOSIUM CONFERENCE RECORD*, VOLS 1-5 (2009) 2045-2049.

[24] Rihua Mao, Liyuan Zhang and Ren-yuan Zhu, "Effects of neutron irradiations in various crystal samples of large size for future crystal calorimeter," *2009 IEEE NUCLEAR SCIENCE SYMPOSIUM CONFERENCE RECORD*, VOLS 1-5 (2009) 2041-2044.

[25] F. Nessi-Tedaldi, G. Dissertori, P. Lecomte, D. Luckey and F. Pauss, "Studies of Cerium Fluoride, LYSO and Lead Tungstate Crystals Exposed to High Hadron Fluences," Paper N32-3, 2009 IEEE NSS Conference.

[26] R. Faccini, C. Gargiulo, F. Pellegrino, V. Pettinacci, A. Zullo, "EMC Forward Mechanical Design ", SuperB Technical Note, SB-DET-2012-006

[27] V. Bocci *et al.*, "Dependence of the energy resolution of a scintillating crystal on the readout integration time," arXiv:1207.4902 [physics.ins-det]. Accepted by JINST.

[28] B. Adeva *et al.* [L3 Collaboration], "The Construction of the L3 Experiment," Nucl. Instrum. Meth. A **289**, 35 (1990).

[29] S. K. Sahu *et al.* [Belle Collaboration], "Radiation hardness of undoped BGO crystals," Nucl. Instrum. Meth. A **388**, 144 (1997).

[30] J. Chen, R. Mao, L. Zhang and Y. Ren-Zhu, "Large size LSO and LYSO crystals for future high energy physics experiments," IEEE Trans. Nucl. Sci. **54**, 718 (2007).

[31] B. Aubert *et al.* (*BABAR* Collaboration), *The BABAR Detector*, Nucl. Instrum. Methods Phys. Res., Sect. A **479**, 1 (2002) [arXiv:hep-ex/0105044].

[32] C. Adloff *et al.* [CALICE collaboration] "Construction and Commissioning of the CALICE Analog Hadron Calorimeter Prototype," JINST 5:P05004 (2010).

[33] W. -S. Hou, "Enhanced charged Higgs boson effects in $B^- \to \tau\bar{\nu}$, μ *bar*ν and $b \to \tau\bar{\nu} + X$," Phys. Rev. D **48** (1993) 2342-2344.

[34] W. Altmannshofer, A. J. Buras, D. M. Straub, M. Wick, "New strategies for New Physics search in $B \to K^* \nu\overline{\nu}$, $B \to K \nu\overline{\nu}$ and $B \to X_s \nu\overline{\nu}$ decays," JHEP **0904**, 022 (2009).

[35] T. Barakat, "The "$B \to K^* \nu\bar{\nu}$ rare decay in the two-Higgs doublet model", J.Phys.G G24, 1903 (1998).

[36] B. Aubert *et al.* [BABAR Collaboration], "Search for $B \to K^* \nu\bar{\nu}$," Phys.Rev. D78, 072007 (2008).

[37] P. del Amo Sanchez *et al.* [BABAR Collaboration], "Search for the Rare Decay $B \to K \nu\bar{\nu}$," Phys. Rev. D **82**, 112002 (2010).

[38] V. Andreev *et al.*, "A high granularity scintillator hadronic-calorimeter with SiPM readout for a linear collider detector", Nucl.Instrum.Meth. A540, 368 (2005); T. Takeshita, "Development of MPPC", Pramana 69, 1079 (2007).

[39] M. Bouchel *et al.*, "SPIROC (SiPM Integrated Read-Out Chip): Dedicated very front-end electronics for an ILC prototype hadronic calorimeter with SiPM read-out", JINST 6, C01098 (2011).

[40] H. Ono *et al.*, "Beam test results of a high-granularity tile/fiber electromagnetic calorimeter", Nucl.Instrum.Meth. A600, 398-407 (2009).

[41] R. Faccini, "Results from silicon photomultiplier neutron irradiation test", proceedings of 11th ICATPP Conference on Astroparticle, Particle, Space Physics, Detectors and Medical Physics Applications, Villa Olmo, Como, Italy, 2009.